Friction in Sheet Forming

by

Brian P. Gearing

B.S. Mechanical Engineering
University of Maryland at College Park, 1996

Submitted to the Department of Mechanical Engineering
in partial fulfillment of the requirements for the degree of

MASTER OF SCIENCE

at the

MASSACHUSETTS INSTITUTE OF TECHNOLOGY

May 1999

Author . . . .
Department of Mechanical Engineering
May 18, 1999

Certified by . . . . , ... , ...
Lallit Anand
Professor
Thesis Supervisor

Accepted by . . . .
Ain A. Sonin
Chairman, Department Committee on Graduate Students
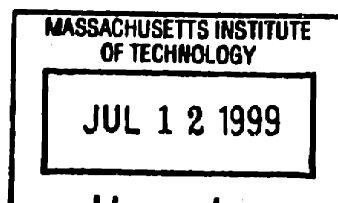
Friction in Sheet Forming

by

Brian P. Gearing

Submitted to the Department of Mechanical Engineering
on May 18, 1999, in partial fulfillment of the
requirements for the degree of
MASTER OF SCIENCE

Abstract

Successful numerical simulations of forming operations require robust and accurate friction models. The present research extends the interface friction model proposed by Anand [1].

The previous work of Anand and Tong [2] and Pisoni [3] considers an application of the model to bulk material processing, whereas the present work is applied to sheet metal forming operations using an aluminum alloy sheet in widespread use in the automotive industry. An interface consisting of lubricated Al6111-T4 sheet and D2 tool steel is investigated. In North America, the Al6111 alloy is currently the material of choice for sheet body panels in a wide variety of automobiles. The lubricants used are MP404 and boric acid. The MP404 lubricant is presently used in industry, and boric acid has recently been proposed as a solid-film lubricant for sheet forming.

The two interfaces are characterized and the model parameters are used in a finite element model to predict the load-displacement curves for axisymmetric cup-drawing and square pan-drawing. The predictions show excellent agreement with the experimental results and represent an improvement over the existing friction models.

The friction model and the proposed testing methodologies are in generic form, and hence may be applied to characterize a wide array of interfaces.

Thesis Supervisor: Lallit Anand
Title: Professor

Acknowledgments

My sincere thanks go to my thesis advisor, Professor Lallit Anand, for supporting the research and providing me with some of the most intellectually challenging years my life has seen. I have learned far more than just Continuum Mechanics and Plasticity.

My thanks go to Ron Rezac, Hyung-Soo Moon, and Chunguang Gu for being dependable and affable research partners and friends.

To the Mechanics and Materials Group at MIT — too many names and too much diversity to ever pay just respect with mere text. Hence, only a statement of my honest gratitude for your support shall have to suffice.

To Prakash Thamburaja and Michael Kim — the only people at this place who could fully understand me and yet, still tolerate me. Without your support, candor, and true friendship... who knows.

My special thanks go to my family for always believing in me.

Contents

List of Figures

6

7

8

9

Chapter 1

Introduction

The goal of the present research is to propose a refined constitutive model for the friction occurring between a tool and workpiece in contact and in relative motion. The model is an extension of the constitutive framework proposed by Anand in [1] and experimentally detailed in Anand and Tong [2] and Pisoni [3]. The constitutive model presented in [1] is a rate-independent, isotropic, and isothermal formulation and shares many similarities with the classical J_2 flow theory of rate-independent isotropic plasticity. For example, as suggested by the experimental results of Courtney-Pratt and Eisner in 1957 [4], the relative velocity at the interface between the tool and workpiece is additively decomposed into an adhering and a slipping part. This decomposition is analogous to the consideration of the total strain rate as being composed of an elastic and a plastic strain rate component. The model is presented in detail in Appendix A.

The traction t at an interface is decomposed, with respect to an orthonormal basis at the interface, into a normal component and a tangential component. The magnitude of the normal component is the normal pressure p and the magnitude of the tangential component is the effective shear stress at the interface $\bar{\tau}$. The slip resistance s at the interface is assumed to be isotropic and has dimensions of stress. The isotropic slip resistance is taken to be a function of the normal pressure p and the accumulated slip at the interface $\bar{u}^s$.

We prescribe a slip condition given by a scalar valued function $\hat{f}(\mathbf{t}, s)$ of the form

$$\hat{f}(\mathbf{t}, s) \equiv \overline{\tau} - \hat{s}(p, \overline{u}^s) \leq 0. \tag{1.1}$$

The slip resistance function $\hat{s}(p, \overline{u}^s)$ is specified by constitutive equations with experimentally determined parameters. The functional form of $\hat{s}(p, \overline{u}^s)$ is motivated by the experimentally determined behavior of the interface under investigation.

The previous results of Anand and Tong [2] and Pisoni [3] consider an interface where the slip resistance s increases with relative sliding distance $\overline{u}^s$, and saturates to a limiting shear stress at the interface as the normal pressure p increases, as is schematically shown in figure D-1. The variation in the slip resistance versus normal pressure at various relative sliding distances is schematically shown in figure D-2; the slip resistance increases with increasing sliding distance and increasing normal pressure. Thus, the previous phenomenological models consider only the case where the interface resistance to sliding, s, hardens with relative sliding distance, $\overline{u}^s$.

However, researchers have found a possible softening at the interface with continued relative sliding for different media, including metal on metal (cf., e.g., [5] and [6]) and granular materials (cf., e.g., [7]). For this type of interfacial response, the slip resistance decreases with increasing sliding distance, as shown in figure D-3 for s versus $\overline{u}^s$ at different values of p, and in figure D-4 for s versus p at different values of $\overline{u}^s$.

The most common friction model is Coulomb friction, which considers the slip resistance to be a function of pressures only

$$s = \mu p, \tag{1.2}$$

where μ is the coefficient of friction. An extension of this model which considers the lower shear yield strength k of two contacting bodies as the limit to the slip resistance is the common shear-cap model specified by

$$s = \begin{cases} \mu p & \mu p < k, \\ k & \mu p \geq k. \end{cases} \qquad (1.3)$$

This model is schematically illustrated in figure D-5. Clearly, these classical friction models are inadequate for modeling the interfacial response schematically shown in figures D-3 and D-4.

In order to address the important case of decreasing slip resistance s with increasing relative sliding distance $\bar{u}^s$, the present research refines the constitutive equations presented in [2] and [3] to give the capability to phenomenologically model either a hardening or softening resistance to interfacial sliding. The evolution equations presented herein are motivated by micromechanical considerations of the complex interactions occurring at an interface.

The present work considers the characterization of the interface between the aluminum alloy sheet metal Al6111-T4, which is in wide use in the automotive industry, and tool steel tooling. The interface is tested with the liquid lubricant Parker Amchem MP404 and the solid-film lubricant boric acid. These lubricants, respectively, exhibit hardening and softening frictional resistances. The model parameters are determined for a hardening interface comprised by Al6111-T4 with an as-rolled or as-received material surface, tool steel, and MP404 lubricant. Friction model parameters for the boric acid lubricated softening interface are also presented. The experimentally determined parameters are then used to predict some technologically important sheet forming operations.

In Chapter 2, the thesis discusses the experimental methods and results for the as-received Al6111-T4 material surface with tool steel, using MP404 and boric acid as lubricants. Specific constitutive functions and the calibration of the model are considered in Chapter 3. Verification of the friction model is presented in Chapter 4, and the thesis is summarized in Chapter 5.

13

Chapter 2

Experiments

The characterization of an interface requires the specification of the slip resistance function $\hat{s}(p, \bar{u}^s)$. In orde to obtain the values for a specific interface, tests similar to those performed by Anand and Tong [2] have been conducted. However, in contrast, the tests in the current work focus on characterizing a tool steel and sheet metal interface under various lubrication and specimen surface conditions. The testing methodology is applied to the aluminum alloy sheet metal Al6111-T4, which is currently in wide use in the automotive industry.

2.1   Experimental Configuration

The experiments are conducted on a Biaxial Instron having a normal load capacity of 50,000 lbf with an axial travel of 4 inches and a torque capacity of 20,000 in-lbf with a rotational travel of 95 degrees. The data acquisition is performed using a LabVIEW 4.1 virtual instrument (vi) specifically designed for the friction test. Using the vi, the user simply inputs the filename for storage and any desired headings to be written to the data file. The user inputs tool diameters into the vi that can be changed to accommodate any tool for testing, and a vi graph allows for the real time display of the shear stress versus sliding distance.

Another feature of the vi is that it is designed to smooth voltage inputs by sampling up to 1 kHz and averaging each input in real time, hence giving an artificial rate of

1 Hz based on many more data points. The advantage of this processing is that it allows for filtered data in real time with smaller files for storage of data. Of course, at high sliding rates, only raw voltage data is acquired and written to the file so as not to average out the dynamics of the process.

The nominal gage of the Al6111 sheet is 0.96 mm. Sheet metal samples, 31.75 mm x 31.75 mm squares, are tested using the configuration schematically shown in figure D-6. The detailed drawings for the tools are shown in figures D-7, D-8, and D-9. The tool and indenter are made of D2 tool steel with a hardness of 52 HRC, from which it is estimated that the yield strength of the tool is on the order of 1250 MPa. The contact region of the tool is an annulus with an outer diameter of 27.64 mm and an inner diameter of 23.97 mm, giving a small contact width of about 1.84 mm in order to approximate a constant shear stress. The contacting surface of the indenter is finely knurled and this effectively holds the specimen in place over a wide range of pressures.

In order to account for the inevitable angular misalignment existing in any system of shafts, the mean tool diameter is designed to minimize the effects of the offset while still allowing for a considerable circumferential sliding distance when subjected to a monotonic angular displacement of the tool. The maximum sliding distance permitted by the tool and Instron is about 22 mm. After measuring the maximum angular velocity output of the Instron and considering the mean tool diameter, the maximum linear velocity at the interface under no load is approximately 20 mm/s.

2.2   Experimental Procedure

Before performing each test, the specimen is cleaned with laboratory grade acetone and the tool is polished to a mirror finish using 1 micron alumina in a distilled water slurry. The tool is polished before every test in order to give a constant initial interface. The sheet metal sample is placed between the tool and indenter pieces where it is held fixed by the indenter as the tool rotates. The test is conducted under a fixed normal load in order to maintain a constant normal pressure as sliding progresses.

Denoting the tool outer diameter by D_o and the inner diameter by D_i, the shear stress, τ, at the interface is found from

$$\tau = \frac{2T}{A_n \overline{D}} \tag{2.1}$$

where T is the measured torque at the interface, $A_n = \pi(D_o^2 - D_i^2)/4$ is the nominal contact area of the tool, and $\overline{D} = (D_o + D_i)/2$ is the mean tool diameter. The shear stress is taken to be equal to the isotropic slip resistance, s, for the rate-independent model.

The normal pressure, p, during the test is

$$p = \frac{N}{A_n} \tag{2.2}$$

where N is the measured normal load.

The sliding distance or relative slip, $\overline{u}^s$, is given by

$$\overline{u}^s = \frac{\overline{D}\theta}{2} \tag{2.3}$$

where θ is the measured angle of rotation in radians.

The coefficient of friction, $\mu \equiv \tau/p$ is then calculated from

$$\mu = \frac{2T}{\overline{D}N}. \tag{2.4}$$

Note that the nominal tool area is used to calculate the shear stress and the normal pressure and does not appear explicitly in equation 2.4.

As the test is conducted, the shear stress, sliding distance, and normal pressure are calculated by the vi, displayed in real time, and written to the data file. The data is then post-processed to obtained curves of τ versus $\overline{u}^s$ at fixed p, μ versus $\overline{u}^s$ at fixed p, and τ versus p at fixed $\overline{u}^s$. The data is then used to calibrate the numerical model.

2.3 Application to Aluminum Sheet Metal

A current trend in the automotive industry is the replacement of steel sheet metals by lighter weight aluminum alloys. The aluminum alloys not only provide for less energy consumption during sheet forming, but also allow for lighter and more fuel-efficient vehicles. Unfortunately, as is well known, the high affinity of the aluminum for tool steel dies and punches may limit the service life of the tooling and results in poor surface finish on the finished product. Hence, methods of inhibiting workpiece wear and enhancing its formability are highly desirable. It is to this end that the present work investigates the effects of various lubricants on the as-received material surface

2.3.1 Bulk Material Behavior

The aluminum alloy chosen as the candidate material is Al6111-T4, which is a Mg-Si aluminum alloy with a nominal composition of (in weight percent) 1 Mg, 1.1 Si, 0.9 Cu, 0.4 Fe, 0.45 Mn, and 0.1 Ti [10]. In North America, the Al6111 alloy is currently the material of choice for the deck lids of the Ford Crown Victoria, Mercury Grand Marquis, and Taurus/Sable models. The sheet metal is typically supplied in a soft condition—T4 in the present case—with a yield strength of around 150 MPa, which allows for good formability [10]. Due to strain hardening effects during a forming operation, an alloy in the T4 state may obtain a yield strength on the order of 350 MPa to 400 MPa. The yield strength correlates to the material hardness or 'dent' resistance of the automotive component.

The material behavior is modeled via isotropic rate-dependent plasticity, details of which may be found in [8]. Since the present work deals with a sheet metal, the approximation of isotropy to model the bulk material behavior must be justified. This task is accomplished by testing three sheet tension specimens—one parallel to the rolling direction (RD), one at forty-five degrees to the RD, and one at ninety degrees to the RD. The ASTM E8 standard dimensions for the sheet tension specimens are detailed in figure D-10. The tension tests are conducted at a constant true strain rate of 0.0004/s, and an additional test is performed with a strain rate increment

18

of two decades in order to determine the rate sensitivity of the material at room temperature.

The Young's modulus of the material is found by performing multiple unloadings and reloadings of a specimen. The average Young's modulus is calculated as 63.2 GPa and a Poisson's ratio of 0.33 is assumed. A comparison of the load versus displacement results for all three directions is given in figure D-11. Although there is a variation in ductility with specimen orientation, the difference in the hardening characteristics is not significant, hence, the assumption of planar isotropy is valid. Note that normal or through-thickness isotropy is assumed.

The RD is chosen to find the hardening parameters of the material. Using a curve-fitting procedure written in Matlab (see Routine 1 in Appendix C), the parameters necessary for the model detailed in [8] are calculated as

$$s_o = 176 \text{ MPa}, \quad s_s = 737 \text{ MPa}, \quad h_o = 6270 \text{ MPa}, \quad a = 3.58, \quad m = 0.002.$$

The calibration results are shown in figure D-12. The material behavior is accurately modeled with the given parameters. Note that here s_o and s_s correspond to initial and saturation values of the deformation resistance of the workpiece material.

With the bulk material model calibrated, the next steps are to experimentally characterize specific interfaces and to calibrate the numerical model for the tangential traction evolution. The two models are then coupled in order to capture the bulk material behavior when subjected to various boundary conditions. The following chapters are concerned with the experimental and numerical characterizations of two different interfaces.

2.4   Experimental Results

The present experimentation characterizes the lubricated aluminum sheet metal and tool steel interface under typical engineering conditions with respect to the surface topography of the sheet. It is with this as-received surface structure that the material would typically be formed in industry. The approach is similar to the work of such previous researchers as Anand and Tong [2] where friction in the processing of bulk materials is investigated.

The experimental methodology detailed in the previous sections is first applied to the Al6111-T4 sheet metal with an as-rolled or as-received surface topography. A profile of the as-received surface is shown in figure D-13, where the peak to peak amplitude of the surface is 2 microns. All tests in this section are conducted at a sliding velocity of 1 mm/s under pressures ranging from 5 MPa to 600 MPa. The effects of two types of lubricant — liquid and solid-film — in conjunction with the as-received material surface against tool steel are investigated.

2.4.1   MP404 Lubricant

This section presents the experimental results for the liquid lubricated Al6111-T4 and tool steel interface. The lubricant is Parker Amchem MP404, a commercial lubricant in widespread use in the automotive industry. After cleaning the specimen with Acetone, the MP404 is applied to the specimen using a camel hair brush. A generous amount of lubricant is evenly distributed over the specimen surface until the depth is about 0.3 mm. Tests are conducted under conditions of monotonic sliding for a sliding distance of 20 mm and under cyclic sliding for a cumulative sliding distance of 1 m.

Results for Monotonic Sliding

The shear stress versus sliding distance for the MP404 lubricated Al6111-T4 and tool steel interface is shown for low pressures, 5 MPa to 40 MPa, in figure D-14 and for high pressures, 100 MPa to 600 MPa, in figure D-15. As can be seen from figure D-14, the hardening is negligible over the first 20 mm of sliding for pressures from 5 MPa

to around 20 MPa. This is most likely due to less contact at the asperities of the interface, thus allowing for the effects of boundary lubrication with the liquid film supporting a considerable portion of the load. Indeed, an inspection of the wear tracks on the specimens for normal pressures in the range of 5 MPa to 20 MPa reveals little discernible damage when compared to the higher pressure tests. At pressures on the order of 40 MPa and above, the shear stress markedly increases with sliding distance. Note that at the highest test pressure of 600 MPa, the shear stress increases from an initial value of 49 MPa to a value after 20 mm of sliding of around 92 MPa, which is almost twice the initial value. Tests at selected pressure levels are conducted twice to consider data repeatability. The data is repeatable to within an average band of 6 % variation for the range of the current tests.

The results of the experiments in the shear stress - normal pressure plane at various fixed sliding distances is shown in figure D-16. The figure is in accord with the experimental results of Anand and Tong [2]. However, unlike the results of [2], the current data shows the effects of boundary lubrication at pressures of 5 MPa to 20 MPa with coefficients of friction on the order of 0.15 after a sliding distance of 20 mm. An inflection point in the shear stress versus normal pressure curve occurs at $p = 25$ MPa, and the friction coefficient increases to a maximum of about 0.28 at $p = 100$ MPa and 20 mm of sliding. A second inflection point occurs around a normal pressure of 100 MPa – 120 MPa, and the shear stress is seen to saturate at around a normal pressure of 600 MPa. Recall that the 0.2 % offset yield strength for the bulk material is $s_o = 176$ MPa, which gives a shear yield strength of $k_o = 102$ MPa. Figure D-16 indicates that at $p = 600$ MPa, saturation values of the shear stress approach 90 MPa, which is consistent with the notion of the shear yield strength of the material substrate as the limit of the interfacial slip resistance.

As can be seen from the results of this section, the shear stress increases with increasing sliding distance, hence constitutive models for the slip resistance similar to those incorporated in [2] and [3] are applicable. The hardening behavior is valid for the present sliding range. An investigation of the response of the interface under cyclic sliding conditions is presented in Appendix B, where the accumulated sliding

distances reach values up to 2 m.

These experimental results are used in the next chapter to motivate functional forms for the evolution of the slip resistance.

2.4.2 Boric Acid

The experimental study of the as-received Al6111-T4 and tool steel interface is extended by considering the effects of a dry, solid-film lubricant composed of boric acid particles. Widely used as an insecticide and as a dessicating agent, boric acid has only recently been investigated for use as a solid-film lubricant. The work of Erdemir and colleagues at Argonne National Laboratory presented in [11], [12], and [13] introduces preliminary results for tribological tests performed with boric acid powder as a lubricant between steel and aluminum. Coefficients of friction as low as 0.02 have been reported for pin-on-disk tests using boric acid powder between a steel pin and Al6061 disk [13]. The claims of these researchers are the impetus of the current testing.

The most common form of boric acid is called orthoboric acid and exists as a natural deposit known in the mineralogy literature as sassolite [13]. The layered crystal structure of boric acid is schematically shown in figure D-17. The high lubrication capacity of boric acid arises from its layered crystal structure which contains planes of covalently bonded triangular groups of BO_3 with some ionic bonding character [11]. The planes are held together by weak van der Waals forces [11]. It is hypothesized that as the boric acid is loaded and relative sliding is imposed, the layers align in the direction of sliding, and, due to the weak van der Waals forces, the layers are able to slide over each other with relative ease [11]. The result is extremely low friction that decreases with increasing normal pressure [13]. A more detailed discussion of the structure of boric acid and its mechanisms of formation can be found in Erdemir [11] and in Erdemir et al. [12].

The lubricant is prepared for application by mixing granular particles of boric acid with water in the ratio of about 1 g of H_3BO_3 to 4 mL of H_2O and then slowly heating the mixture in a hood. With gentle stirring, the mixture turns to a clear

solution at around 70°C to 80°C. After cleaning the sheet metal specimen with Acetone, the heated mixture is evenly applied to the specimen surface using a camel hair brush. The specimen is then allowed to dry at room temperature for at least four hours. This procedure produces a relatively even and durable boric acid coating on the material surface.

Results for Monotonic Sliding

The shear stress versus sliding distance for the boric acid lubricated Al6111-T4 and tool steel interface at $\bar{v}^s = 1$ mm/s and at normal pressures ranging from 20 MPa to 100 MPa and from 200 MPa to 600 MPa is shown in figures D-18 and D-19, respectively. The initial softening behavior of the shear stress response at every normal pressure should be noted. This softening is most likely due to the stress required to align the initially randomly oriented layers of the boric acid [11]. At all pressures, the shear stress attains a relatively constant value after 4 mm of sliding. An inspection of the specimens reveals no discernible wear at pressures from 20 MPa to 40 MPa, which is in contrast to the tests conducted with MP404. The variation of the coefficient of friction with sliding distance over a range of normal pressures is shown in figure D-20. The graph shows a decrease in the coefficient of friction with increasing normal pressure. The experimental results are in accord with those presented in [12] and [13].

The variation of the shear stress with normal pressure at various sliding distances is shown in figure D-21. When compared with figure D-16, it is clear that all coefficients of friction over the range of pressures tested are considerably lower than those obtained by using MP404 as the lubricant. As can be seen from figure D-22, the coefficient of friction for the MP404 case at 100 MPa normal pressure and after 20 mm of sliding is about 0.29 and that of the boric acid case is 0.063, or a reduction of 78 %! This impressive result demonstrates the potential of boric acid as an energy saving commercial lubricant.

The following chapter shall address the characterization of both the MP404 and boric acid lubricated Al6111-T4 sheet against tool steel.

Chapter 3

Model Calibration

This chapter considers the experimental results presented for the MP404 and boric acid lubricated Al6111-T4 and tool steel interfaces under monotonic sliding. A constitutive function for the slip resistance is motivated by the experimental data, and the two interfaces are characterized by fitting the proposed evolution equations to the experiments. The model parameters are used in the following chapter to verify the friction model by numerically predicting the behavior of complicated sheet-forming experiments.

3.1   Specific Constitutive Functions

A consideration of the variation of the slip resistance with both sliding distance and normal pressure as indicated by the experimental results in the previous chapter reveals several general trends.

As can be seen from figure D-14, for the MP404 case, the shear stress shows little evolution with increasing sliding distance for pressures up to about 20 MPa. In this region, the effects of boundary lubrication appear to prevail. As the real area of contact increases with increasing pressure, the lubricant effects become less dominant, and hence the slip resistance shows a marked increase with increases in sliding distance. At high pressures, on the order of 600 MPa, the slip resistance is seen to approximately approach the shear yield strength of the sheet material. Thus,

24

the constitutive relation must capture negligible hardening at low pressures and then allow for evolution of s with $\overline{u}^s$ until it saturates around the material shear yield strength.

The results when using boric acid show that s increases with p at a fixed $\overline{u}^s$, figure D-21. However, in contrast with the case of MP404, when using boric acid, s decreases with increasing sliding distance $\overline{u}^s$. Hence, the model must also allow for the possibility of an interface that shows a softening behavior of s with accumulated slip $\overline{u}^s$.

A simple form for the slip resistance function $\hat{s}(p, \overline{u}^s)$ which is similar to that suggested by Anand [1], but which accounts for the possibility of negligible surface hardening at low pressures (e.g., during lubricated sliding between certain metallic surfaces) is the function

$$\hat{s}(p, \overline{u}^s) = \begin{cases} \mu_l p & p \le p_{cr}, \\ s^* \tanh \left\{ \dfrac{\mu(p - p_{cr})}{s^*} \right\} + \mu_l p_{cr} & p > p_{cr}, \end{cases} \tag{3.1}$$

with

$$\mu = \hat{\mu}(\overline{u}^s) \quad \text{and} \quad s^* = \hat{s}^*(\overline{u}^s). \tag{3.2}$$

Here, μ_l is the coefficient of friction at pressures p which are less than a critical pressure, p_{cr}. At very low normal pressures, equation (3.1) gives

$$s = \mu_l p, \tag{3.3}$$

thus, μ_l represents the conventional coefficient of Coulomb friction at low pressures. For p slightly larger than p_{cr}, equation (3.1) gives

$$s = (\mu_l - \mu)p_{cr} + \mu p. \tag{3.4}$$

Therefore, μ is the Coulomb friction operative once the lubricant effects become less dominant and the real area of contact begins to increase. At high pressures, equation (3.1) goes to

$$s \approx s^*, \tag{3.5}$$

hence s^* represents the limit of interfacial slip at high contact pressures for a given relative slip.

The remaining step in the model formulation is to specify phenomenological equations for the functional dependence of μ and s^* on $\overline{u}^s$. The evolution laws for μ and s^* may be expressed in incremental form as

$$\dot{\mu} = h_1 \cdot \overline{v}^s, \quad \mu(0) \equiv \mu_o \tag{3.6}$$

and

$$\dot{s}^* = h_2 \cdot \overline{v}^s, \quad s^*(0) \equiv s_o^*, \tag{3.7}$$

where

$$h_1 \quad \text{and} \quad h_2 \tag{3.8}$$

are experimentally determined hardening functions and μ_o and s_o^* are initial values of μ and the saturation value of the slip resistance s^*, respectively. Note that μ_o is the initial value of the friction coefficient at a pressure level that is greater than p_{cr}, thus μ_o should not be confused with μ_l.

The previous work of Anand and Tong [2] and Pisoni [3] considered a case where both μ and s^* increased with $\overline{u}^s$ until saturation values were reached. The fit equations were motivated by experimental observations of the shear stress response with accumulated slip up to about 45 mm for dry interfaces of copper against steel [3]. As

26

a modification to the model proposed by Anand [1], Hughes et al. [6] suggested a functional form for $\mu(\overline{u}^s)$ that could account for their experimental observation of a softening of the interfacial shear stress with accumulated slip for an interface similar to that in [2]. Also, the data presented in the previous chapter clearly indicates the possibility of s increasing or decreasing with $\overline{u}^s$ at a given p.

The phenomenon of shear stress softening with accumulated slip at an interface has been observed in many tribosystems for quite some time. For example, Bridgman in 1936 noted the jerky motion and marked sudden stress drops that accompany the shearing of rocks at high normal pressures, and suggested that such behavior might be a possible mechanism for earthquake generation [14]. Indeed, a review of the current literature on constitutive modeling of friction reveals a large amount of active research in the geophysical community dealing with the concerns expressed by Bridgman. Shear stress softening is also considered in the simplified friction models incorporated in mechanics, where the static friction is taken to be larger than the kinetic friction.

Therefore, with regard to the experimental results indicating a pressure sensitive softening of the interfacial shear stress with accumulated slip, following the work of Anand and Gu [7] on granular materials, we present functional forms for $\mu(\overline{u}^s)$ and $s^*(\overline{u}^s)$ that are motivated by micromechanical considerations of the complex interactions at the interface of two contacting bodies

Evolution Equation for μ

Motivated by the work of Anand and Gu [7] on granular media, where dilatational effects play a dominant role in the material response, we introduce a parameter η as an internal variable to account for the redistribution of asperity contacts coupled with wear debris and particle agglomeration at contact interfaces.

We express the evolution of μ in incremental form as

$$\dot{\mu} = h_1 \cdot \overline{v}^s, \quad \mu(0) \equiv \mu_o, \tag{3.9}$$

and we take the hardening function h_1 to be governed by

$$h_1 = h_\mu \cdot \left|1 - \frac{\mu}{\mu_s}\right|^{r_1} \cdot \text{sign}\left(1 - \frac{\mu}{\mu_s}\right),$$ (3.10)

where

$$\mu_s = \begin{cases} \mu_k + b \cdot [\eta - \eta_{cr}]^q & \eta \geq \eta_{cr}, \\ \mu_k & \eta < \eta_{cr}, \end{cases}$$ (3.11)

and add the evolution equation

$$\dot{\eta} = -\eta \cdot h_\beta \cdot [\mu - \mu_k] \cdot \bar{v}^s, \quad \eta(0) \equiv \eta_o.$$ (3.12)

The material parameters in the above evolution equations are

$$\{\mu_o, \mu_k, \eta_o, \eta_{cr}, h_\mu, h_\beta, r_1, q, b\}.$$ (3.13)

The hardening modulus h_1 is positive when $\mu < \mu_s$, it is negative when $\mu > \mu_s$, and the quantity μ_s depends on the value of the internal variable η with respect to a critical value η_{cr}. If initially $\eta_o < \eta_{cr}$ and $\mu_o < \mu_k$, then the friction coefficient μ increases until it reaches a value μ_k. The value μ_k may be interpreted as the kinetic coefficient of friction. The internal variable η is specified such that its evolution $\dot{\eta}$ approaches zero as μ approaches μ_k. When $\eta_o > \eta_{cr}$, the coupled nature of the evolution equations will give a peak in the friction coefficient μ versus sliding distance $\bar{u}^s$ in monotonic sliding. The equations 3.9, 3.10, 3.11, and 3.12 provide a useful phenomenological method for modeling a wide variety of interfaces.

If the interface under investigation shows no softening, we may recover the functional form for μ proposed in [2] and [3], by taking μ_s as a constant, $r_1 = 1$, and

28

expressing the hardening function as

$$h_1 = \frac{\mu_s}{u_1} \cdot \left(1 - \frac{\mu}{\mu_s}\right),$$ (3.14)

which may be integrated to give

$$\mu = \mu_o + [\mu_s - \mu_o] \cdot \left[1 - \exp\left(\frac{-\bar{u}^s}{u_1}\right)\right],$$ (3.15)

where u_1 is a fit parameter with dimensions of length. Equation 3.15 is precisely the function used in [2] and [3] to model a non-softening interface.

Evolution Equation for s^*

The functional form adopted for the evolution of the interfacial shear stress at high contact pressure is

$$\dot{s}^* = h_2 \cdot \bar{v}^s, \quad s^*(0) \equiv s_o^*$$ (3.16)

where we take

$$h_2 = h_s \cdot \left|1 - \frac{s^*}{s_s^*}\right|^{r_2} \cdot \text{sign}\left(1 - \frac{s^*}{s_s^*}\right).$$ (3.17)

Here, h_s is a modulus with dimensions of stress per length and is a fit parameter, the power r_2 is a fit parameter, and s_s^* is a saturation value for the high pressure shear stress. We may again recover the functional forms in [2] and [3] by taking $r_2 = 1$ and specifying

$$h_2 = \frac{s_s^*}{u_2} \cdot \left(1 - \frac{s^*}{s_s^*}\right),$$ (3.18)

29

with u_2 as a fit parameter having dimensions of length. We then integrate equation 3.18 to obtain

$$s^* = s_o^* + (s_s^* - s_o^*) \cdot \left[1 - \exp\left(\frac{-\overline{u}^s}{u_2}\right) \right],$$
(3.19)

which is the function s^* used in [2] and [3] to model a non-softening interface.

3.2 Calibration

3.2.1 MP404 Lubricant

The first interface to be calibrated is that of MP404 lubricated Al6111-T4 against tool steel. The interfacial behavior is taken to be one of a hardening slip resistance with sliding distance.

In order to model the interface as hardening, we ensure that η remains less than or equal to η_{cr} at all times during the process (see equation 3.11), hence $\mu_s = \mu_k$. Using this assumption, we may integrate equation 3.9 to obtain

$$\mu(\overline{u}^s) = \mu_k \left[1 - \left\{ \frac{(r_1 - 1) \cdot h_\mu \cdot \overline{u}^s}{\mu_k} + \left(1 - \frac{\mu_o}{\mu_k} \right)^{1-r_1} \right\}^{\frac{1}{1-r_1}} \right], \qquad (3.20)$$

The evolution of the saturation value of the slip resistance is taken to be governed by

$$s^*(\overline{u}^s) = s_o^* + (s_s^* - s_o^*) \cdot \left[1 - \exp\left(\frac{-\overline{u}^s}{u_2} \right) \right]. \qquad (3.21)$$

In order to obtain the model parameters for equations 3.1, 3.20, and 3.21, the following four steps are performed:

Step 1

With reference to figures D-14, D-15, and D-16, one may discern essentially no evolution of s with sliding distance until normal pressures greater than 20 MPa and less than 30 MPa are reached. Thus, the critical pressure p_{cr} is estimated to be 25 MPa. In order to obtain μ_l for this range, a representative test is selected and the average friction coefficient is calculated. In this case, the test conducted at a normal pressure of 15 MPa is used for calibration. The result of the fit is shown in figure D-23, where the average friction coefficient is specified as $\mu_l = 0.15$.

31

Step 2

In order to find the model parameters for equation 3.20, the test conducted at a normal pressure of 100 MPa is chosen to represent the hardening behavior of s in an intermediate range between a case of no evolution in s with sliding distance, and a case where the saturation values of s are reached. The experimentally obtained shear stress is divided by the normal pressure and the integrated equation 3.20 is fit to the data by trial and error with a Matlab routine, which is detailed in Appendix C as Routine 2. The result of the fit is shown in figure D-24.

Step 3

The parameters for the evolution of the saturation value of the slip resistance with sliding distance are found by fitting equation 3.21 to the test conducted at the highest normal pressure of 600 MPa. The fit is performed by trial and error with the Matlab Routine 3 in Appendix C. The fit is shown in figure D-25.

Step 4

The values obtained from the previous three steps are now used with equations 3.1, 3.20, and 3.21 to refine the friction model fit (using the Matlab Routine 4 of Appendix C) of the evolution of the slip resistance with sliding distance at any pressure, as indicated in figures D-26 and D-27, where the model is used to capture the experimental behavior for low and high normal pressures, respectively. As can be seen from these results, the friction model fit is excellent.

The parameters used to model the interface consisting of Al6111-T4 with MP404 lubricant against tool steel are:

$$\mu_l = 0.15 \qquad p_{cr} = 25 \text{ MPa}$$

$$\mu_o = 0.11 \qquad \mu_k = 0.32 \qquad h_\mu = 1 \text{ mm}^{-1} \quad r_1 = 4 \qquad (3.22)$$

$$s_o^* = 60 \text{ MPa} \quad s_s^* = 200 \text{ MPa} \quad u_2 = 120 \text{ mm}.$$

Note that for this specific interface, η_o, η_{cr}, h_β, q, and b are not considered since $\eta(\overline{u}^s) \leq \eta_{cr}$ is enforced.

3.2.2 Boric Acid

The softening behavior experimentally observed for an interface comprised by boric acid, Al6111-T4, and tool steel is modeled by fitting equations 3.1, 3.9 and 3.21 to the experimental data at appropriate normal pressures. The fitting procedure is performed in four steps:

Step 1

With reference to figures D-18 and D-19, one may discern that the slip resistance evolves with sliding distance even for the lowest experimental normal pressure of 20 MPa. Hence, for this interface, the critical pressure p_{cr} is taken to be zero and μ_l is no longer germane.

Step 2

The test conducted at a normal pressure of 100 MPa is chosen to represent the slip resistance evolution at low normal pressures, and equation 3.9 is fit by trial and error to the data by using a Matlab code with explicit time integration (see Routine 5 in Appendix C). The result of the fit is shown in figure D-28.

It should be noted that in adjusting the parameters for the above fit, the response of the fit equation is sensitive to the values of η_o and η_{cr} for picking up the initial evolution of μ with $\overline{u}^s$. Also, the parameters r_1 and h_μ have a strong effect on the shape of the response curve. The fit response is less sensitive to the parameters h_β, b, and q.

Step 3

The evolution of the saturation value of the slip resistance is taken to be indicated by the test conducted at a normal pressure of 600 MPa. Equation 3.21 is fit to the data by trial and error using Routine 3 in Appendix C. The result is shown in figure D-29.

33

Step 4

The values just obtained are now used with equations 3.1, 3.9, and 3.21 to further fit (see Routine 6 in Appendix C) the evolution of the slip resistance with sliding distance at any pressure, as indicated in figures D-30 and D-31, where the model is adjusted to capture the experimental behavior for low and high normal pressures, respectively. As can be seen from these results, the friction model fit is excellent for the entire range of pressures tested.

The parameters used to model the interface consisting of Al6111-T4 with boric acid against tool steel are:

$$
\begin{aligned}
&p_{cr} = 0 \text{ MPa} \\
&\mu_o = 0.088 \qquad \mu_k = 0.061 \qquad h_\mu = 0.3 \text{ mm}^{-1} \quad r_1 = 2.5 \\
&\eta_o = 0.12 \qquad\;\; \eta_{cr} = 0.10 \qquad h_\beta = 2.5 \text{ mm}^{-1} \quad b = 2 \qquad q = 3 \\
&s_o^* = 55.6 \text{ MPa} \quad s_s^* = 36.1 \text{ MPa} \quad u_2 = 1.6 \text{ mm}.
\end{aligned}
\tag{3.23}
$$

The specified parameters for both interfaces are used in a numerical model in the following chapter for purposes of model verification.

Chapter 4

Model Verification

This chapter is concerned with the verification of the friction model. The parameters for both the MP404 and boric acid lubricated interfaces determined in the previous chapter are used in numerical calculations using ABAQUS/Explicit v5.8 to predict the behavior of axisymmetric cup-drawing and square pan-drawing of blanks of Al6111-T4 lubricated by MP404 and boric acid.

4.1 MP404 Lubricant

4.1.1 Axisymmetric Cup-Drawing

Experiment

The axisymmetric cup-drawing experiment is performed using a double-action servo-controlled forming press developed by Lee [15]. The geometry of the apparatus is shown schematically in figure D-32, where we note that in our experiments the applied blankholder force is a constant 10 kN throughout the drawing process. All surfaces in contact with the deforming blank are polished to a mirror finish. The die set, which is composed of the punch, die, and binder, is constructed of AISI/SAE D2 steel, hardened to a minimum of 62 HRC. The circular blank of the as-received Al6111-T4 is cut on a water-jet machine and has a radius of 50.8 mm with a thickness of 0.95 mm.

The test is conducted by first cleaning the blank with acetone and then spreading a generous layer of MP404 on both sides of the blank. The blank is carefully centered on the binder and an IBM-486 PC equipped with a real-time data acquisition board (DT2801-A) actuates the press to apply the binder force of 10 kN, move the punch at about 1 mm/s, and simultaneously the computer records the load-displacement data as the blank is formed. The test is completed when either the blank is drawn completely through the die or the specimen fails. The draw ratio, or blank diameter divided by the punch diameter, is about 2.

The blank of Al6111-T4 with MP404 lubricant completely draws through the die without failure. The drawn cup is shown in figure D-33.

Simulation

The simulation is carried out using an algorithm written by H. S. Moon for the friction model in the VFRIC subroutine in ABAQUS/Explicit v5.8 coupled with a User-Material Subroutine for the bulk material behavior written by L. Anand. The bulk material parameters given in Chapter 3 are used in the latter subroutine. The experiment is modeled using axisymmetric CAX4R elements and rigid surfaces for the punch, die, and binder [17]. The axisymmetric mesh is shown in figure D-34, and the deformed mesh is shown in figure D-35. Note the large amount of thinning in the cup wall as evidenced in figure D-35, which elucidates why most drawing failures are initiated at the nose of the punch.

The friction model prediction of the punch load versus punch displacement for the cup-drawing experiment is compared against the experimental data in figure D-36. The peak load for the operation and the general load-displacement behavior and load levels are well predicted by the simulation.

As a final exercise, we compare the simulation prediction for the cup-drawing experiment with numerical predictions using the standard shear cap friction model in ABAQUS [17]. Two shear cap models are chosen, with the first at 0 mm of sliding and the second at 20 mm of sliding. The shear cap model parameters are obtained from the experimental data and are shown in figure D-37. The simulation predictions

using the shear cap parameters are shown against the experiment and our friction model prediction in figure D-38. Clearly, considering that no a priori knowledge of the shear cap parameters could be obtained without experimentation, our friction model provides a superior method for accurate prediction.

4.1.2 Square Pan-Drawing

Experiment

A square pan-drawing experiment is performed in order to further test the predictive capabilities of our numerical model. The experiment is conducted using the same double-action servo-controlled forming press used for the axisymmetric cup-drawing experiment. The geometry of the apparatus is shown schematically in figure D-39. All surfaces in contact with the deforming blank are polished to a mirror finish. The die set, which is composed of the punch, die, and binder, is constructed of AISI/SAE D2 steel, hardened to a minimum of 62 HRC. The square blank of the as-received Al6111-T4 is cut using sheet metal shears and is 228.6 mm x 228.6 mm with a thickness of 0.95 mm.

The test is conducted by first cleaning the blank with acetone and then spreading a generous layer of MP404 on both sides of the blank. The blank is carefully centered on the binder and as before, the system applies a binder force of 15 kN, moves the punch at about 1 mm/s, and simultaneously records the load-displacement data as the blank is formed. The test is completed when either the blank is drawn completely through the die or the specimen fails. Note that the large clearance between the punch and the die may allow for a significant amount of buckling of the blank side walls as it is drawn into the die.

The square blank of Al6111-T4 is drawn into the die cavity and fails at the punch tip after about 46 mm of punch displacement. The drawn specimen is shown in figure D-40 where side wall and flange buckling as well as failure at the inside corners of the pan may be observed.

37

Simulation

The simulation is carried out using the standard friction specification in ABAQUS/Explicit v5.8 [17] with a value of $\mu_l = 0.15$ since the normal pressures do not exceed $p_{cr} = 25$ MPa. The User-Material Subroutine for the bulk material behavior written by L. Anand is used. The experiment is modeled using quarter symmetry with C3D8R elements for the blank and R3D4 elements for the punch, die, and binder [17]. There is one element through the thickness for the blank.

The undeformed mesh is shown from a top view in figure D-41, and the deformed mesh is shown in figure D-42. Note the side wall buckling as evidenced in figure D-42, which is similar to the behavior that is observed in the experiment.

The friction model prediction of the punch load versus punch displacement for the pan-drawing experiment is compared against the experimental data in figure D-43. The simulation has been stopped at about the same location where failure occurred in the drawn specimen as indicated by the abrupt end to the experimental data at around 35 kN. The peak load for the operation and the general load-displacement behavior and load levels are well predicted by the friction model.

4.2 Boric Acid

4.2.1 Axisymmetric Cup-Drawing

Experiment

The axisymmetric cup-drawing experiment is performed using the same experimental equipment and procedure as for the MP404 case. However, the blank is now coated on both sides with boric acid.

The blank of Al6111-T4 with boric acid as lubricant fails abruptly at the punch tip after only about 18 mm of punch displacement. The failed cup is shown in figure D-44, where it is noted that the photograph is taken after the specimen is cleaned in a solvent. A postmortem examination of the specimen reveals severe galling of the surface at the contact region between the blank and the die radius. Essentially, the boric acid layer is completely sheared from the surface and provides no effective lubrication. Hence, experimental studies into procedures to provide more tenacious bonding between the boric acid and aluminum surface are warranted.

Simulation

A simulation is carried out using the model parameters from Chapter 4 for the boric acid case, and the same axisymmetric mesh as that of the MP404 lubricant case is used. The simulation is performed in order to approximately ascertain the response of the boric acid lubricated specimen without failure.

The friction model prediction of the punch load versus punch displacement for the cup-drawing experiment is compared against the experimental data in figure D-45. As can be seen from the figure, if the boric acid layer adheres effectively, the peak load level is considerably reduced when compared to the levels obtained with MP404 lubricant (assuming of course that the simulation accurately predicts the response). This point is more clearly observed with reference to figure D-46, which compares the numerical simulations of the punch load versus punch displacement of the MP404 and boric acid lubrication cases. A comparison of the peak loads gives a reduction of about 13% when using boric acid as opposed to MP404 as lubricant.

The results presented herein indicate the possibility of using boric acid to gain significant savings in energy consumption when used on a mass production scale. However, the integrity of the boric acid layer must be improved before commercial implementation is possible. These results provide an impetus for further pursuit of integrating this promising lubricant into widespread industrial use.

The present results demonstrate that with a few simple monotonic sliding experiments to obtain the dependence of the shear stress on the normal pressure at fixed sliding distances, one may calibrate the robust friction model to a wide range of interfaces and accurately predict complicated multi-axial experiments.

Chapter 5

Closure

The constitutive model for interface friction introduced by Anand in [1] is reviewed. The model is fully three-dimensional, rate-independent, isothermal, and isotropic in nature. The model is developed in a context that is analogous to the classical J_2 flow theory of rate-independent isotropic plasticity. The notion of an interfacial slip resistance that serves as a macroscopic response characteristic to account for the complicated micromechanical interactions at the surface is put forth. New evolution equations for the interfacial slip resistance similar to those incorporated in [7] are proposed. These equations are able to capture a wide range of interface behavior, from hardening to softening of the slip resistance with accumulated sliding distance under variable normal pressure.

The previous work of Anand and Tong [2] and Pisoni [3] applied the constitutive model with similar slip resistance evolution equations to the deformation processing of bulk materials. The present work extends the application realm to sheet forming operations and proposes a novel methodology to obtain the experimental data necessary to calibrate the friction model. The interfaces investigated herein are Al6111-T4 with MP404 against tool steel and Al6111-T4 with boric acid against tool steel. The interfaces are completely characterized within the context of the model, and the fit parameters are incorporated into a numerical model, which has been implemented into the VFRIC subroutine in ABAQUS/Explicit v5.8.

Our model is interrogated for its predictive capabilities by comparing calcula-

tions against experimental results for monotonic sliding and by performing numerical simulations of the axisymmetric cup-drawing and square pan-drawing of Al6111-T4 blanks lubricated with MP404 and boric acid. The model is deemed to be robust and capable of predicting complicated multi-axial sheet forming operations.

A rate-dependent version of the constitutive model has recently been implemented into ABAQUS/Explicit v5.8 by H. S. Moon. Experiments to ascertain the rate-dependent model parameters are currently underway.

In addition, the research may be extended by developing a temperature dependent constitutive model, by investigating the effects of sliding rates that are orders of magnitude larger than those currently tested, and by striving to further bridge the gap between the tribological perspective of the micromechanics of friction and the macroscopic constitutive models that may serve as valuable predictive tools for industry.

Bibliography

[1] Anand, L., "A Constitutive Model for Interface Friction", *Computational Mechanics.* 12 (1993): 197-213.

[2] Anand, L., and Tong, W., "A Constitutive Model for Friction in Forming", *Annals of the CIRP.* 42 (1993): 361-366.

[3] Pisoni, A.C., *A Constitutive Model for Friction in Metal-Working.* MS Thesis, MIT. 1992.

[4] Courtney-Pratt, J. S., and Eisner, E., "The Effect of a Tangential Force on the Contact of Metallic Bodies", *Proc. of the Royal Society A.* 238 (1957): 529-550.

[5] Kawai, N. and Dohda, K., "A New Lubricity Evaluation Method for Metal Forming by a Compression-Twist Type Friction Testing Machine", *Journal of Tribology.* 109 (1987): 343-350.

[6] Hughes, D., Weingarten, L., and Dawson, D., "Numerical Simulation and Experimental Observations of Initial Friction Transients", *Simulation of Materials Processing: Theory, Methods and Applications.* (1995): 265-270.

[7] Anand, L., and Gu, C., "Granular Materials: Constitutive Equations and Shear Localization", *Submitted to JMPS.*

[8] Anand, L., "Constitutive Equations for the Rate-Dependent Deformation of Metals at Elevated Temperatures", *ASME Journal of Engineering Materials and Technology.* 104 (1982): 12-17.

[9] Gurtin, M.E., *An Introduction to Continuum Mechanics*. Academic Press, New York. 1981.

[10] Gupta, A.K., Marois, P.H.,and Lloyd, D.J., "Study of the Precipitation Kinetics in a 6000 Series Automotive Sheet Material", *Material Science Forum*. 217-222 (1996): 801-808.

[11] Erdemir, A., "Tribological Properties of Boric Acid and Boric-Acid-Forming Surfaces. Part I: Crystal Chemistry and Mechanism of Self-Lubrication of Boric Acid", *Lubrication Engineering*. 47 (1991): 168-173.

[12] Erdemir, A., Fenske, G., Erck, R., Nichols, F., and Busch, D., "Tribological Properties of Boric Acid and Boric-Acid-Forming Surfaces. Part II: Mechanisms of Formation and Self-Lubrication of Boric Acid Films on Boron- and Boric Oxide-Containing Surfaces", *Lubrication Engineering*. 47 (1991): 179-184.

[13] Erdemir, A., and Fenske, G., "Clean and Cost-Effective Dry Boundary Lubricants for Aluminum Forming", Society of Automotive Engineers Report 980453. (1998): 9-17.

[14] Bridgman, P. W., "Shearing Phenomena at High Pressure of Possible Importance to Geology", *Journal of Geology*. 44 (1936): 653-669.

[15] Lee, C.G.Y., *Closed-Loop Control of Sheet Metal Stability During Forming*. MS Thesis, MIT. 1983.

[16] Kothari, M., *Polycrystalline Elasto-Viscoplasticity: Application to B.C.C. Metals*. PhD Thesis, MIT. 1997.

[17] ABAQUS, *Reference Manuals*. Hibbitt, Karlsson, & Sorensen Inc., Pawtucket, RI, 1998.

[18] Cao, J., and Boyce, M. C., "A Predictive Tool for Delaying Wrinkling and Tearing Failures in Sheet Metal Forming", Journal of Engineering Materials and Technology. 119 (1997): 354-365.

Appendix A

Constitutive Model for Friction

This appendix presents the constitutive model for interface friction formulated by Anand [1] and presented as well in [2] and [3]. As an approximation, friction at an interface is considered to be rate-independent and isothermal. Also, the model is fully three-dimensional and isotropic in nature. The theory assumes that the state of a material point at the interface can be fully characterized at any instant by two variables. The first is the applied traction, t, and the second is a scalar internal variable which is called the slip resistance, s, and which has dimensions of stress. The isotropic slip resistance is similar in spirit to the deformation resistance proposed by Anand in [8] to account for cumulative micromechanical effects in isotropic plasticity theory. The value of the slip resistance is related to the pressure at the interface, p, and the accumulated relative tangential slip at the interface, $\overline{u}^s$, through a constitutive equation with experimentally determined parameters.

Another ingredient of the theory is that the tangential component of the relative velocity at the interface is additively decomposed into an adhering component and a slipping component. In analogy to plasticity theory, the adhering and slipping components may be compared to the elastic and plastic strain rates, respectively. Also, the adhering component is assumed to be recoverable, while the slipping portion is non-recoverable and dissipative. The relative tangential slipping velocity is given by a slip rule, where a slipping condition in traction space must be satisfied for slipping to occur. The magnitude of the tangential slipping velocity is defined by a consistency

condition to be discussed in more detail herein.

A.1 Preliminaries

The notation used is now common in continuum mechanics (cf., e.g. Gurtin [9]). Consider two bodies $\mathcal{B}^+$ and $\mathcal{B}^-$, which represent the tool and the workpiece, respectively. With $\mathbf{p}$ representing a material point in the body at time $t = 0$, the motion of each body is given by

$$\mathbf{x}^+ = \hat{\mathbf{x}}^+(\mathbf{p}^+, t) \quad \text{and} \quad \mathbf{x}^- = \hat{\mathbf{x}}^-(\mathbf{p}^-, t). \tag{A.1}$$

The motions of the bodies relative to their current configurations $\mathcal{B}_t^+$ and $\mathcal{B}_t^-$ are given by

$$\boldsymbol{\xi}^+ = \hat{\mathbf{x}}_t^+(\mathbf{x}^+, \tau) \quad \text{and} \quad \boldsymbol{\xi}^- = \hat{\mathbf{x}}_t^-(\mathbf{x}^-, \tau), \tag{A.2}$$

where $\tau = t + \Delta t$. The incremental displacements can then be expressed by

$$\hat{\mathbf{u}}_t^+(\mathbf{x}^+, \tau) = \boldsymbol{\xi}^+ - \mathbf{x}^+ \quad \text{and} \quad \hat{\mathbf{u}}_t^-(\mathbf{x}^-, \tau) = \boldsymbol{\xi}^- - \mathbf{x}^-, \tag{A.3}$$

and the spatial velocities are given by

$$\hat{\mathbf{v}}^+(\mathbf{x}^+, t) = \frac{\partial}{\partial \tau} \hat{\mathbf{u}}_t^+(\mathbf{x}^+, \tau)|_{\tau=t} \quad \text{and} \quad \hat{\mathbf{v}}^-(\mathbf{x}^-, t) = \frac{\partial}{\partial \tau} \hat{\mathbf{u}}_t^-(\mathbf{x}^-, \tau)|_{\tau=t}. \tag{A.4}$$

When the two bodies come into contact, we assume that the region of contact may be considered to be an interface of zero thickness, hence we set $\mathbf{x} \equiv \mathbf{x}^+ = \mathbf{x}^-$. The outward normal to the surface of the workpiece $\mathcal{B}_t^-$ at the point $\mathbf{x}$ under consideration at time t is denoted as $\mathbf{n} = \hat{\mathbf{n}}(\mathbf{x}^-, t)$. The configuration is schematically shown in

46

figure D-47. The relative velocity, $\bar{\mathbf{v}}$, between the tool and workpiece is expressed, with arguments suppressed, by

$$\bar{\mathbf{v}} = \mathbf{v}^+ - \mathbf{v}^-. \tag{A.5}$$

Let

$$\bar{\mathbf{v}}_N = (\mathbf{n} \otimes \mathbf{n})\bar{\mathbf{v}} \equiv \bar{v}_N \mathbf{n} \tag{A.6}$$

and

$$\bar{\mathbf{v}}_T = \{\mathbf{1} - (\mathbf{n} \otimes \mathbf{n})\}\bar{\mathbf{v}} = \bar{\mathbf{v}} - \bar{v}_N \mathbf{n} \tag{A.7}$$

denote the normal and tangential components of the relative velocity vector, respectively.

Next, we define the instantaneous traction exerted by the tool on the workpiece by

$$\mathbf{t} = \mathbf{t}_N + \mathbf{t}_T, \tag{A.8}$$

where

$$\mathbf{t}_N = (\mathbf{n} \otimes \mathbf{n})\mathbf{t} \equiv t_N \mathbf{n} \tag{A.9}$$

and

$$\mathbf{t}_T = \{\mathbf{1} - (\mathbf{n} \otimes \mathbf{n})\}\mathbf{t} = \mathbf{t} - t_N \mathbf{n} \tag{A.10}$$

are the normal and tangential components of the instantaneous traction vector, respectively. We define the normal or contact pressure at the interface by

$$p \equiv -t_N, \tag{A.11}$$

and the effective tangential traction or shear stress by

$$\bar{\tau} \equiv \sqrt{\mathbf{t}_T \cdot \mathbf{t}_T}. \tag{A.12}$$

47

We now define the co-rotational derivative $\mathbf{t}^\circ$ of $\mathbf{t}$ relative to an orthonormal basis $\{\mathbf{e}_1^s(t), \mathbf{e}_2^s(t), \mathbf{e}_3^s(t)\}$ with its origin at $\mathbf{x}^-$ and with $\mathbf{e}_3^s(t) \equiv \mathbf{n}(t)$, as

$$\mathbf{t}^\circ \equiv \sum_i \dot{t}_i \mathbf{e}_i^s = \dot{\mathbf{t}} - \mathbf{\Omega t}. \tag{A.13}$$

The twirl tensor, $\mathbf{\Omega}(t)$, is skew symmetric and is defined by

$$\dot{\mathbf{e}}_i^s(t) = \mathbf{\Omega}(t)\mathbf{e}_i^s(t) \quad \text{with} \quad \mathbf{\Omega}(t) \equiv \frac{\partial}{\partial \tau}\mathbf{R}_t(\tau)|_{\tau=t}, \tag{A.14}$$

and the tensor $\mathbf{R}_t(\tau)$ is an incremental rotation tensor defined by

$$\mathbf{e}_i^s(\tau) = \mathbf{R}_t(\tau)\mathbf{e}_i^s(t), \tag{A.15}$$

with

$$[\mathbf{R}_t(\tau)]^T\mathbf{R}_t(\tau) = \mathbf{R}_t(\tau)[\mathbf{R}_t(\tau)]^T = \mathbf{1}, \quad \det[\mathbf{R}_t(\tau)] = 1, \quad \text{and} \quad \mathbf{R}_t(t) = \mathbf{1}. \tag{A.16}$$

Note that $\mathbf{R}_t(\tau)$ is a proper orthogonal tensor. The co-rotational derivative of $\mathbf{t}$ represents the time derivative of the traction measured by an observer rotating with an orthonormal basis $\{\mathbf{e}_i^s\}$ attached to $\mathbf{p}^-$.

In formulating the constitutive model, we use the pair $(\mathbf{t}^\circ, \overline{\mathbf{v}})$ as defined above. We must guarantee that these variables are frame indifferent or objective. Note that in order for a vector, $\mathbf{a}$, to be objective, it must transform during a change in observer to $\mathbf{a}^*$ as

$$\mathbf{a}^* = \mathbf{Qa} \tag{A.17}$$

where $\mathbf{Q}$ is a proper orthogonal rotation tensor. First, we consider the relative veloc-

48

ity, $\bar{\mathbf{v}}$. Recall that under a change in observer

$$\hat{\mathbf{x}}^*(\mathbf{p}, t) = \mathbf{c}(t) + \mathbf{Q}(t)\{\hat{\mathbf{x}}(\mathbf{p}, t) - \mathbf{0}\}, \tag{A.18}$$

for every material point $\mathbf{p}$ and time t, where $\mathbf{c}(t)$ is a point in space and $\mathbf{Q}(t)$ is a rotation. Differentiating equation A.18 with respect to time, the transformation rules for the velocities $\hat{\mathbf{v}}^+(\mathbf{x}^+, t)$ and $\hat{\mathbf{v}}^-(\mathbf{x}^-, t)$ are

$$\hat{\mathbf{v}}^{+*}(\mathbf{x}^{+*}, t) = \dot{\mathbf{c}}(t) + \mathbf{Q}(t)\hat{\mathbf{v}}^+(\mathbf{x}^+, t) + \dot{\mathbf{Q}}(t)\{\mathbf{x}^+ - \mathbf{0}\} \tag{A.19}$$

and

$$\hat{\mathbf{v}}^{-*}(\mathbf{x}^{-*}, t) = \dot{\mathbf{c}}(t) + \mathbf{Q}(t)\hat{\mathbf{v}}^-(\mathbf{x}^-, t) + \dot{\mathbf{Q}}(t)\{\mathbf{x}^- - \mathbf{0}\}. \tag{A.20}$$

Subtracting equation A.20 from equation A.19 gives the transformation rule for the relative velocity:

$$\bar{\mathbf{v}}^* = \mathbf{Q}\bar{\mathbf{v}} \tag{A.21}$$

Hence, in accord with equation A.17, the relative velocity is an objective or frame indifferent tensor.

In considering the co-rotational derivative of $\mathbf{t}$, we first note that the traction and our orthonormal basis transform as

$$\mathbf{t}^* = \mathbf{Q}\mathbf{t} \quad \text{and} \quad (\mathbf{e}_i^s)^* = \mathbf{Q}\mathbf{e}_i^s, \tag{A.22}$$

respectively. Taking the time derivative of equation A.22 gives

$$\dot{\mathbf{t}}^* = \dot{\mathbf{Q}}\mathbf{t} + \mathbf{Q}\dot{\mathbf{t}} \quad \text{and} \quad \overline{(\mathbf{e}_i^s)^*} = \dot{\mathbf{Q}}\mathbf{e}_i^s + \mathbf{Q}\dot{\mathbf{e}}_i^s, \tag{A.23}$$

49

and by using equations A.14 and A.22b, equation A.23b becomes

$$\overline{\dot{(\mathbf{e}_i^s)^*}} = \dot{\mathbf{Q}}\mathbf{Q}^T(\mathbf{e}_i^s)^* + \mathbf{Q}\boldsymbol{\Omega}\mathbf{Q}^T(\mathbf{e}_i^s)^*. \tag{A.24}$$

We have thus found the transformation rule for the twirl tensor $\boldsymbol{\Omega}$ under a change in observer:

$$\overline{\dot{(\mathbf{e}_i^s)^*}} = \boldsymbol{\Omega}^*(\mathbf{e}_i^s)^* \quad \text{therefore} \quad \boldsymbol{\Omega}^* = \dot{\mathbf{Q}}\mathbf{Q}^T + \mathbf{Q}\boldsymbol{\Omega}\mathbf{Q}^T. \tag{A.25}$$

Using the definition of the co-rotational derivative under a change in observer along with equations A.22, A.23, and A.25 we find

$$\mathbf{t}^{\circ *} = \overline{\dot{\mathbf{t}^*}} - \boldsymbol{\Omega}^*\mathbf{t}^* \tag{A.26}$$

$$\mathbf{t}^{\circ *} = \dot{\mathbf{Q}}\mathbf{t} + \mathbf{Q}\dot{\mathbf{t}} - (\dot{\mathbf{Q}}\mathbf{Q}^T + \mathbf{Q}\boldsymbol{\Omega}\mathbf{Q}^T)\mathbf{Q}\mathbf{t} \tag{A.27}$$

$$\mathbf{t}^{\circ *} = \mathbf{Q}(\dot{\mathbf{t}} - \boldsymbol{\Omega}\mathbf{t}) \tag{A.28}$$

$$\mathbf{t}^{\circ *} = \mathbf{Q}\mathbf{t}^{\circ}. \tag{A.29}$$

Therefore, the co-rotational derivative $\mathbf{t}^{\circ}$ is frame indifferent.

Finally, it is necessary to show that the quantities $\mathbf{R}_t(\tau)$ and $\boldsymbol{\Omega}(t)$ can be calculated given the motion $\hat{\mathbf{x}}_t^-(\mathbf{x}^-, \tau)$. As suggested by Anand [1], we define the surface deformation gradient corresponding to a given motion and its polar decomposition by

$$\hat{\mathbf{F}}_t^-(\mathbf{x}^-, \tau) = \frac{\partial}{\partial \mathbf{x}^-}\hat{\mathbf{x}}_t^-(\mathbf{x}^-, \tau), \tag{A.30}$$

with

$$\hat{\mathbf{F}}_t^-(\mathbf{x}^-, \tau) = \hat{\mathbf{R}}_t^-(\mathbf{x}^-, \tau)\hat{\mathbf{U}}_t^-(\mathbf{x}^-, \tau). \tag{A.31}$$

Reasonable choices for $\mathbf{R}_t(\tau)$ and $\Omega(t)$ are then

$$\mathbf{R}_t(\tau) \equiv \hat{\mathbf{R}}_t^-(\mathbf{x}^-, \tau) \tag{A.32}$$

and

$$\Omega(t) \equiv \hat{\mathbf{W}}^-(\mathbf{x}^-, t) = \frac{\partial}{\partial \tau} \hat{\mathbf{R}}_t^-(\mathbf{x}^-, \tau)|_{\tau=t}. \tag{A.33}$$

With the background information in this section, we proceed with the formulation of the interface constitutive model for friction.

A.2 Constitutive Model

The variables governing the response of an element of a contacting interface between a workpiece and a tool are taken to be the pair $(\mathbf{t}, s)$, where $\mathbf{t}$ is the traction and s is the slip resistance. The model is presented in subdivisions which are chosen to make the analogy between our friction model and the classical J_2 flow theory of rate-independent isotropic plasticity more explicit.

Relative Adhering Velocity

Recall that the relative tangential velocity is decomposed according to $\bar{\mathbf{v}} = \bar{\mathbf{v}}_N + \bar{\mathbf{v}}_T$. As suggested by the experimental results of Courtney-Pratt and Eisner [4], we additively decompose the relative tangential velocity, $\bar{\mathbf{v}}_T$, into an adhering and a slipping part

$$\bar{\mathbf{v}}_T \equiv \bar{\mathbf{v}}^a + \bar{\mathbf{v}}^s. \tag{A.34}$$

Constitutive Equation for $\mathbf{t}$

The evolution of the co-rotational derivative of the traction is taken to be governed by

$$\mathbf{t}^\circ = \mathbf{K}[\bar{\mathbf{v}}_N + \bar{\mathbf{v}}^a] = \mathbf{K}[\bar{\mathbf{v}} - \bar{\mathbf{v}}^s], \tag{A.35}$$

where

$$\mathbf{K} \equiv [k_N(\mathbf{n} \otimes \mathbf{n}) + k_T(\mathbf{1} - \mathbf{n} \otimes \mathbf{n})] \tag{A.36}$$

is the second order isotropic stiffness tensor for adherence, with $k_N > 0$ and $k_T > 0$ the normal and tangential stiffnesses in adherence, respectively. Note that the co-rotational derivative of the traction may be written in component form as

$$\mathbf{t}_N^\circ = k_N \bar{\mathbf{v}}_N \quad \text{and} \quad \mathbf{t}_T^\circ = k_T(\bar{\mathbf{v}}_T - \bar{\mathbf{v}}^s) = k_T(\bar{\mathbf{v}}^a). \tag{A.37}$$

Slip Condition

We prescribe a slip condition in our model given by a scalar valued function $\hat{f}(\mathbf{t}, s)$ with values

$$\hat{f}(\mathbf{t}, s) \equiv \overline{\tau} - s \leq 0, \qquad (A.38)$$

with $s = \hat{s}(p, \underline{\alpha})$, where $\underline{\alpha}$ denotes the "state" of the interface. The surface $\hat{f}(\mathbf{t}, s) = 0$ defines the current slip surface in traction space, and the outward normal to the slip surface at the current traction point is

$$\overline{\mathbf{m}} \equiv \frac{\partial}{\partial \mathbf{t}} \hat{f}(\mathbf{t}, s). \qquad (A.39)$$

If the current traction is within the slip surface, or if it is on the slip surface and a trial traction rate $\mathbf{K}[\overline{\mathbf{v}}]$ points toward the interior side of the tangent plane to the slip surface, that is if $\overline{\mathbf{m}} \cdot \mathbf{K}[\overline{\mathbf{v}}] \leq 0$, then the process is considered to be adhering. Otherwise, the process is slipping.

Flow Rule

The relative tangential slipping velocity $\overline{\mathbf{v}}^s$ is given by the slip or flow rule

$$\overline{\mathbf{v}}^s = \overline{v}^s \mathbf{m}, \qquad (A.40)$$

with

$$\overline{v}^s = |\overline{\mathbf{v}}^s| \geq 0 \quad \text{and} \quad \mathbf{m} \equiv \frac{\mathbf{t}_T}{\overline{\tau}}. \qquad (A.41)$$

The magnitude $\overline{v}^s$ is termed the effective relative tangential slipping velocity and is a positive valued scalar to be determined by the consistency condition presented below. Also, $\mathbf{m}$ is a unit vector defining the slip direction, which is taken to be in the

direction of the tangential traction. Note that since we have chosen

$$\mathbf{m} \neq \overline{\mathbf{m}} \equiv \frac{\partial}{\partial \mathbf{t}} \hat{f}(\mathbf{t}, s), \qquad \text{(A.42)}$$

the flow rule is non-associated.

Hardening Rule

We assume that the state of the interface $\underline{\alpha}$ is adequately characterized by the accumulated relative tangential slip at the interface, $\overline{u}^s$, which evolves according to

$$\dot{\overline{u}}^s \equiv \overline{v}^s, \qquad \text{(A.43)}$$

with initial value

$$\overline{u}^s(0) = 0. \qquad \text{(A.44)}$$

In this case, the slip resistance is specified by the constitutive equation

$$s = \hat{s}(p, \overline{u}^s) \geq 0, \qquad \text{(A.45)}$$

and the evolution equation for the slip resistance, or hardening rule, becomes

$$\dot{s} = h_N \dot{p} + h_T \overline{v}^s, \qquad \text{(A.46)}$$

where

$$h_N \equiv \frac{\partial s}{\partial p} \quad \text{and} \quad h_T \equiv \frac{\partial s}{\partial \overline{u}^s} \qquad \text{(A.47)}$$

are hardening functions which account for changes in the slip resistance with changes in the contact pressure and the relative tangential slip, respectively.

Kuhn-Tucker Complementarity Condition

Using the above definitions, the Kuhn-Tucker complementarity condition is specified by

$$\bar{v}^s \geq 0, \quad f \leq 0, \quad \text{therefore} \quad \bar{v}^s f = 0. \tag{A.48}$$

Consistency Condition

The consistency condition, given by

$$\bar{v}^s \dot{f} = 0 \quad \text{if} \quad f = 0, \tag{A.49}$$

ensures that our slip condition is satisfied during a slipping process.

Magnitude of $\bar{v}^s$

In order to determine the magnitude of $\bar{v}^s$, we take the time derivative of equation A.38

$$\dot{f} = \frac{\partial f}{\partial \bar{\tau}}\dot{\bar{\tau}} + \frac{\partial f}{\partial s}\dot{s} \leq 0 \tag{A.50}$$

Consideration of equations A.11, A.12, and A.45 gives

$$\dot{f} = \frac{\partial f}{\partial \bar{\tau}}\frac{\partial \bar{\tau}}{\partial \mathbf{t}} \cdot \dot{\mathbf{t}} + \frac{\partial f}{\partial s}\left\{ \left[h_N \frac{\partial p}{\partial \mathbf{t}} \right] \cdot \dot{\mathbf{t}} + h_T \bar{v}^s \right\} \leq 0. \tag{A.51}$$

Using the results

$$\frac{\partial \bar{\tau}}{\partial \mathbf{t}} = \frac{\mathbf{t}_T}{\bar{\tau}} \quad \text{and} \quad \frac{\partial p}{\partial \mathbf{t}} = -\mathbf{n}, \tag{A.52}$$

and noting that the outward normal to the slip surface may be expressed by

55

$$\overline{\mathbf{m}} \equiv \frac{\partial}{\partial \mathbf{t}} \hat{f}(\mathbf{t}, s) = \frac{\partial f}{\partial \mathcal{T}} \mathbf{m} - h_N \frac{\partial f}{\partial \mathcal{S}} \mathbf{n} = \mathbf{m} + h_N \mathbf{n}, \qquad (A.53)$$

we rewrite equation A.51 as

$$\dot{f} = \overline{\mathbf{m}} \cdot \dot{\mathbf{t}} - h_T \overline{v}^s \leq 0. \qquad (A.54)$$

Furthermore, we use equations A.35 and A.40 and the results

$$\overline{\mathbf{m}} \cdot \dot{\mathbf{t}} = \overline{\mathbf{m}} \cdot \mathbf{t}^{\circ} \quad \text{and} \quad \overline{\mathbf{m}} \cdot \mathbf{K}[\mathbf{m}] = k_T \qquad (A.55)$$

to arrive at

$$\dot{f} = \overline{\mathbf{m}} \cdot \mathbf{K}[\overline{\mathbf{v}}] - (k_T + h_T)\overline{v}^s \leq 0, \qquad (A.56)$$

and assuming that

$$g \equiv (k_T + h_T) > 0 \qquad (A.57)$$

gives the magnitude of $\overline{v}^s$ as

$$\overline{v}^s = \begin{cases} 0 & \text{if} \quad f < 0 \quad \text{or} \quad f = 0 \quad \text{and} \quad \overline{\mathbf{m}} \cdot \mathbf{K}[\overline{\mathbf{v}}] \leq 0, \\ g^{-1}\overline{\mathbf{m}} \cdot \mathbf{K}[\overline{\mathbf{v}}] & \text{if} \quad f = 0 \quad \text{and} \quad \overline{\mathbf{m}} \cdot \mathbf{K}[\overline{\mathbf{v}}] > 0. \end{cases} \qquad (A.58)$$

Summary of Constitutive Model

In summary, the isotropic, rate-independent, isothermal interface constitutive model consists of the following set of coupled evolution equations for $(\mathbf{t}, s)$:

1. Evolution equation for the traction $\mathbf{t}$:

$$\mathbf{t}^{\circ} = \mathbf{K}[\overline{\mathbf{v}}_N + \overline{\mathbf{v}}^a] = \mathbf{K}[\overline{\mathbf{v}} - \overline{\mathbf{v}}^s], \tag{A.59}$$

where

$$\mathbf{K} \equiv [k_N(\mathbf{n} \otimes \mathbf{n}) + k_T(\mathbf{1} - \mathbf{n} \otimes \mathbf{n})] \tag{A.60}$$

is the second order isotropic stiffness tensor for adherence, with $k_N > 0$ and $k_T > 0$ the normal and tangential stiffnesses in adherence, respectively. The relative tangential slipping velocity is given by the slip rule

$$\overline{\mathbf{v}}^s = \overline{v}^s \mathbf{m}, \tag{A.61}$$

where

$$\mathbf{m} \equiv \frac{\mathbf{t}_T}{\overline{\tau}} \tag{A.62}$$

is the unit vector in the direction of the tangential traction,

$$\overline{\tau} \equiv \sqrt{\mathbf{t}_T \cdot \mathbf{t}_T}. \tag{A.63}$$

is an effective tangential traction or shear stress, and $\overline{v}^s$ is an effective relative tangential slipping velocity given by

$$
\overline{v}^s = \begin{cases} 0 & \text{if } f < 0 \text{ or } f = 0 \text{ and } \overline{\mathbf{m}} \cdot \mathbf{K}[\overline{\mathbf{v}}] \leq 0, \\ g^{-1}\overline{\mathbf{m}} \cdot \mathbf{K}[\overline{\mathbf{v}}] & \text{if } f = 0 \text{ and } \overline{\mathbf{m}} \cdot \mathbf{K}[\overline{\mathbf{v}}] > 0, \end{cases} \tag{A.64}
$$

where

$$
g \equiv k_T + h_T \tag{A.65}
$$

and

$$
\overline{\mathbf{m}} \equiv \mathbf{m} + h_N \mathbf{n} \tag{A.66}
$$

is the normal to the slip surface $\overline{\tau} - s = 0$. If preferred, the evolution equation for the traction may be expressed as

$$
\mathbf{t}^\circ = \mathbf{M}[\overline{\mathbf{v}}], \tag{A.67}
$$

where

$$
\mathbf{M} \equiv \mathbf{K} - g^{-1}k_T \left\{ k_N h_N (\mathbf{m} \otimes \mathbf{n}) + k_T (\mathbf{m} \otimes \mathbf{m}) \right\} \tag{A.68}
$$

is the second order adhering-slipping stiffness tensor.

2. Evolution equation for the slip resistance s:

We assume the slip resistance to be given by

$$
s = \hat{s}(p, \overline{u}^s) \geq 0, \quad with \quad \hat{s}(0, \overline{u}^s) = s_{th}, \tag{A.69}
$$

where $p = -t_N$ is the contact pressure, s_{th} is a threshold value of the slip resistance, and $\overline{u}^s$ is the accumulated relative tangential slip whose evolution is governed by

$$\dot{\overline{u}}^s \equiv \overline{v}^s, \tag{A.70}$$

with initial value

$$\overline{u}^s(0) = 0. \tag{A.71}$$

The evolution of s is then

$$\dot{s} = h_N \dot{p} + h_T \overline{v}^s, \tag{A.72}$$

where

$$h_N \equiv \frac{\partial s}{\partial p} \quad \text{and} \quad h_T \equiv \frac{\partial s}{\partial \overline{u}^s} \tag{A.73}$$

are hardening functions which account for changes in the slip resistance with changes in the contact pressure and the relative tangential slip, respectively.

To complete the constitutive model for a particular tool and workpiece interface, the parameters / functions that need to be specified are the normal and tangential stiffnesses in adherence, k_N and k_T, respectively, and the constitutive equation for the slip resistance s, or equivalently, the initial value of the slip resistance and the hardening functions h_N and h_T.

Appendix B

Results for Cyclic Sliding

B.1 MP404 Lubricant

Due to machine and tooling limitations, the total sliding distance possible in the monotonic tests is around 20 mm. In order to allow for very large sliding distances in the meter and perhaps even kilometer range, cyclic loading is the only option using the current apparatus. The linear sliding rate of 1 mm/s is obtained by programming a linear displacement versus time or 'sawtooth' waveform into the Instron. The frequency is set at 0.0246 Hz, which, given the mean tool diameter, allows for a sliding velocity of 1 mm/s. The Instron rotates around the zero degree mark in forty-five degree increments, which gives a total sliding distance per cycle of 40 mm.

An example of a cyclic sliding test for the MP404 lubricated Al6111-T4 and tool steel interface at a normal pressure of 100 MPa is shown in figure D-48, where the signs of the shear stress and sliding distance indicate different directions of sliding. The initial 20 mm of sliding of the cyclic loop — marked by '1' — indicates a similar hardening behavior as that shown in figure D-15 for monotonic sliding. The next two sliding passes of 20 mm — '2' and '3', respectively — each essentially maintain the saturation value of the first 20 mm pass. However, as the fourth pass of 20 mm progresses — see '4' — a marked softening of the shear stress response occurs. With continued sliding, the cyclic loop softens to a stable value which gives a symmetric curve about the origin of figure D-48. This behavior is better observed by applying

a Matlab program that takes the average value of the shear stress and accumulated sliding in each direction of displacement and builds a curve of the absolute value of the shear stress versus the accumulated sliding distance (see Routine 7 in Appendix C). The result of the data smoothing is shown in figure D-49. A softening behavior of the shear stress with sliding distance is clearly represented by the data.

The pressure dependency of the peaking behavior is shown in figure D-50, which presents curves for normal pressures of 30 MPa, 100 MPa, and 200 MPa. This data may be compared with the shear stress versus sliding distance data for granular media presented by Anand and Gu [7], where a similar friction model is incorporated.

A comparison of the results for the MP404 lubricated Al6111-T4 and tool steel interface under monotonic sliding and cyclic sliding suggests the possibility of simplifying the current model to apply to two separate regimes. The first is in analogy to the work in [3] and [2] where the possibility of softening at the interface is not addressed. The cyclic sliding data in figure D-48 implies that softening is not initiated until after about 60 mm of sliding, hence a model neglecting the effects of softening may be applied. Depending on the process being modeled, a sliding distance of 60 mm may be adequate. Note that the test at 100 MPa is assumed to provide a reasonable average for the maximum distance slid before softening occurs over the range of pressures considered.

In conducting experimentation, it is necessary to isolate the response of the specimen from coupling with the machine response. Due to the possibility of 'backlash' at the interface with the knurling, tests using a different configuration are performed to verify that the obtained measurements indeed indicate the desired interfacial response. A cylindrical specimen of Al6061-T6 with a diameter of 50 mm and height of 125 mm with a ground surface finish is coated with MP404 and loaded by the tool to 200 MPa with cyclic sliding. The result of the test is shown in figure D-51, where a similar behavior to that of the MP404 lubricated Al6111-T4 sheet is observed. Apparently, a knurling 'backlash' is not a factor in the experimental results.

B.2 Boric Acid

In order to achieve large sliding distances, cyclic sliding tests are conducted for the boric acid lubricated Al6111-T4 and tool steel interface. The shear stress versus accumulated sliding distance is shown in figures D-52 and D-53 for normal pressures of 20 MPa and 200 MPa, respectively. While the test at $p = 20$ MPa decreases to a relatively constant shear stress after about 180 mm of sliding, the test at $p = 200$ MPa markedly increases to a shear stress corresponding to dry sliding. An inspection of the specimens after testing shows that the integrity of the boric acid layer for the low pressure test is not degraded, whereas the boric acid layer broke into fragments at the high pressure test and lost all lubricating capacity. The results at $p = 200$ MPa should be compared with those of $p = 200$ MPa in figure D-50 for the MP404 lubricant. The lubricating capacity of the MP404 lubricant clearly surpasses that of the boric acid film once sliding distances greater than 250 mm are attained.

Appendix C

Matlab Routines

C.1 Routine 1

```
%%%%%%%%%%%%%%%%%%%%%%%%%%%%%%%%%%%%%%%%%%%%%%%%%%%%%%%%%%%%%%%%%%%

%  12/12/97   --   Rev1   --   BPG.

%  Curve-fitting algorithm for the integrated form of the

%  deformation resistance versus the plastic strain.

%%%%%%%%%%%%%%%%%%%%%%%%%%%%%%%%%%%%%%%%%%%%%%%%%%%%%%%%%%%%%%%%%%%

%

% Load data file

%

load filename.dat

%

% set the plastic strain ep equal to corresponding raw data value

%

for n = 1:length(filename(:,2));

ep(n) = filename(n,2);

end

%

% Set equation parameters (in MPa)

%
```

```
so = 106;
ss = 291;
ho = 150;
a = 2.0;
c = (1-a);
%
% Calculate the deformation resistance sf at each plastic
% strain value via
%
m=length(ep);
for i=1:m;
sf(i)=ss*(1-(((-c*ho*ep(i)/ss)+((1-so/ss)^c))^(1/c)));
end
%
% Plot the predicted curve of sf versus ep
%
plot(ep,sf,'k-')
%
%%%%%%%%%%%
```

C.2 Routine 2

```
%%%%%%%%%%%%%%%%%%%%%%%%%%%%%%%%%%%%%%%%%%%%%%%%%%%%%%%%%%%%%%%%
% 12/12/98    --    Rev1    --    BPG.
% Curve-fitting algorithm for the integrated form of the friction
% coefficient as a function of the sliding distance. Note that
% SI units are used.
%%%%%%%%%%%%%%%%%%%%%%%%%%%%%%%%%%%%%%%%%%%%%%%%%%%%%%%%%%%%%%%%
%
% Set pressure corresponding to experimental data
%
p=100;
%
% Set equation parameters
%
muo=0.11;
muk=0.32;
h=1;
r=4;
c=(1-r);
etao=0.15;
hb=0.0025;
%
% Calculate mu(i) where i is the sliding distance
%
for i=1:36;
mu(i)=muk*(1-(((-c*h*(i-1)/muk)+((1-muo/muk)^c))^(1/c)));
eta(i)=etao*exp(hb*(muk-mu(i)));
us(i)=i-1;
end
```

```
%
% Plot equation prediction against experimental data
%
figure(1)
plot(us,mu,'y-')
%
% Plot eta as a function of sliding distance
%
figure(2)
plot(us,eta,'r-')
%
%
%%%%%%%%%%
```

C.3 Routine 3

```
%%%%%%%%%%%%%%%%%%%%%%%%%%%%%%%%%%%%%%%%%%%%%%%%%%%%%%%%%%%%%
%  12/21/98   --   Rev1   --   BPG.
%  Curve-fitting algorithm for the evolution of s* with the
%  sliding distance. SI units are used.
%%%%%%%%%%%%%%%%%%%%%%%%%%%%%%%%%%%%%%%%%%%%%%%%%%%%%%%%%%%%%
%
% Record the pressure corresponding to experimental data
%
p=600;
%
% Set equation parameters
%
u2=120;
si=60;
ss=200;
%
% Calculate the saturation value for a given sliding distance
% where i is the sliding distance
%
for i=1:36;
s(i)=si+(ss-si)*(1-exp(-(i-1)/u2));
us(i)=i-1;
end
%
% Plot equation prediction against experimental data
%
plot(us,s,'k-')
%%%%%%%%%%%%
```

C.4   Routine 4

```
%%%%%%%%%%%%%%%%%%%%%%%%%%%%%%%%%%%%%%%%%%%%%%%%%%%%%%%%%%%%%%%%

%  12/21/98   --   Rev1   --   BPG.

%  Curve-fitting algorithm for the evolution of s with the

%  sliding distance at fixed normal pressures using the model

%  parameters obtained for the friction coefficient as a

%  function of sliding distance and for s* as a function of

%  sliding distance. SI units are used.

%%%%%%%%%%%%%%%%%%%%%%%%%%%%%%%%%%%%%%%%%%%%%%%%%%%%%%%%%%%%%%%%

%

% Set initial parameters previously obtained

%

mulow=0.15;

pcrit=25;

muo=0.11;

muk=0.32;

h=1;

r=4;

c=(1-r);

so=60;

ss=200;

u2=120;

%

% Specify a normal pressure for the fit as i. Note that the

% normal pressure is i-1 since an array index cannot be 0. Thus,

% i = 401 would be a normal pressure of 400 MPa.

%

for i=401:401;

%
```

```
% The nested loop gives the sliding distance as j in increments
% of 0.1 mm, which may be refined if desired.
%
for j=1:310;
mu(j)=muk*(1-(((-c*h*((j-1)/10)/muk)+((1-muo/muk)^c))^(1/c)));
s(j)=so+(ss-so)*(1-exp(-((j-1)/10)/u2));
%
% Enforce the conditions on the critical pressure via
%
if (i-1) < pcrit;
sp(j) = mulow*(i-1);
else
sp(j)=mulow*pcrit+s(j)*tanh(mu(j)*((i-1)-pcrit)/s(j));
end
%
% Specify the sliding distance in mm
%
d(j)=(j-1)/10;
end
%
% Plot the model against the experiment at the corresponding
% normal pressure and then update the sliding distance
%
plot(d,sp,'y-')
%
% Update the pressure if calculating at variable pressures
%
end
%%%%%%%%%%%%
```

C.5 Routine 5

```
%%%%%%%%%%%%%%%%%%%%%%%%%%%%%%%%%%%%%%%%%%%%%%%%%%%%%%%%%%%%%%%%%%
% 1/26/99   --   Rev1   --   BPG.
% Curve-fitting algorithm for the incremental form of the friction
% coefficient as a function of the sliding distance. Note that SI
% units are used.
%%%%%%%%%%%%%%%%%%%%%%%%%%%%%%%%%%%%%%%%%%%%%%%%%%%%%%%%%%%%%%%%%%
%
% Record the pressure corresponding to experimental data
%
pressure=20;
%
% Specify initial guesses of equation constants.
%
v = 1;
dt = 0.01;
%
% Since the calculation is in incremental form, the sliding
% velocity v is specified (in mm/s) and the time increment dt
% is also specified (in seconds).
%
muk = 0.0606;
muo = 0.088;
eto = 0.12;
etcr = 0.10;
b = 2.0;
q = 3.0;
hb = 2.5;
hm = 0.3;
```

```
r = 2.5;
%
% Initialize variables (note that u is the sliding distance)
%
for j=1:1;
  mu(j)=muo;
  et(j)=eto;
  if eto >= etcr
    mus(j) = muk + b*(et(j)-etcr)^q;
  else
    mus(j) = muk;
  end
u(j) = j-1;
end
%
% March forward in time and calculate values explicitly via
%
for i=2:3500;
%
% i is an array index that scales with the chosen dt value
%
et(i) = et(i-1)*(1+hb*(muk - mu(i-1)))*v*dt;
  if et(i) >= etcr
    mus(i) = muk + b*(et(i)-etcr)^q;
  else
    mus(i) = muk;
  end
mu(i) = mu(i-1) + hm*(abs(1 - (mu(i-1)/mus(i-1)))^r)*
+                 sign(1 - (mu(i-1)/mus(i-1)))*v*dt;
u(i) = (i-1)/100;
```

```
end
%
% Compare the results against the corresponding experimental
% data at the set pressure.
%
figure(1)
plot(u,mu,'y-')
%
% Track the evolution of eta via
%
figure(2)
plot(u,et,'ro')
%
%
%%%%%%%%%%
```

C.6   Routine 6

```
%%%%%%%%%%%%%%%%%%%%%%%%%%%%%%%%%%%%%%%%%%%%%%%%%%%%%%%
%  1/26/99    --    Rev1    --    BPG.
%  Curve-fitting algorithm for the evolution of s with the
%  sliding distance at fixed normal pressures using the model
%  parameters obtained for the friction coefficient as a
%  function of sliding distance and for s* as a function of
%  sliding distance. SI units are used.
%%%%%%%%%%%%%%%%%%%%%%%%%%%%%%%%%%%%%%%%%%%%%%%%%%%%%%%
%
% Input initial fit values of equation constants.
%
v = 1;
dt = 0.1;
muk = 0.0606;
muo = 0.088;
eto = 0.12;
etcr = 0.10;
b = 2.0;
q = 3.0;
hb = 2.5;
hm = 0.3;
r = 2.5;
%
% Initialize variables (note that u is the sliding distance)
%
for j=1:1;
  mu(j)=muo;
  et(j)=eto;
```

```
  if eto >= etcr
    mus(j) = muk + b*(et(j)-etcr)^q;
  else
    mus(j) = muk;
  end
u(j) = j-1;
end
%
% Move forward in time and calculate values explicitly
%
for i=2:360;
et(i) = et(i-1)*(1+hb*(muk - mu(i-1)))*v*dt;
  if et(i) >= etcr
    mus(i) = muk + b*(et(i)-etcr)^q;
  else
    mus(i) = muk;
  end
mu(i) = mu(i-1) + hm*(abs(1 - (mu(i-1)/mus(i-1)))^r)*
+                  sign(1 - (mu(i-1)/mus(i-1)))*v*dt;
u(i) = (i-1)/10;
%
% Calculate saturation values at the corresponding sliding
% distance
%
u2=1.6;
ui=55.6;
us=36.1;
s(1)=ui;
s(i)=ui+(us-ui)*(1-exp(-((i-1)/10)/u2));
%
```

```
% Set normal pressures n and calculate the corresponding
% slip resistance
%
n=20;
sp1(1)=s(1)*tanh(mu(1)*(n)/s(1));
sp1(i)=s(i)*tanh(mu(i)*(n)/s(i));
n=40;
sp2(1)=s(1)*tanh(mu(1)*(n)/s(1));
sp2(i)=s(i)*tanh(mu(i)*(n)/s(i));
n=100;
sp3(1)=s(1)*tanh(mu(1)*(n)/s(1));
sp3(i)=s(i)*tanh(mu(i)*(n)/s(i));
n=200;
sp4(1)=s(1)*tanh(mu(1)*(n)/s(1));
sp4(i)=s(i)*tanh(mu(i)*(n)/s(i));
n=400;
sp5(1)=s(1)*tanh(mu(1)*(n)/s(1));
sp5(i)=s(i)*tanh(mu(i)*(n)/s(i));
n=600;
sp6(1)=s(1)*tanh(mu(1)*(n)/s(1));
sp6(i)=s(i)*tanh(mu(i)*(n)/s(i));
end
%
% Compare calculation results to experimental
% data at various fixed pressures
%
figure(1)
plot(u,sp1,'y-')
plot(u,sp2,'y-')
plot(u,sp3,'y-')
```

```
figure(2)
plot(u,sp4,'y-')
plot(u,sp5,'y-')
plot(u,sp6,'y-')
%
%
%%%%%%%%%%%%
```

C.7 Routine 7

```
%%%%%%%%%%%%%%%%%%%%%%%%%%%%%%%%%%%%%%%%%%%%%%%%%%%%%%%%%%%%%%%
%  11/21/98   --   Rev1   --   BPG.
%  Data smoothing algorithm to take data from a cyclic friction
%  test and produce a plot of the absolute value of the shear
%  stress versus the accumulated sliding distance.
%%%%%%%%%%%%%%%%%%%%%%%%%%%%%%%%%%%%%%%%%%%%%%%%%%%%%%%%%%%%%%%
%
% Enter raw data file to be processed:
%
file=FMS2C42H;
%
% Convert data to one direction of sliding
%
off=file(1,1);
td(1)=file(1,1);
for i=1:length(file(:,1));
d(i)=file(i,1)-off;
  if d(i) < 0
    dp(i) = -1*d(i);
  else
    dp(i) = d(i);
  end
end
%
for i=1:length(file(:,1))-1;
  if dp(i+1) < dp(i)
    td(i+1)=(dp(i)-dp(i+1))+td(i);
  else
```

```
        td(i+1)=(dp(i+1)-dp(i))+td(i);
    end
end
%
for i=1:length(file(:,2));
s(i)=file(i,2);
end
%
% Take average for each sliding direction
%
k1=0;
k2=0;
k3=0;
for i=1:length(file(:,1))-1;
    if sign(s(i)) == sign(s(i+1))
        if s(i) >= 0
            sp(k1+1)=s(i);
            dp(k1+1)=td(i);
            k1=k1+1;
        else
            sn(k2+1)=s(i);
            dn(k2+1)=td(i);
            k2=k2+1;
        end
    elseif s(i) >= 0
        if k1 == 0
            sm(k3+1)=s(i);
            dm(k3+1)=td(i);
            k3=k3+1;
        else
```

```matlab
        sm(k3+1)=(sum(sp(1:k1)))/k1;

        dm(k3+1)=(sum(dp(1:k1)))/k1;

        k3=k3+1;

        k1=0;

      end

    else

      if k2 == 0

        sm(k3+1)=s(i);

        dm(k3+1)=td(i);

        k3=k3+1;

      else

        sm(k3+1)=(sum(sn(1:k2)))/k2;

        dm(k3+1)=(sum(dn(1:k2)))/k2;

        k3=k3+1;

        k2=0;

      end

    end

end

%

% Construct a plot of the absolute value of the shear

% stress versus the accumulated sliding distance via

%

for i=1:length(sm);

  if sm(i) < 0

    smc(i) = -1*sm(i);

  else

    smc(i) = sm(i);

  end

end

%
```

```matlab
% Construct a plot of the average of the absolute value
% of the shear stress versus the average value of the
% accumulated sliding distance
%
k4=0;
if rem(length(smc),2) == 0
  for i=1:2:length(smc)-1;
    smmc3(k4+1)=mean(smc(i:i+1));
    dmm3(k4+1)=mean(dm(i:i+1));
    k4=k4+1;
  end
else
  for i=1:2:length(smc)-2;
    smmc3(k4+1)=mean(smc(i:i+1));
    dmm3(k4+1)=mean(dm(i:i+1));
    k4=k4+1;
  end
end
%
%%%%%%%%%%
```

Appendix D

Figures
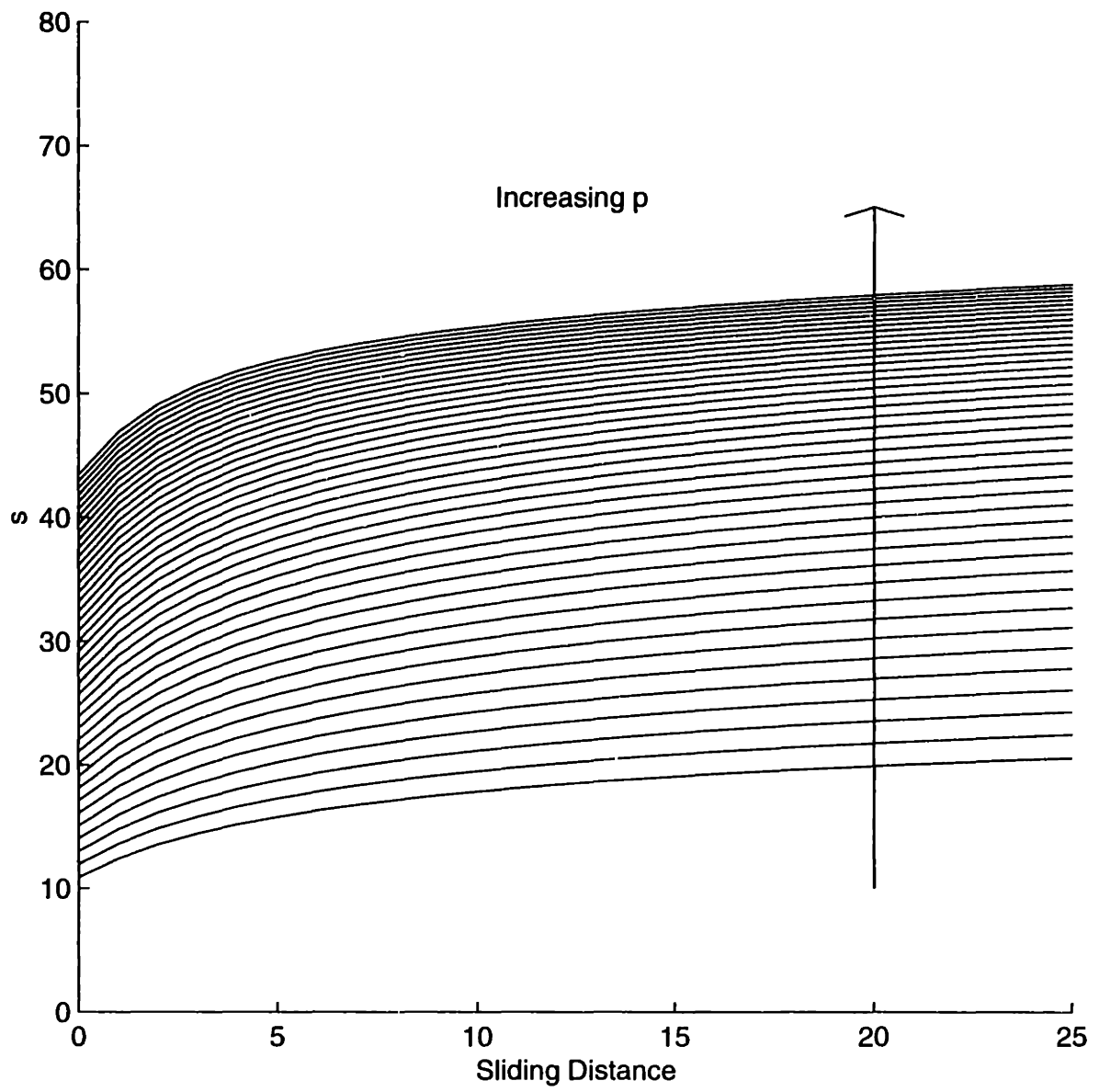
Figure D-1: Schematic of s vs. $\bar{u}^s$ at fixed values of p.
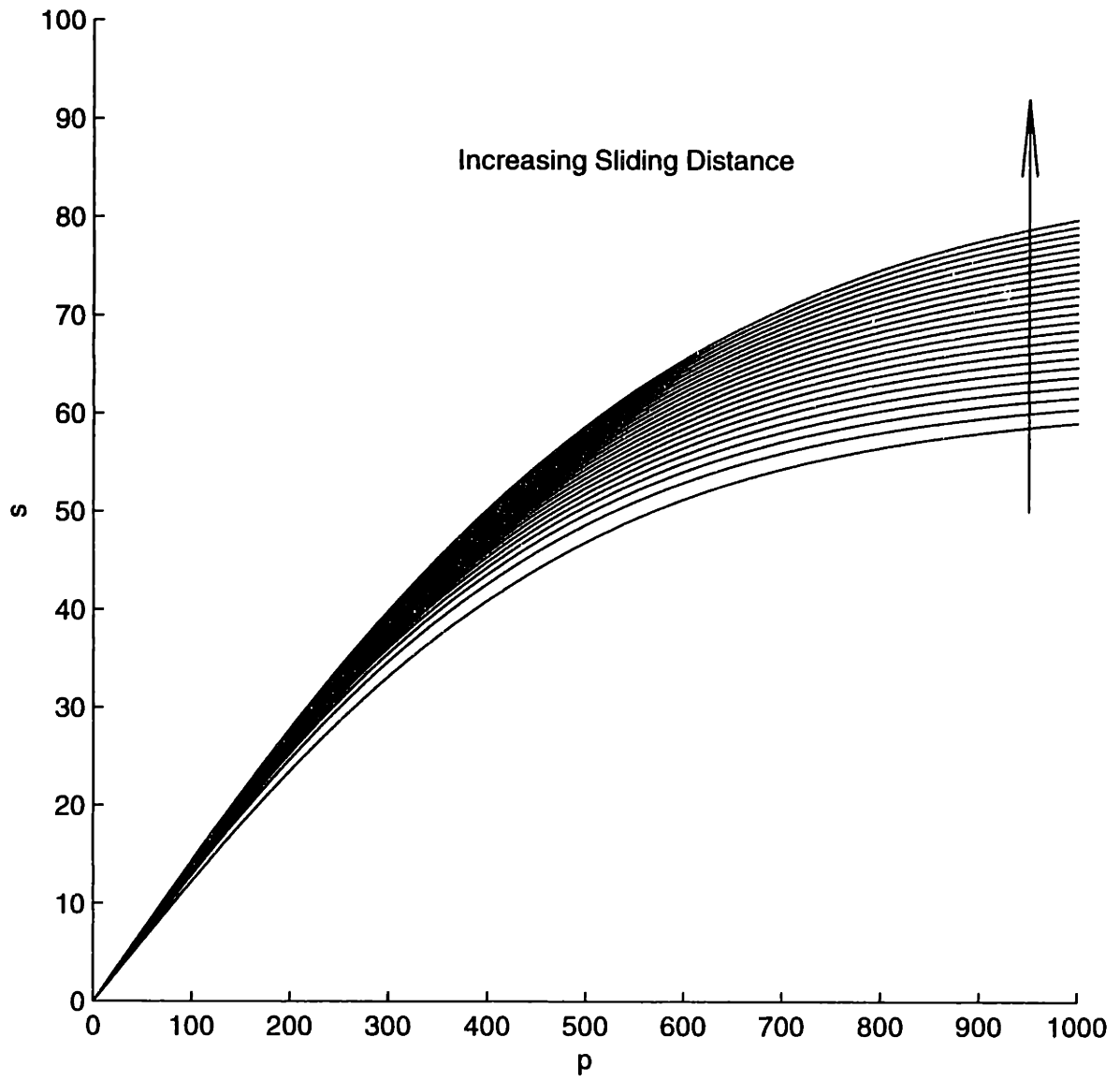
Figure D-2: Schematic of s vs. p at fixed values of $\bar{u}^s$
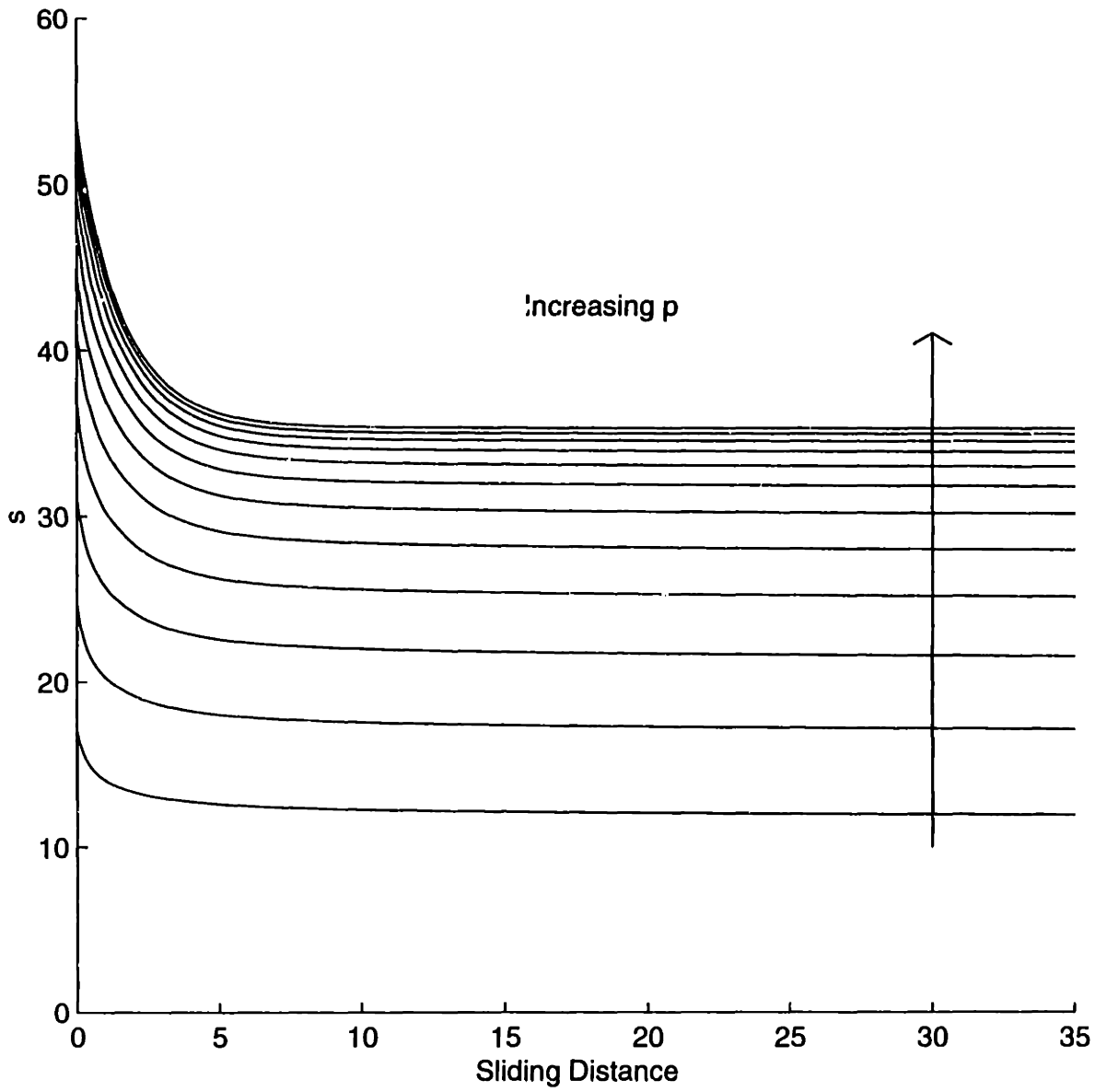
Figure D-3: Schematic of s vs. $\bar{u}^s$ at fixed values of p.
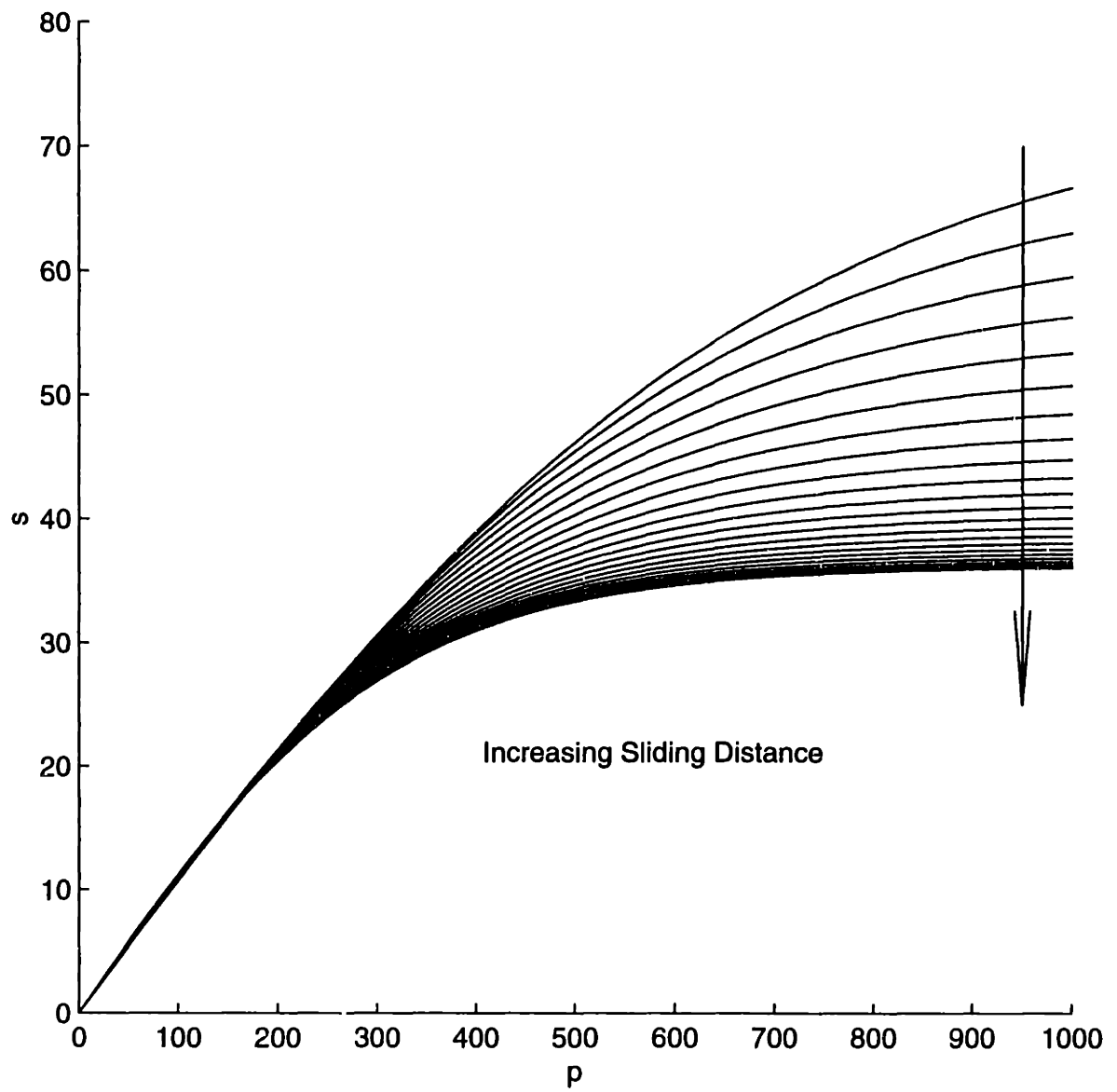
Figure D-4: Schematic of s vs. p at fixed values of $\bar{u}^s$

85
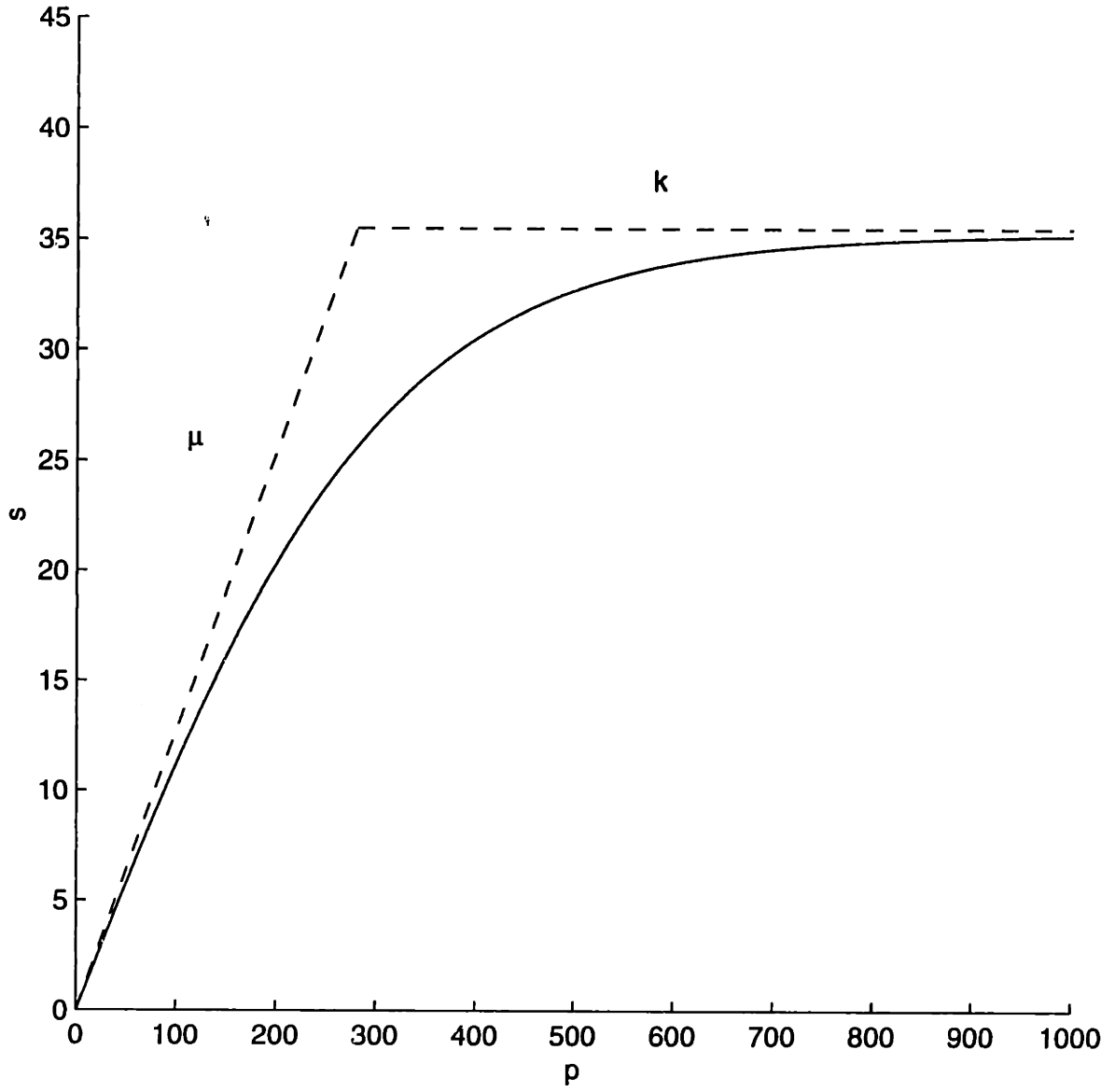
Figure D-5: Schematic of s vs. p at fixed values of $\overline{u}^s$ and the shear-cap model approximation.
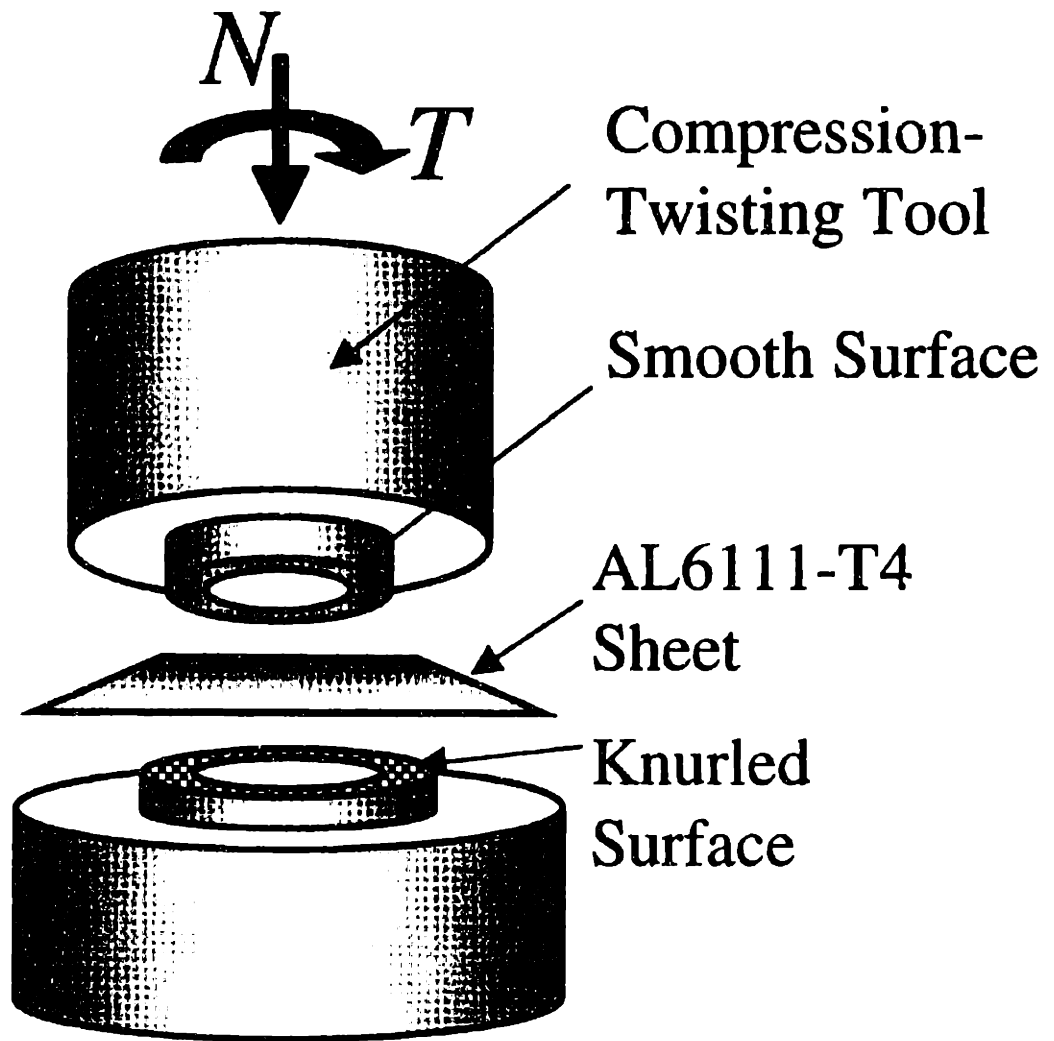
Figure D-6: Schematic of the experimental configuration for the friction test.
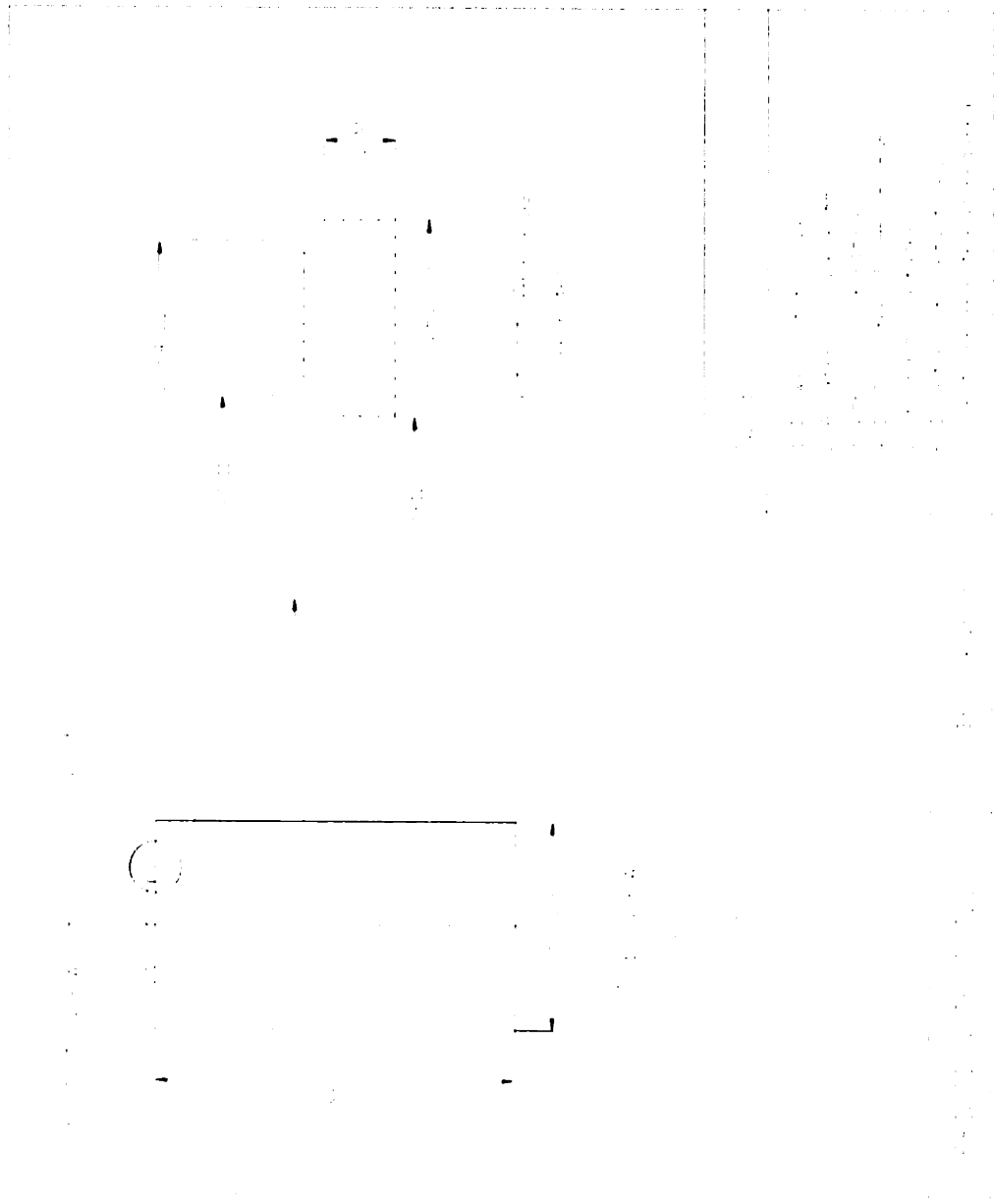
Figure D-7: Compression twisting tool.
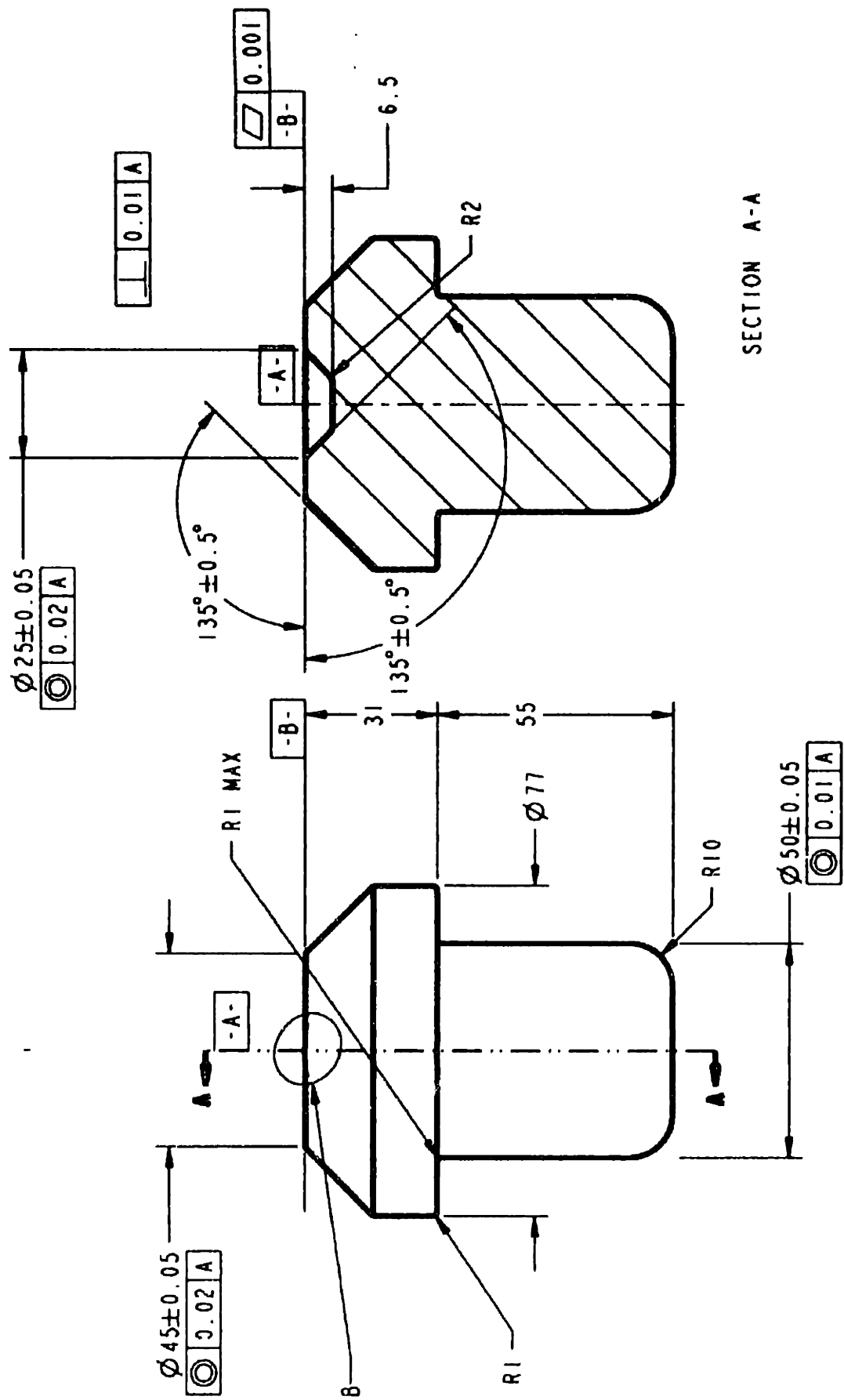
Figure D-8: Tool with knurled surface. All dimensions are in millimeters.

Figure D-9: Cross-section of knurled surface. Knurls have a 0.8 mm x 0.8 mm square base. All dimensions are in millimeters.
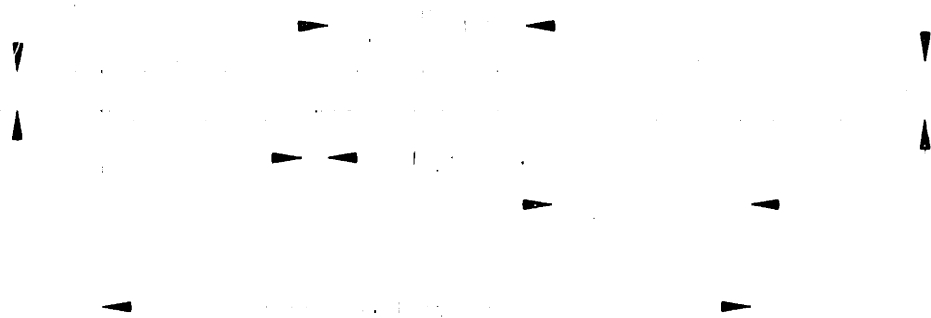
Figure D-10: Sheet tension specimen (ASTM E8). All dimensions are in inches.
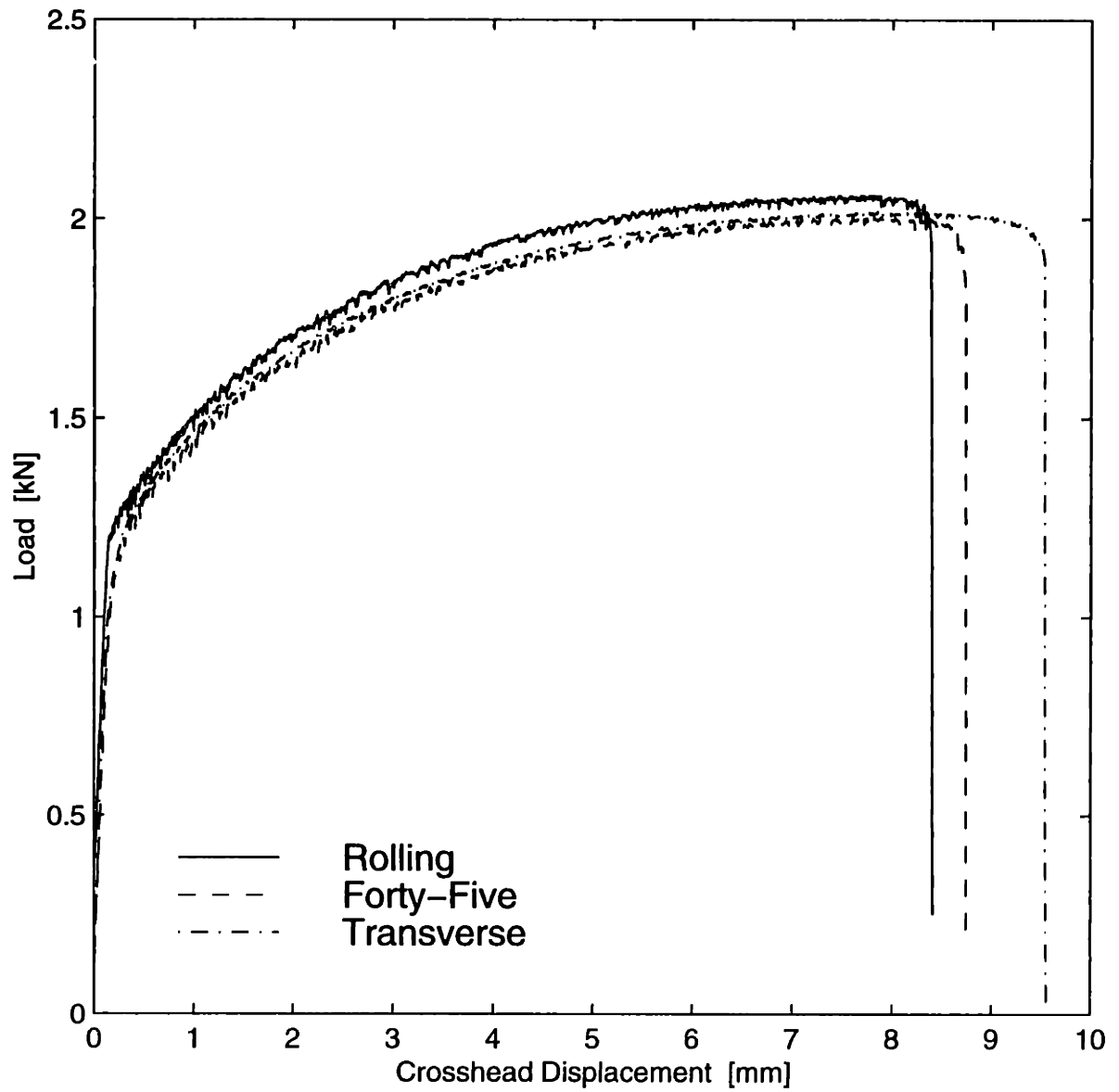
Figure D-11: Load vs. crosshead displacement for uniaxial tension of Al6111-T4 sheet specimens cut parallel, at forty-five degrees, and transverse to the rolling direction.
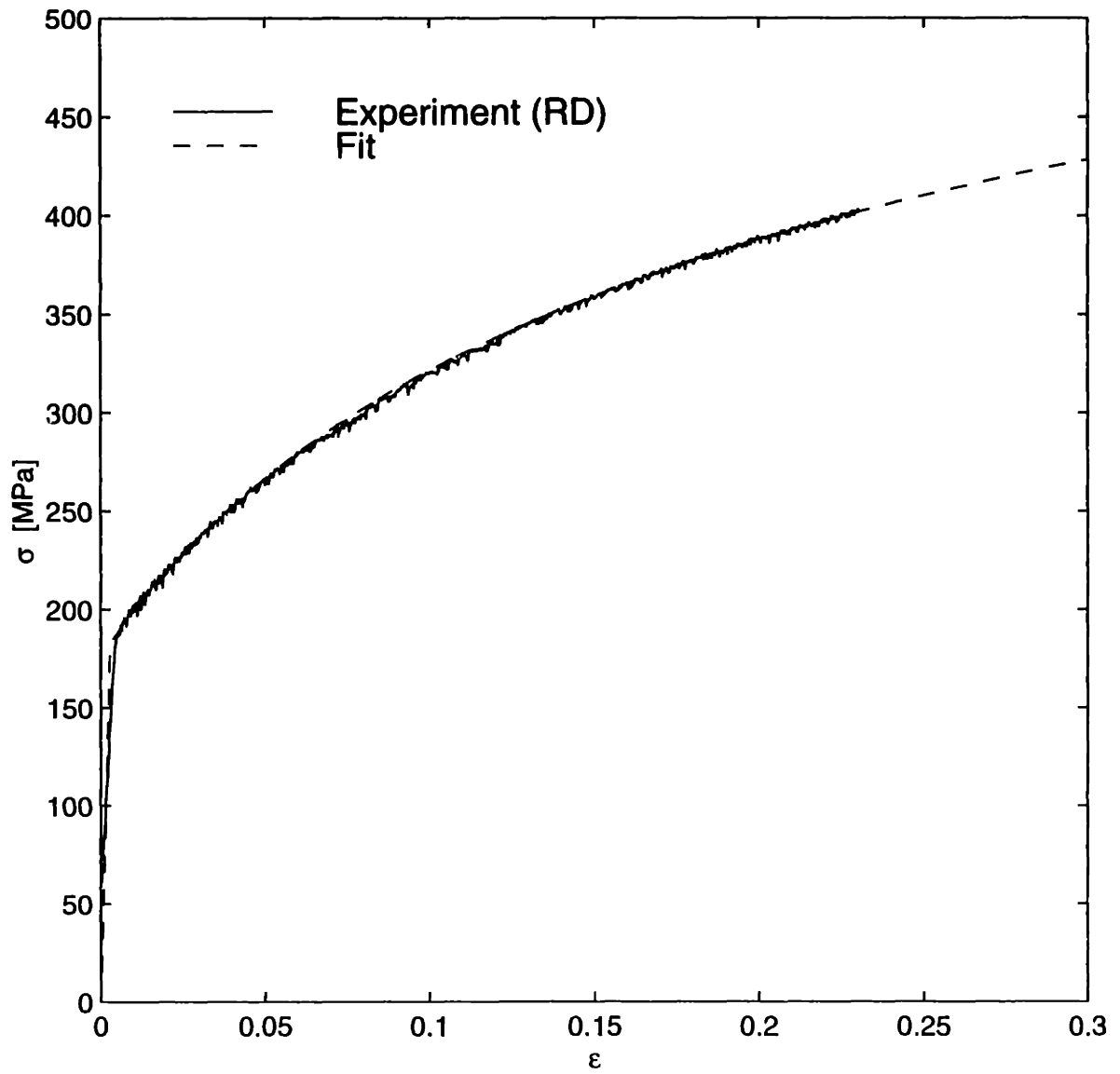
Figure D-12: Model fit of the true stress vs. true strain for uniaxial tension of Al6111-T4 specimen in the RD.
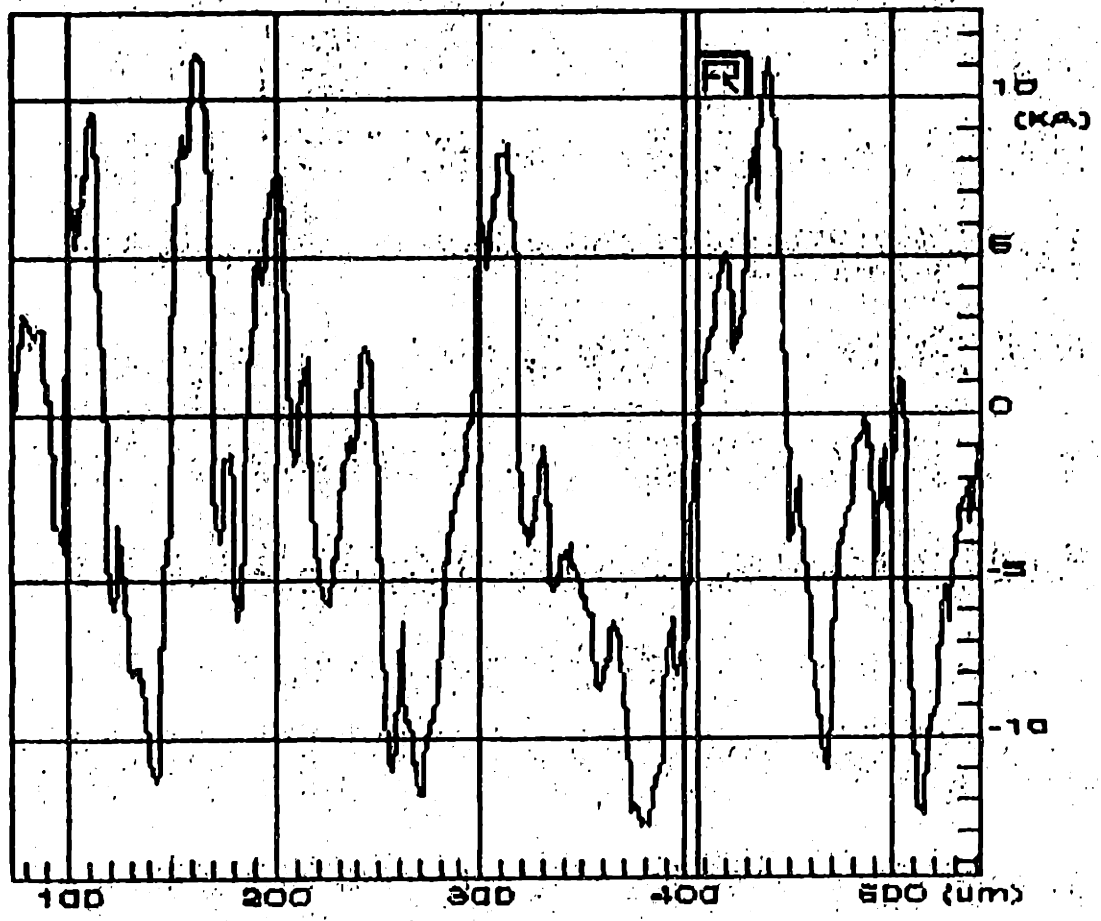
Figure D-13: Profile of Al6111-T4 as-received surface structure — perpendicular to rolling direction.
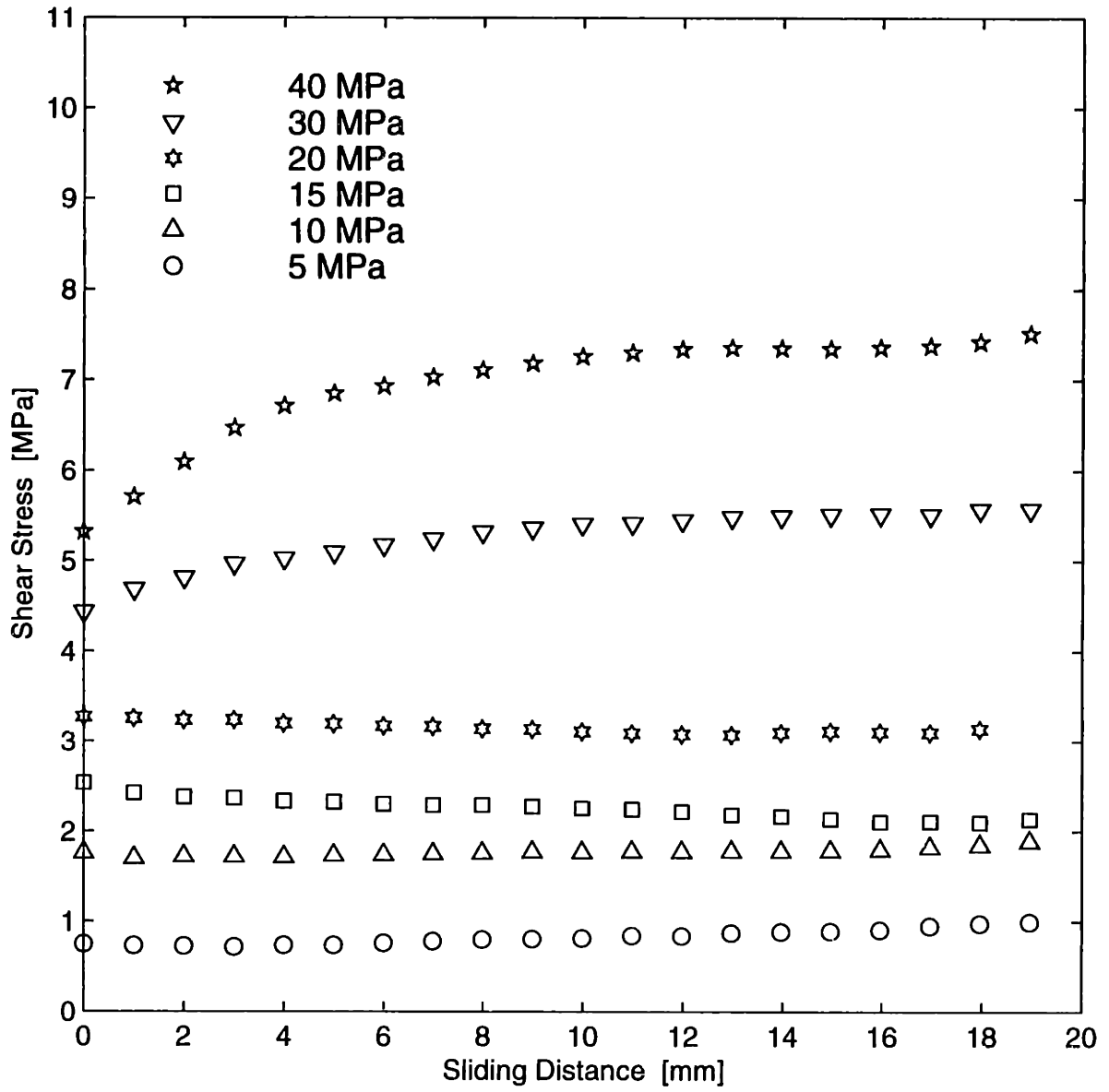
Figure D-14: Shear stress vs. sliding distance for the MP404 lubricated Al6111-T4 / tool steel interface for pressures from 5 MPa to 40 MPa with $\bar{v}^s = 1$ mm/s.
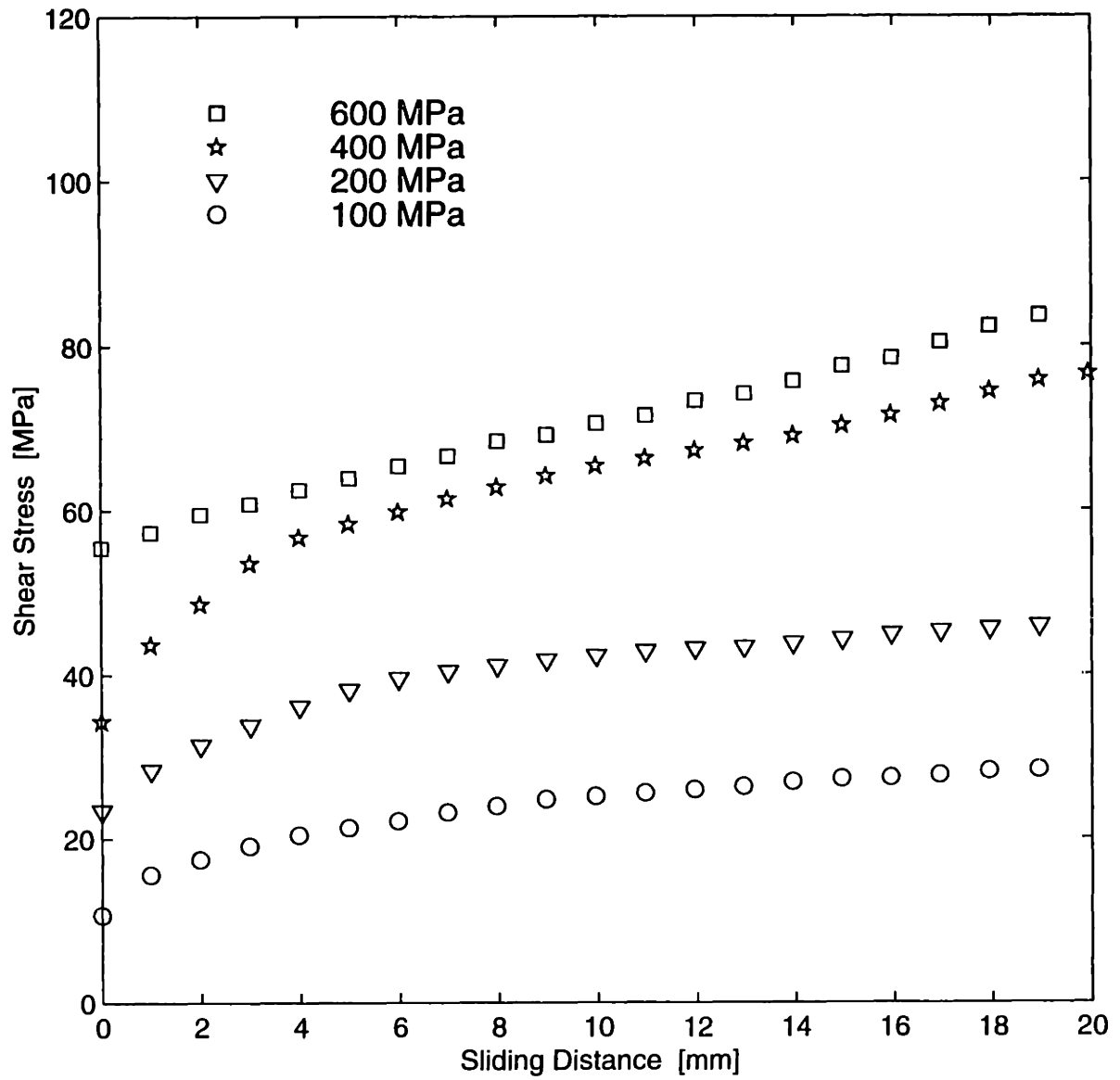
Figure D-15: Shear stress vs. sliding distance for the MP404 lubricated Al6111-T4 / tool steel interface for pressures from 100 MPa to 600 MPa with $\bar{v}^s = 1$ mm/s.
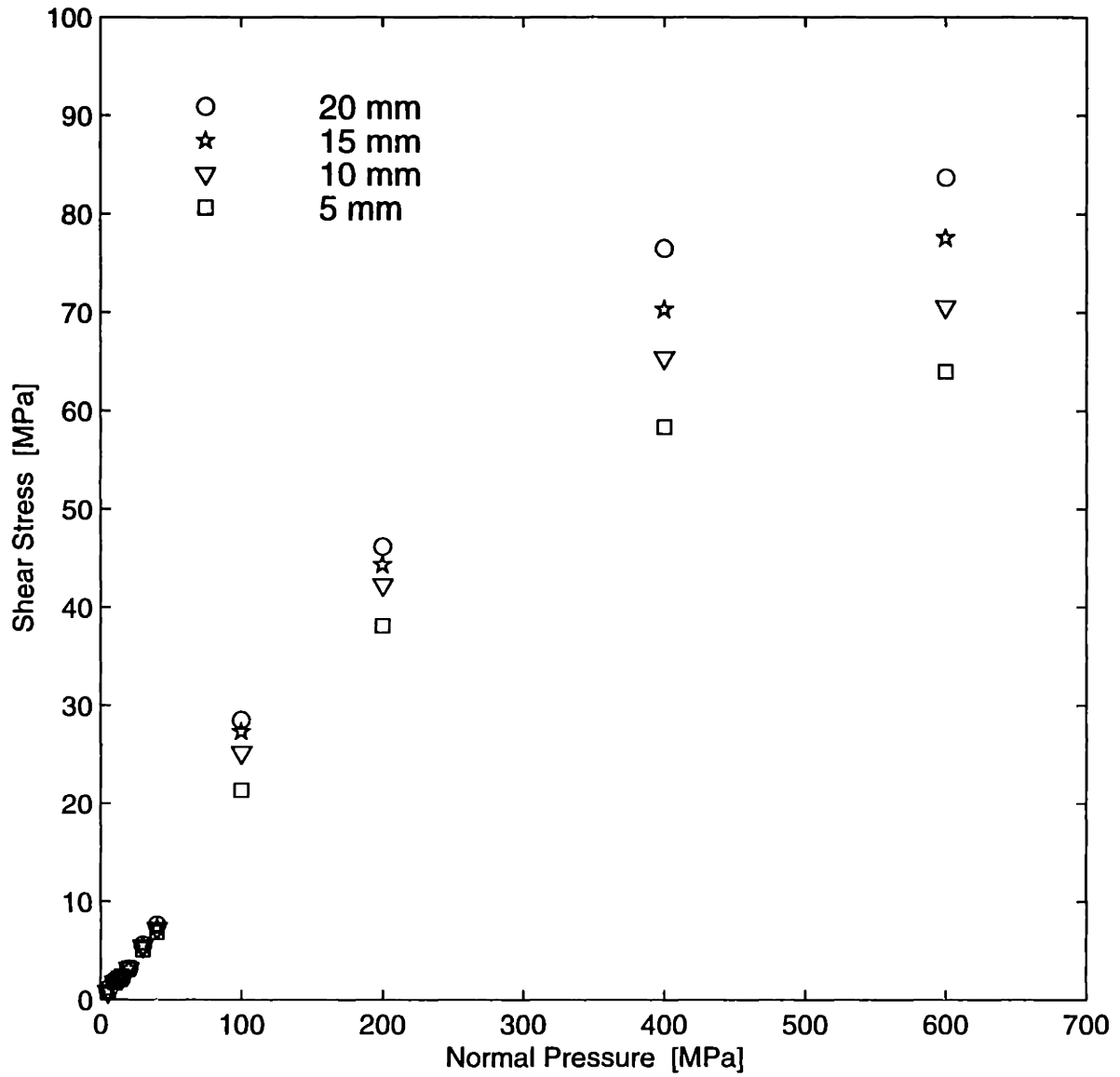
Figure D-16: Shear stress vs. normal pressure for the MP404 lubricated Al6111-T4 / tool steel interface at fixed sliding distances with $\bar{v}^s = 1$ mm/s.
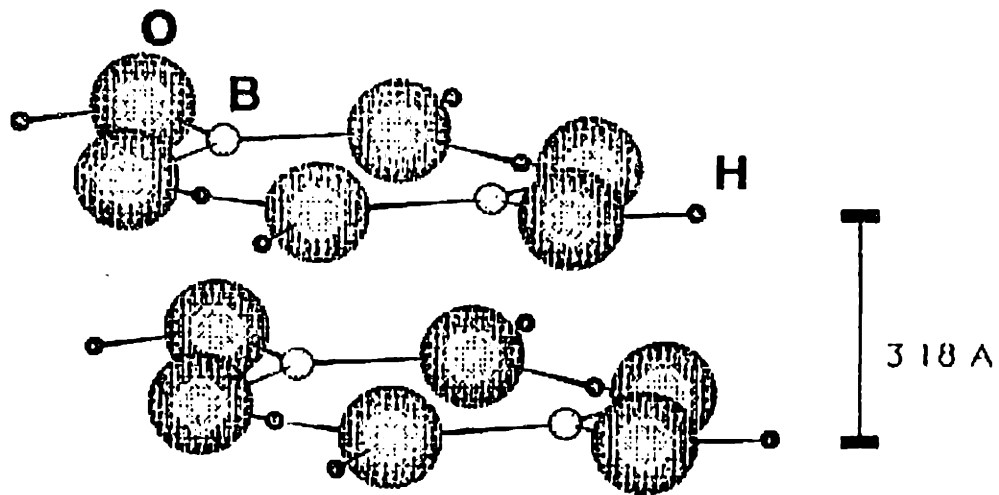
Figure D-17: Schematic of an interatomic array of boric acid showing its layered crystal structure (adapted from [13]).
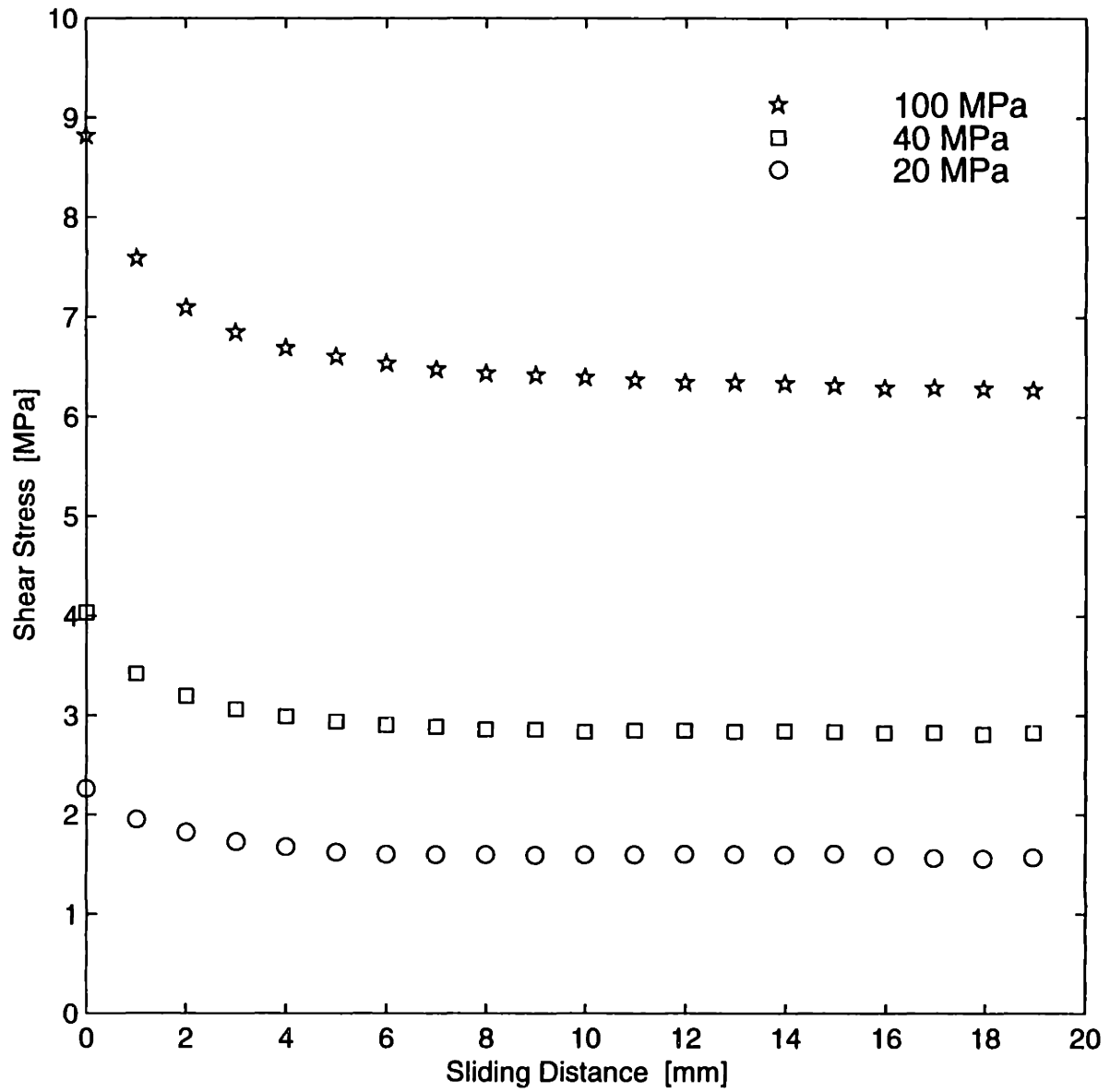
Figure D-18: Shear stress vs. sliding distance for the boric acid lubricated Al6111-T4 / tool steel interface for pressures from 20 MPa to 100 MPa with $\overline{v}^s = 1$ mm/s.
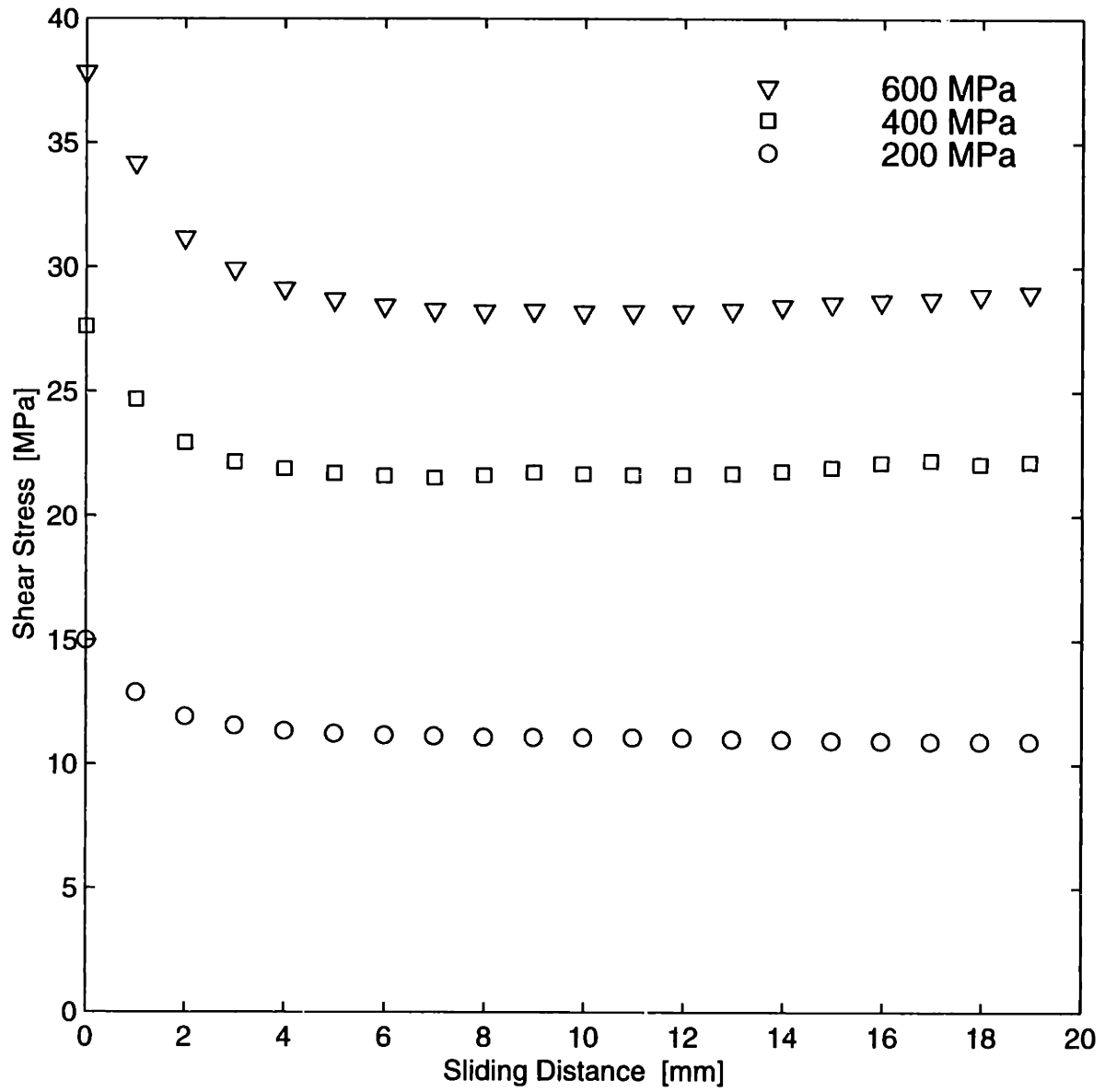
Figure D-19: Shear stress vs. sliding distance for the boric acid lubricated Al6111-T4 / tool steel interface for pressures from 200 MPa to 600 MPa with $\bar{v}^s = 1$ mm/s.
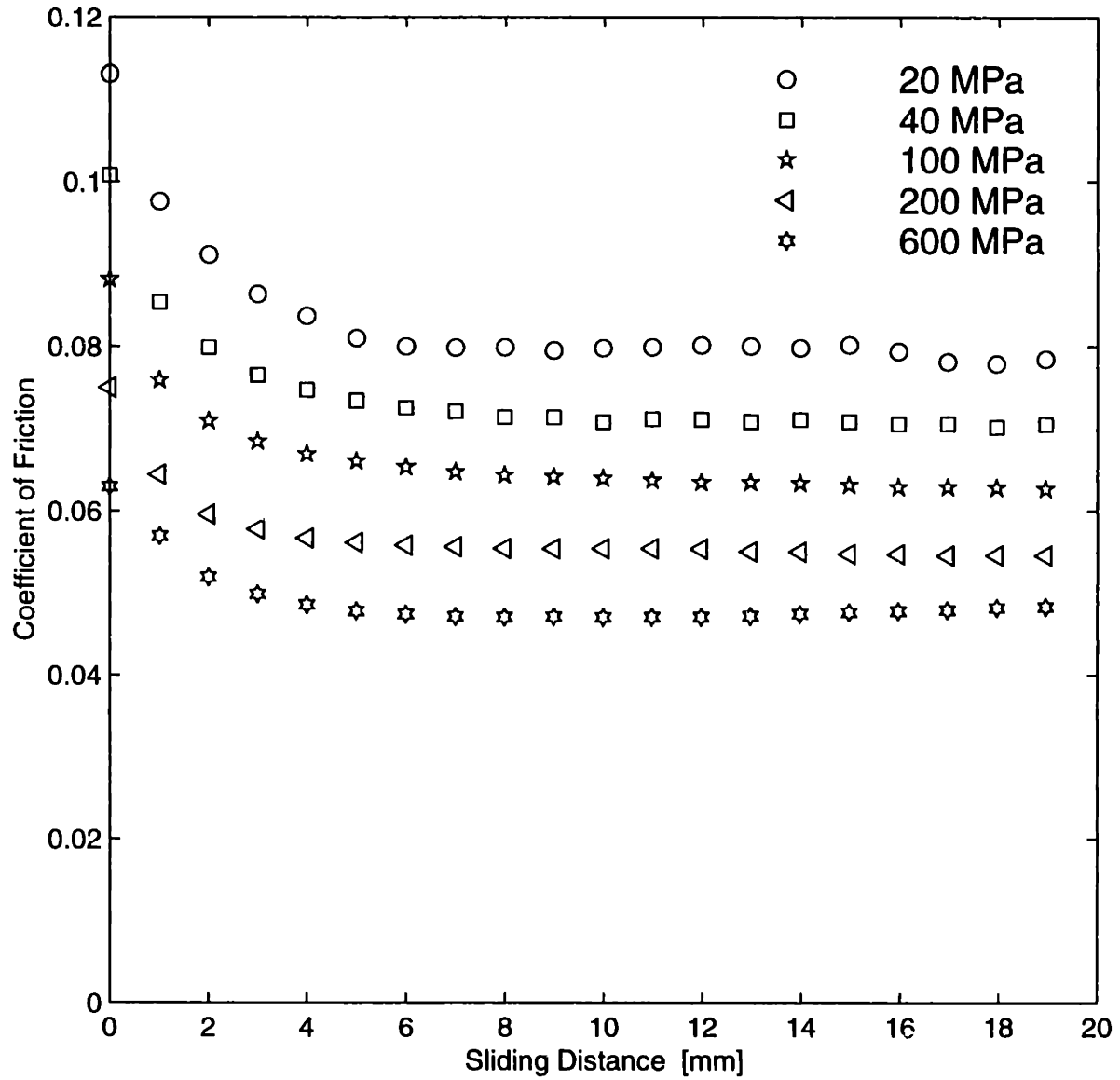
Figure D-20: Coefficient of Friction vs. sliding distance for the boric acid lubricated Al6111-T4 / tool steel interface at $\overline{v}^s = 1$ mm/s.
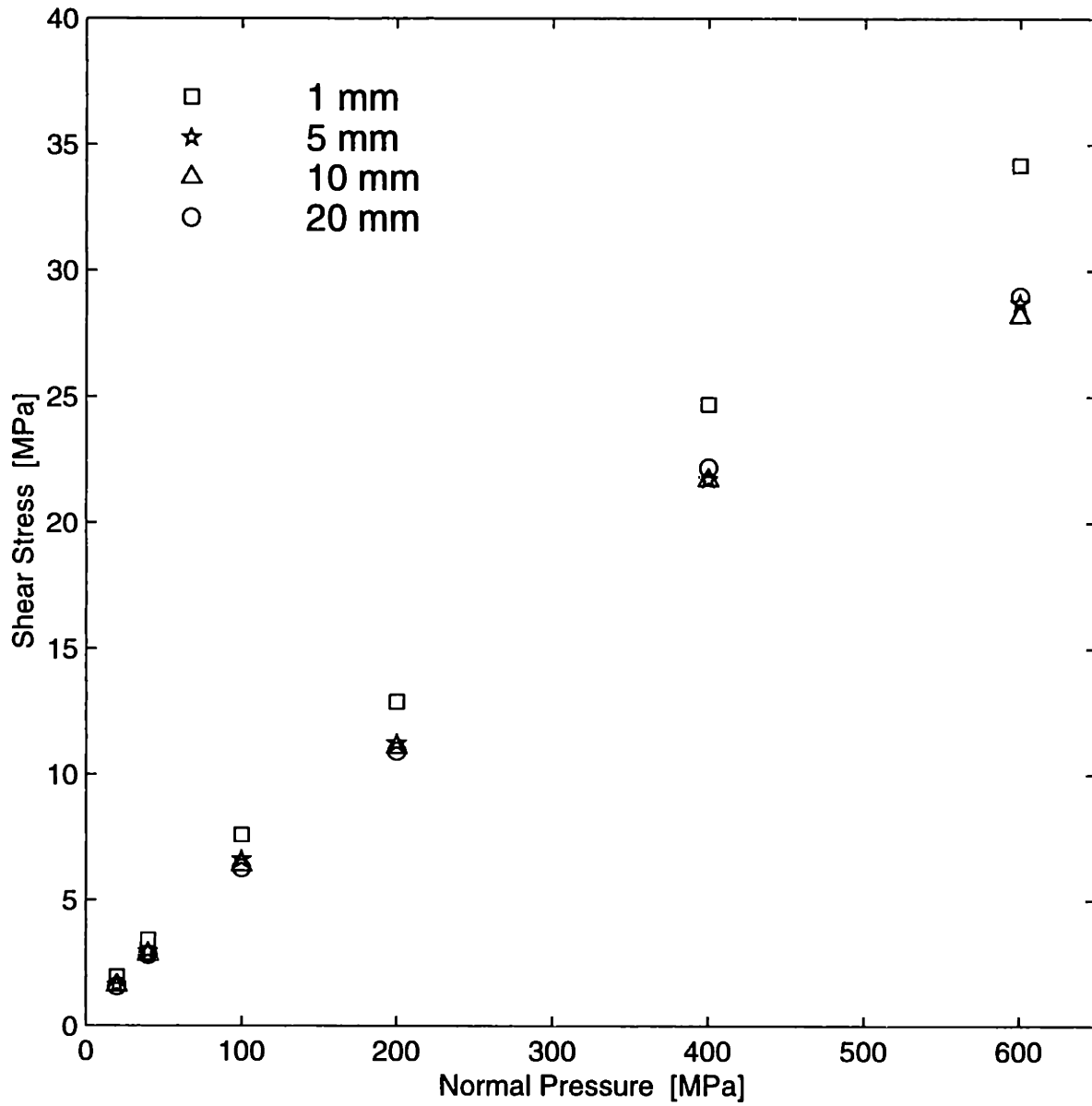
Figure D-21: Shear stress vs. normal pressure for the boric acid lubricated Al6111-T4 / tool steel interface at fixed sliding distances with $\bar{v}^s = 1$ mm/s.
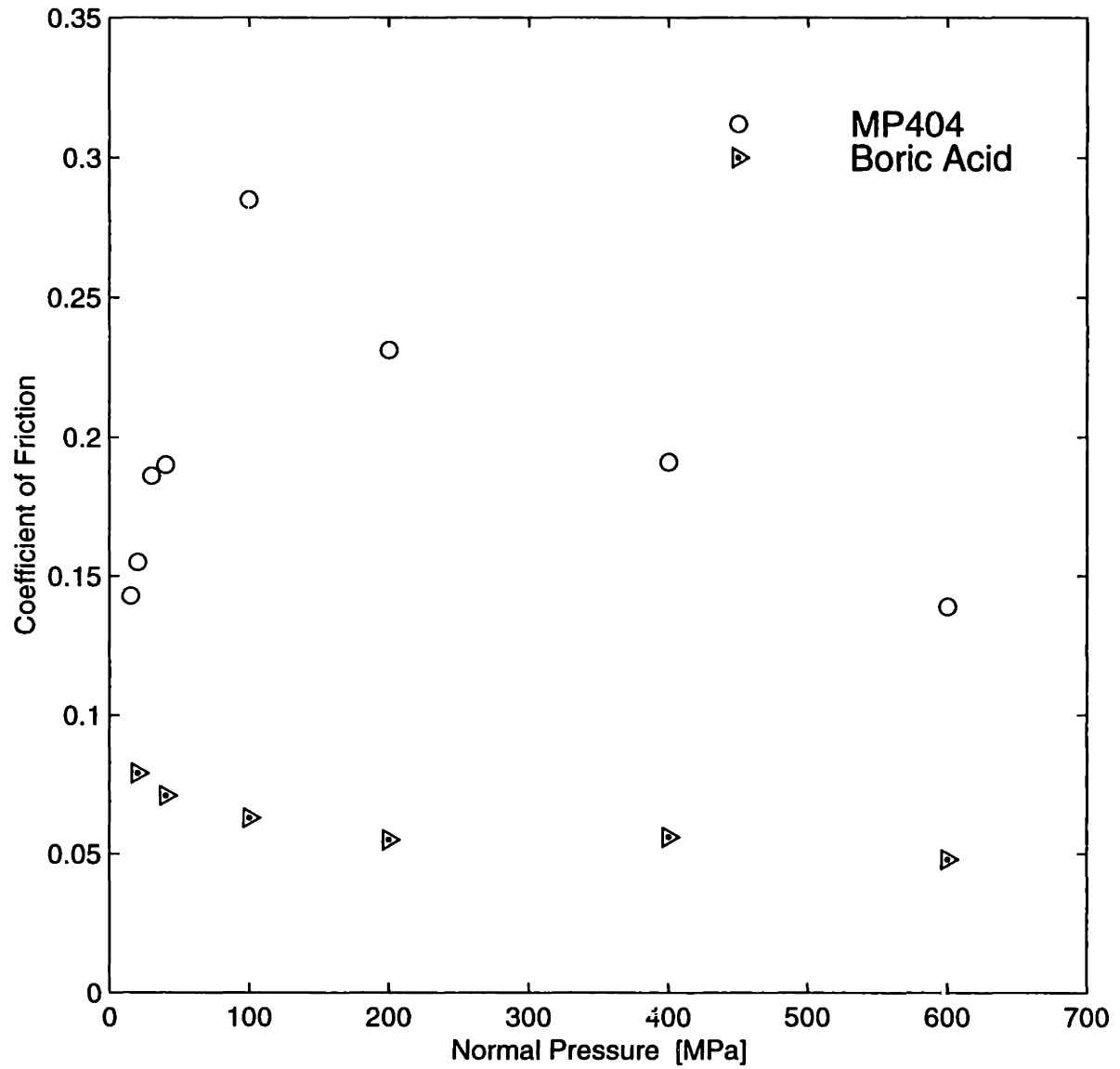
Figure D-22: Coefficient of friction vs. normal pressure for the MP404 and boric acid lubricated Al6111-T4 / tool steel interfaces at a sliding distance of 20 mm with $\bar{v}^s = 1$ mm/s.
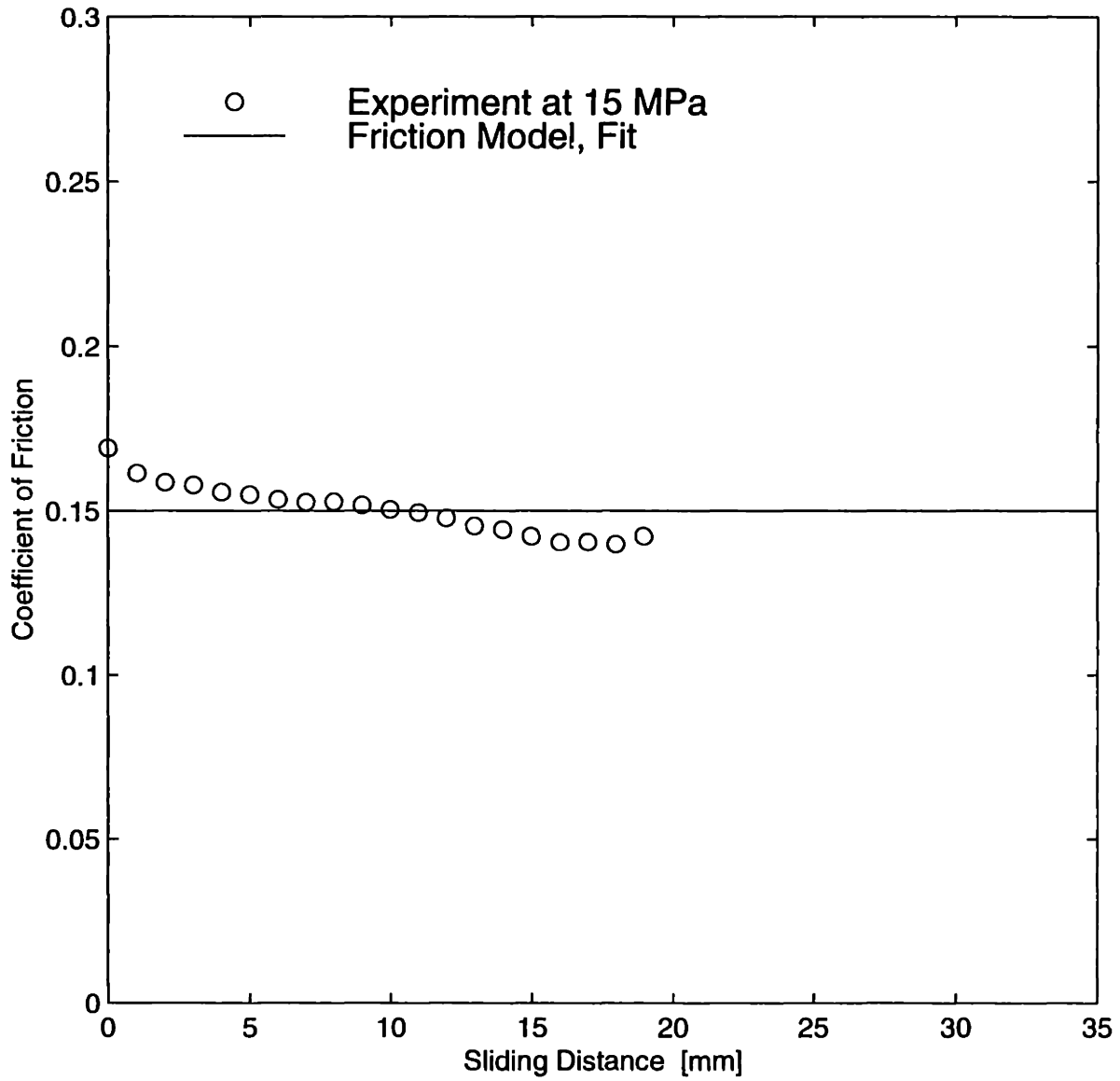
Figure D-23: Friction model fit of the coefficient of friction vs. sliding distance for the MP404 lubricated Al6111-T4 / tool steel interface at $p = 15$ MPa and $\bar{v}^s = 1$ mm/s.
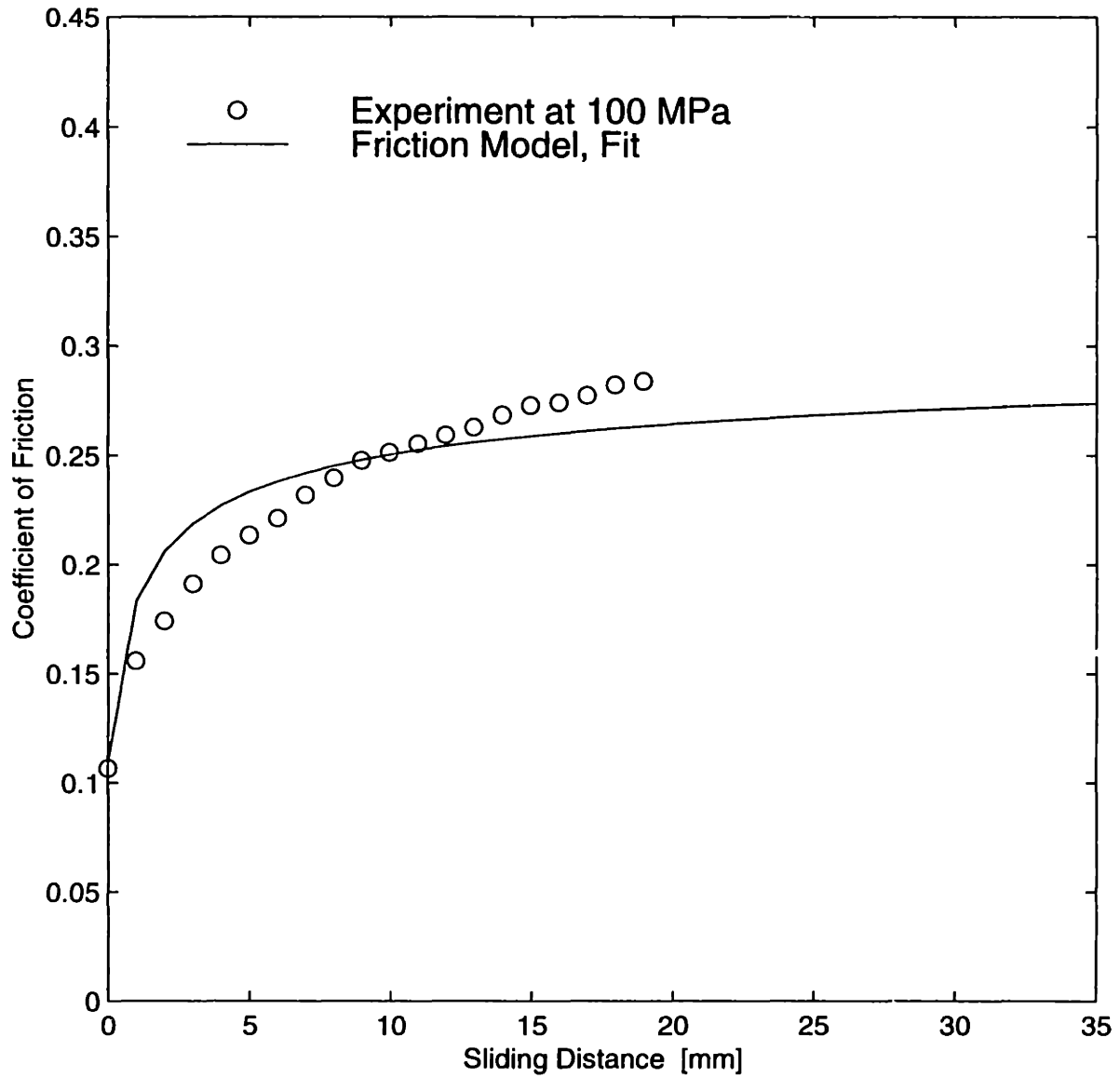
Figure D-24: Friction model fit of the coefficient of friction vs. sliding distance for the MP404 lubricated Al6111-T4 / tool steel interface at $p = 100$ MPa and $\bar{v}^s = 1$ mm/s.
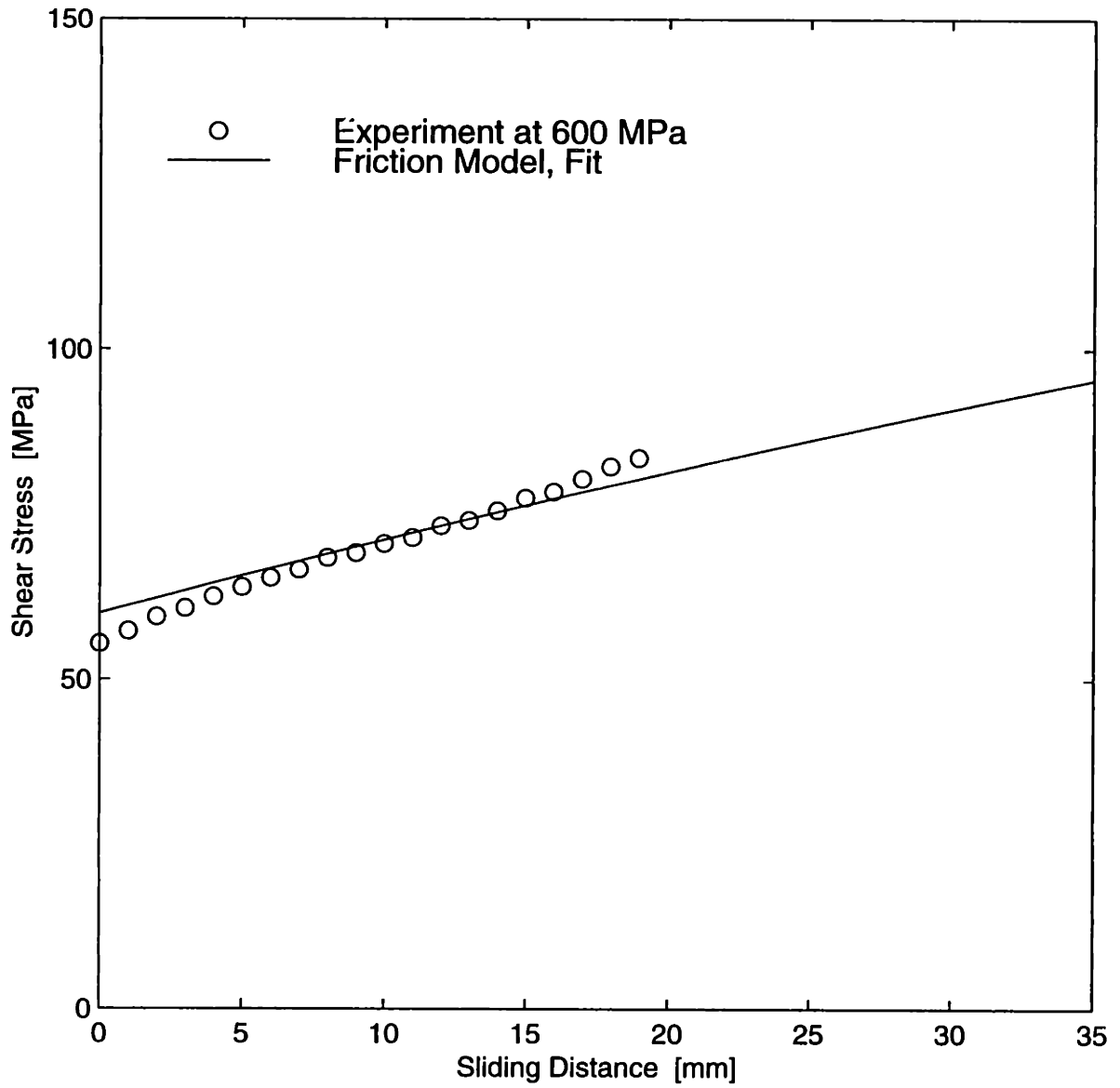
Figure D-25: Friction model fit of the shear stress vs. sliding distance for the MP404 lubricated Al6111-T4 / tool steel interface at $p = 600$ MPa and $\bar{v}^s = 1$ mm/s.
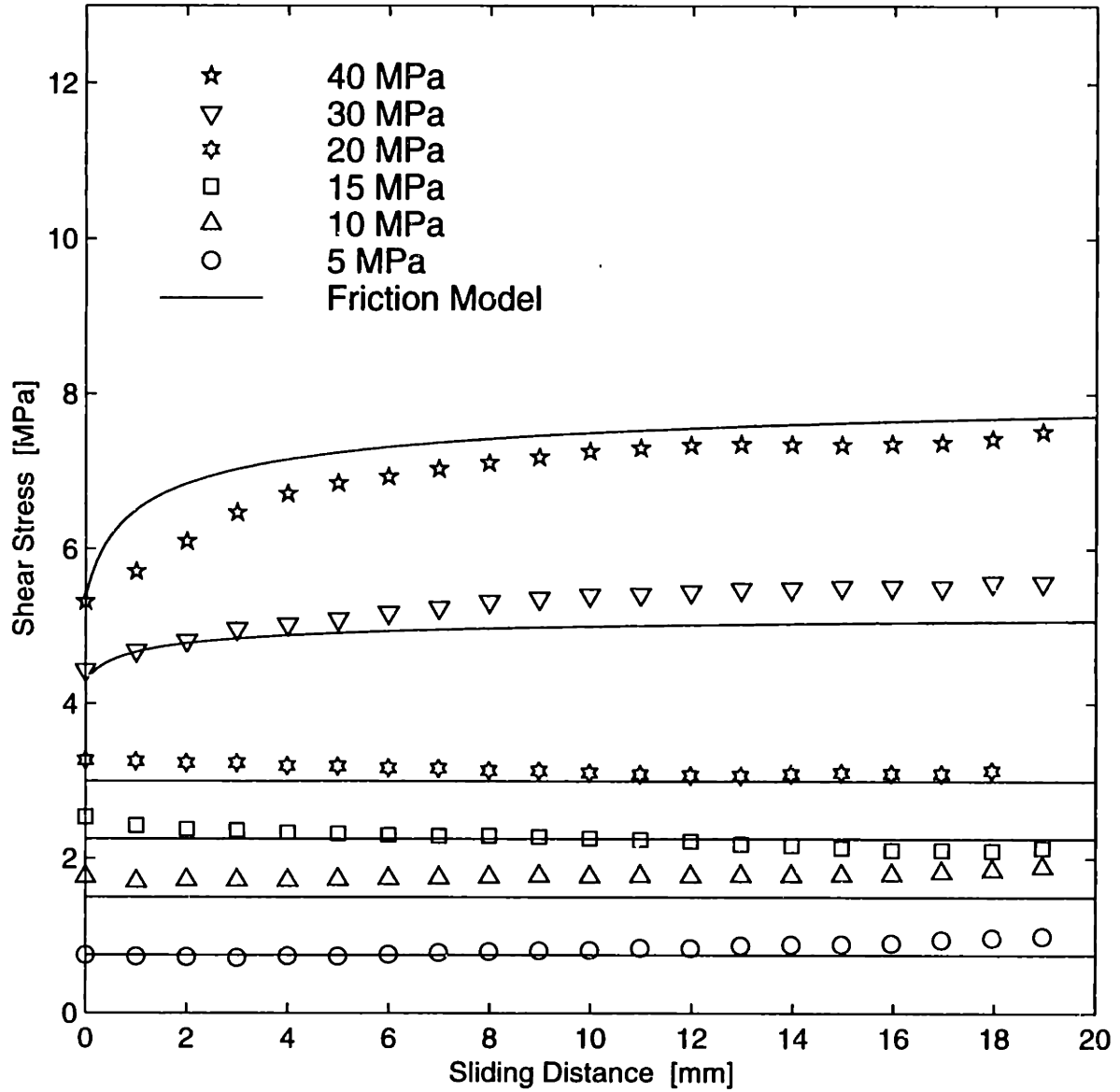
Figure D-26: Friction model fit of the shear stress vs. sliding distance for the MP404 lubricated Al6111-T4 / tool steel interface at low normal pressures.
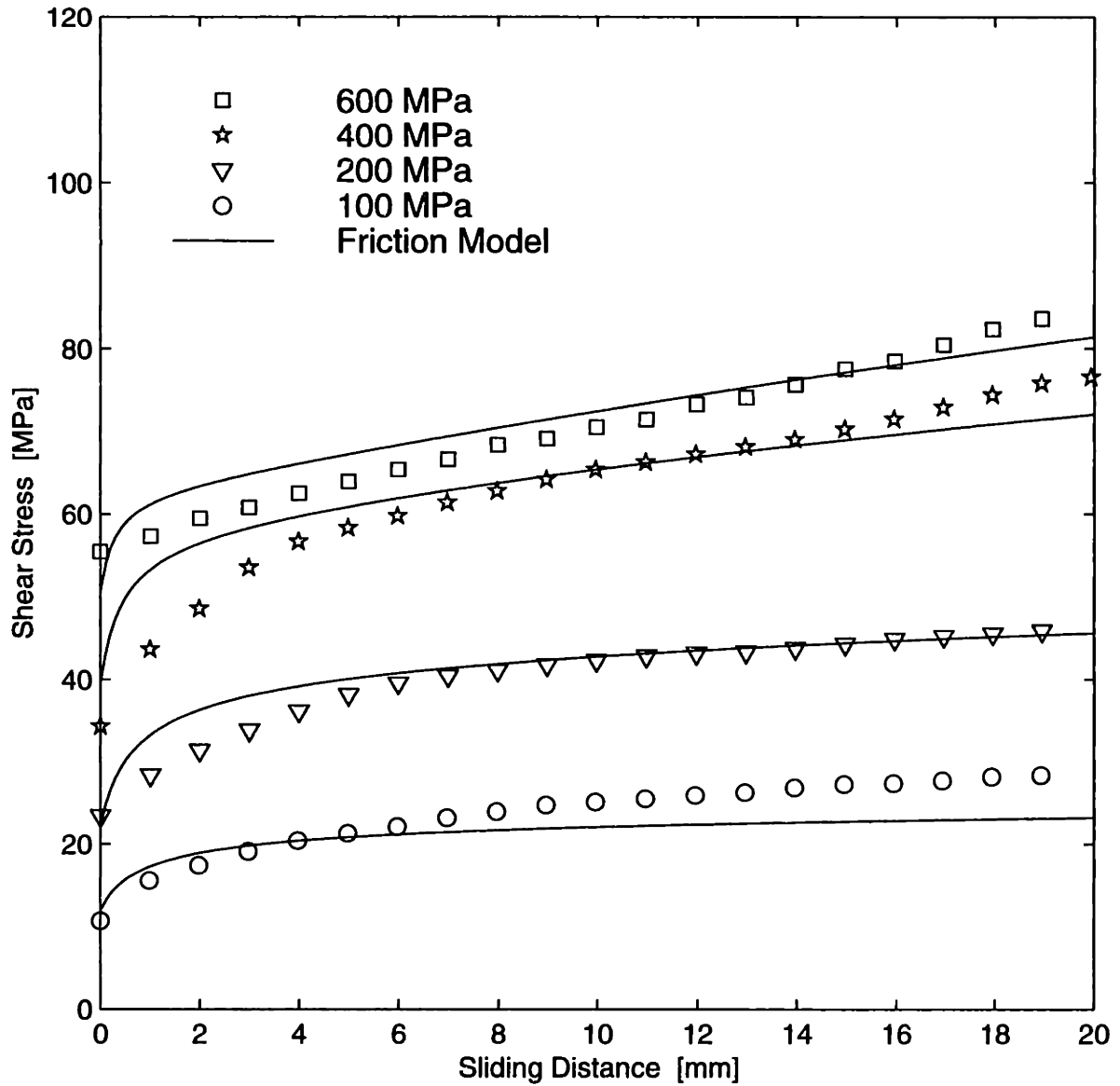
Figure D-27: Friction model fit of the shear stress vs. sliding distance for the MP404 lubricated Al6111-T4 / tool steel interface at high normal pressures.
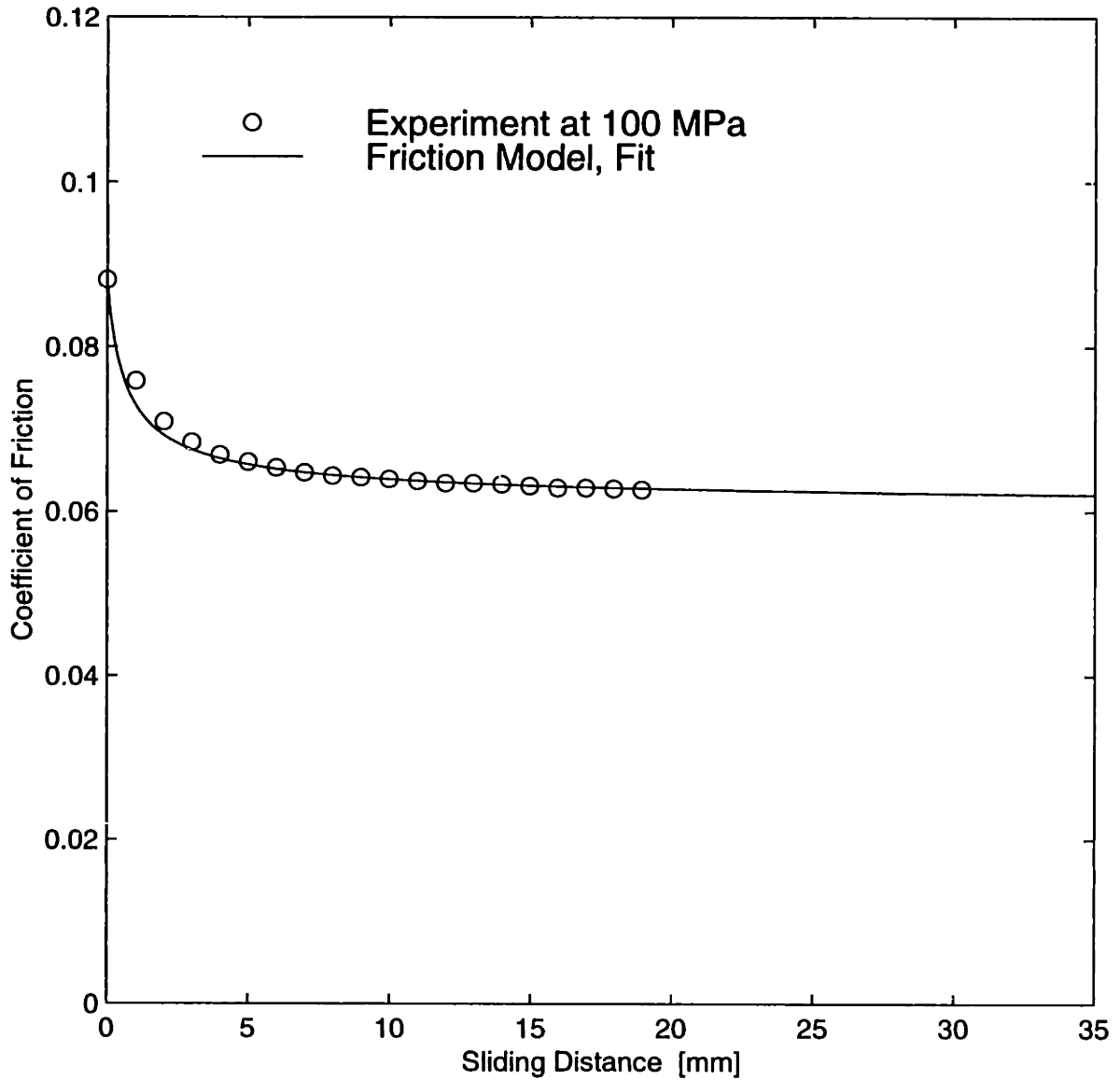
Figure D-28: Friction model fit of the coefficient of friction vs. sliding distance for the boric acid lubricated Al6111-T4 / tool steel interface at p = 100 MPa and $\bar{v}^s = 1$ mm/s.
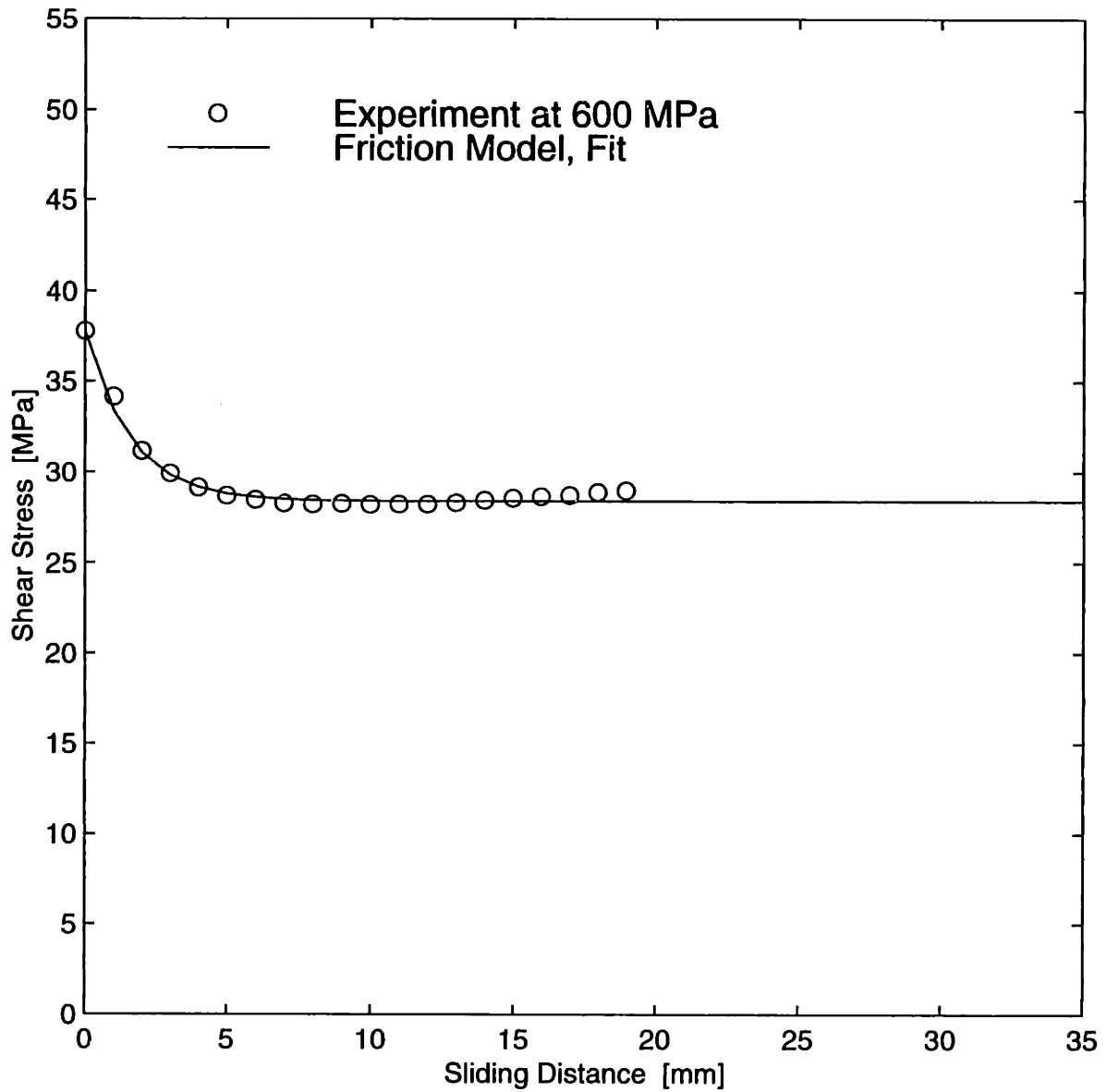
Figure D-29: Friction model fit of the shear stress vs. sliding distance for the boric acid lubricated Al6111-T4 / tool steel interface at p = 600 MPa and $\bar{v}^s = 1$ mm/s.
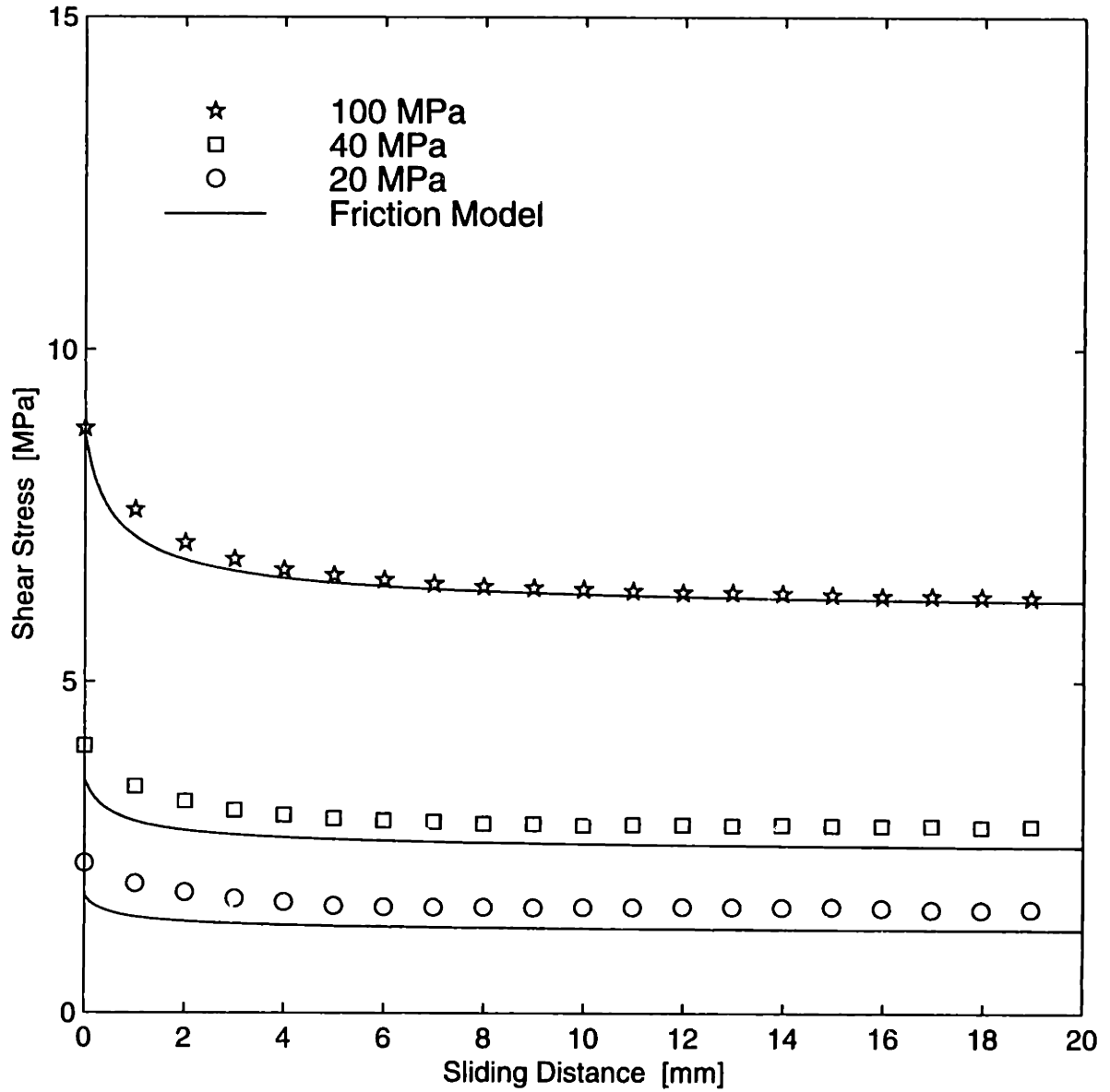
Figure D-30: Friction model fit of the shear stress vs. sliding distance for the boric acid lubricated Al6111-T4 / tool steel interface at low normal pressures.
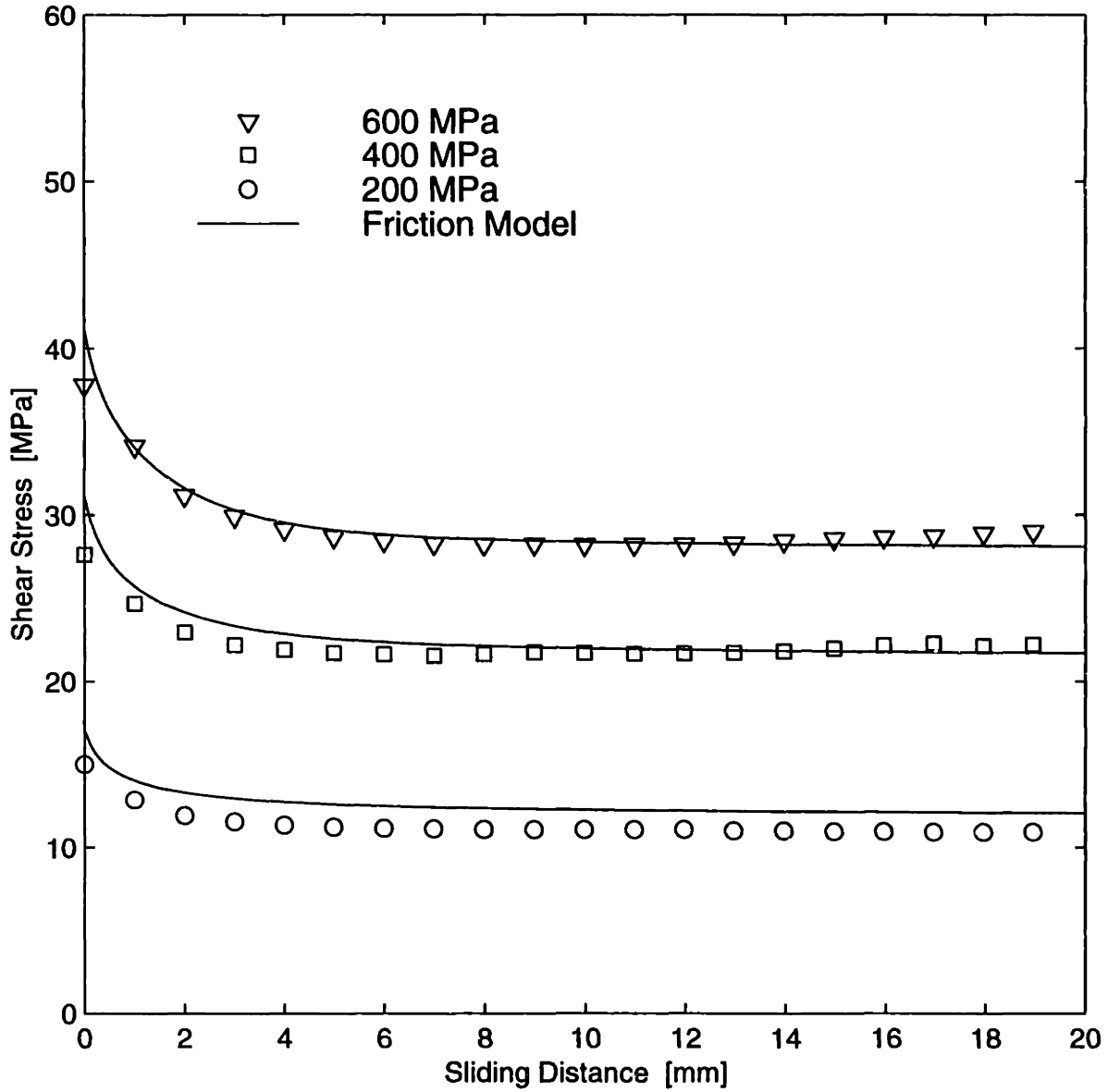
Figure D-31: Friction model fit of the shear stress vs. sliding distance for the boric acid lubricated Al6111-T4 / tool steel interface at high normal pressures.
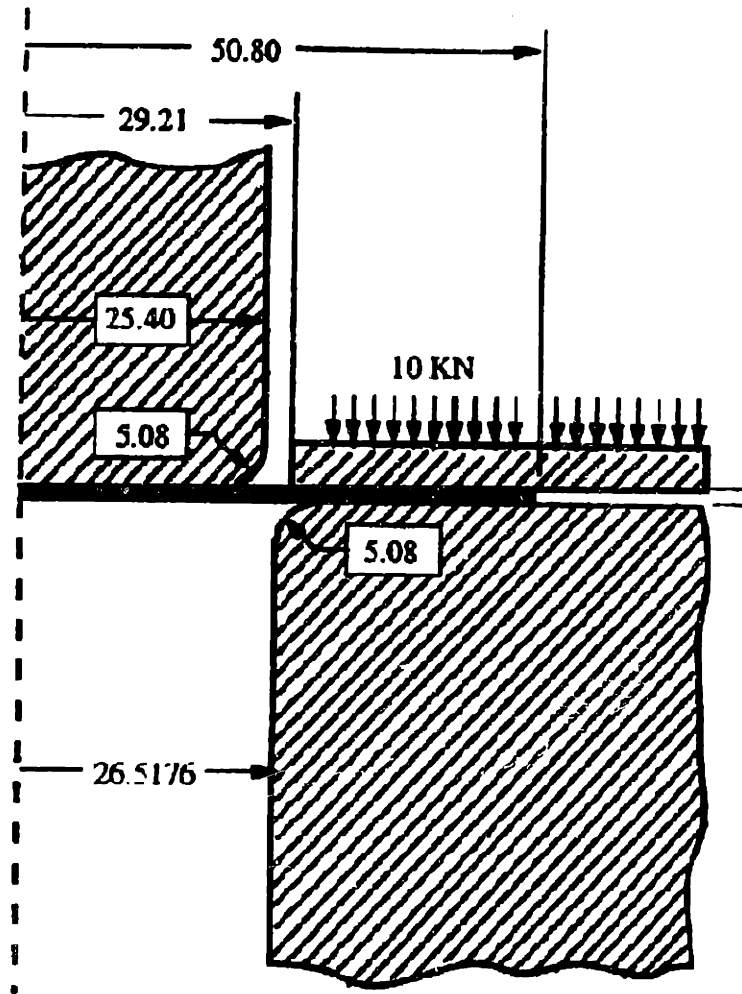
Figure D-32: Geometry of the axisymmetric cup-drawing apparatus with dimensions in mm (adapted from [16]).

Figure D-33: Fully drawn axisymmetric cup of Al6111-T4 using MP404 lubricant.
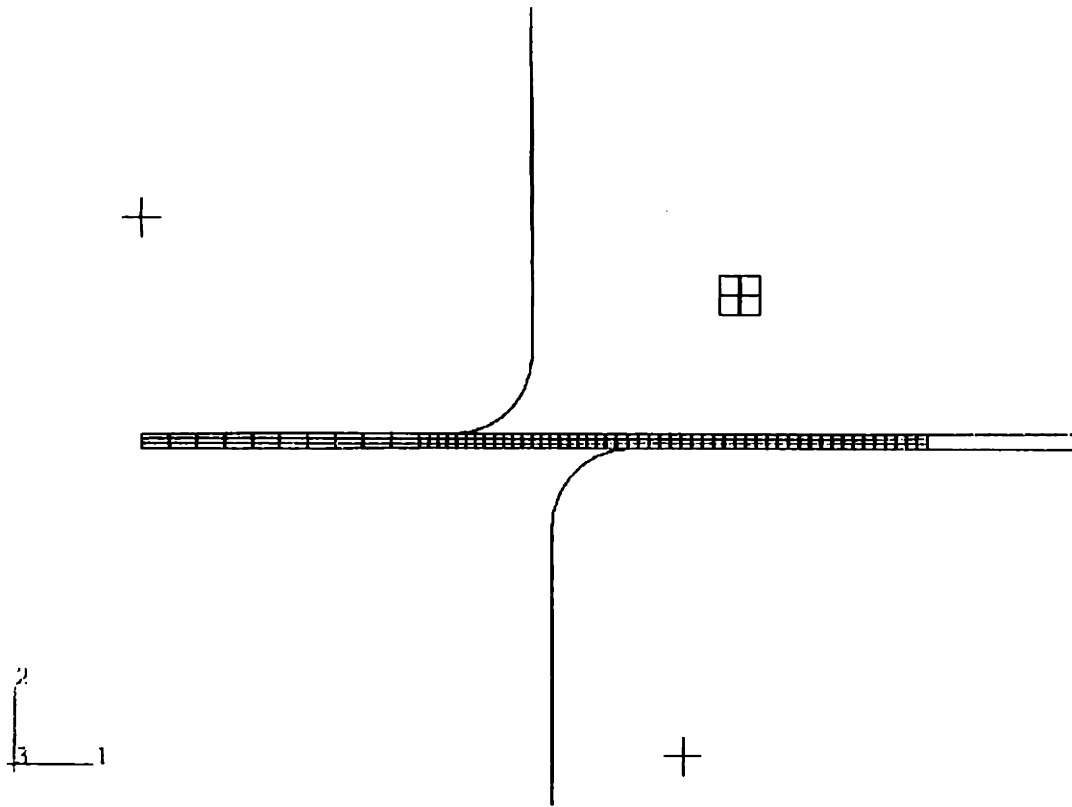
Figure D-34: Axisymmetric mesh for the simulation of the deep drawing of an Al6111-T4 blank with MP404 lubricant. Punch and die are indicated by +, with the die and binder on the right.
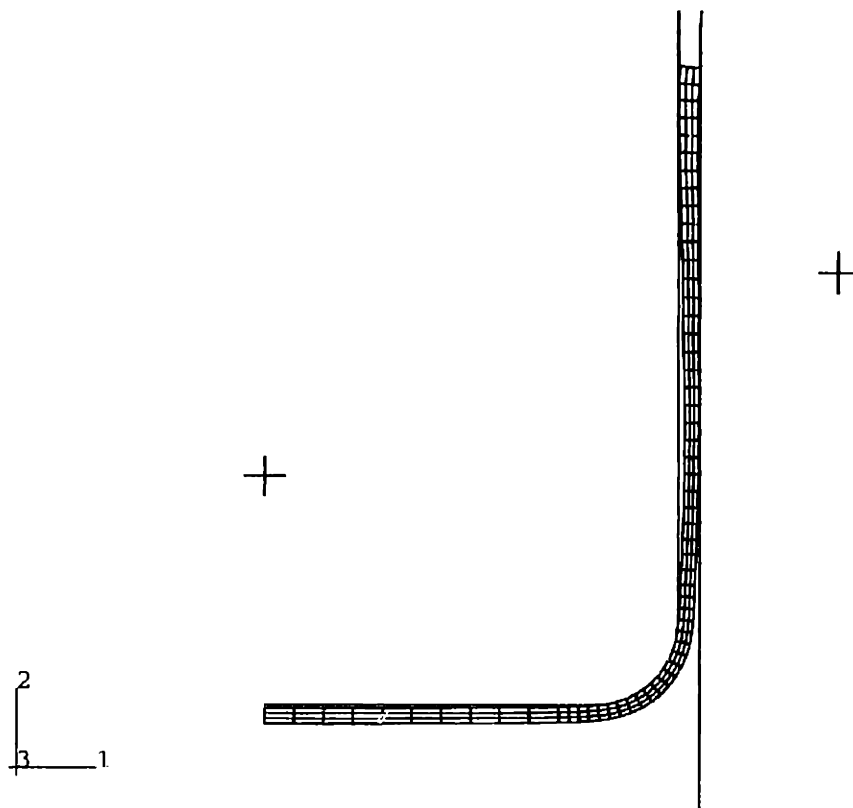
Figure D-35: Deformed mesh for the simulation of deep drawing of an Al6111-T4 blank with MP404 lubricant. Punch and die are indicated by +, with the die on the right.
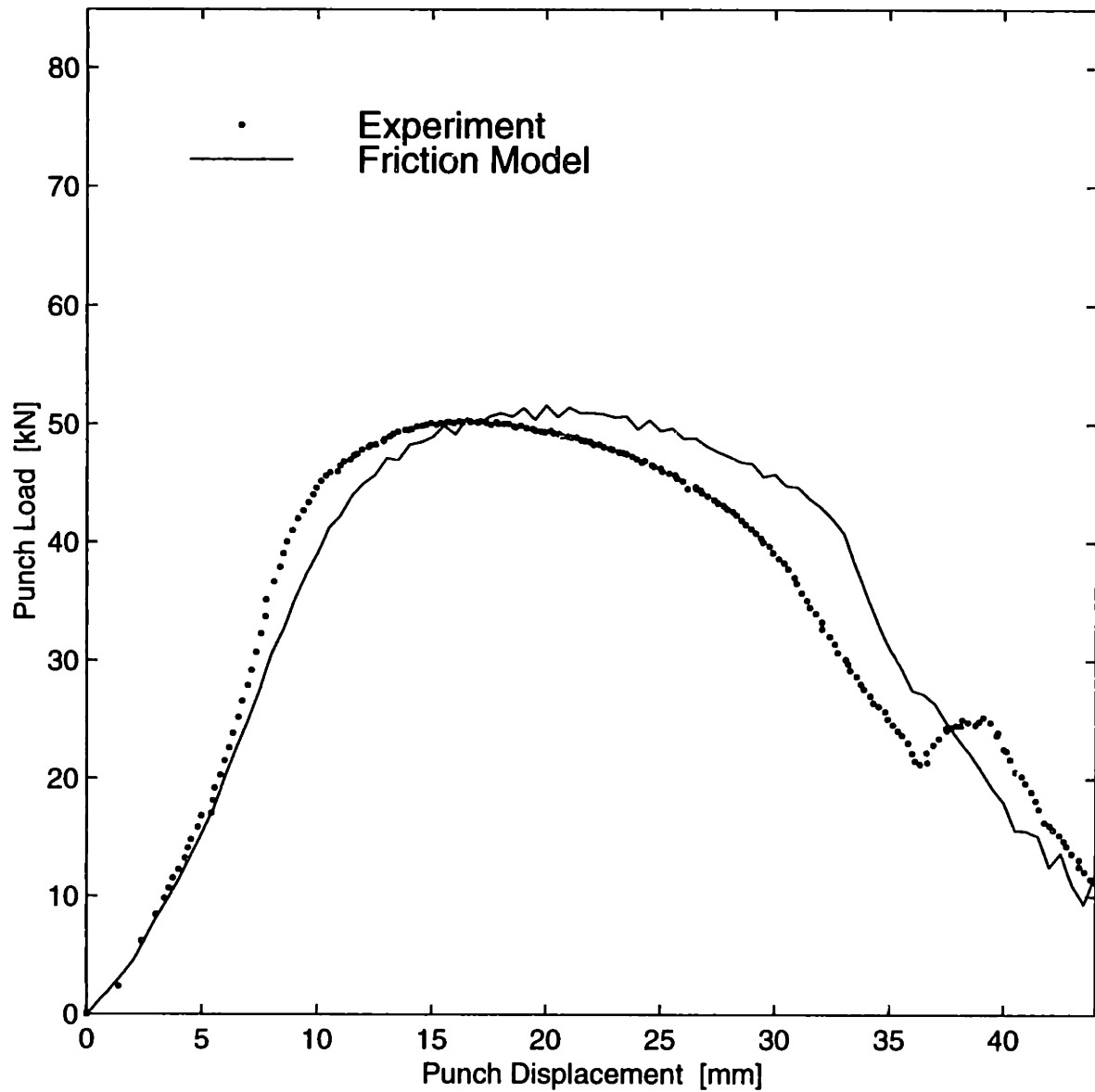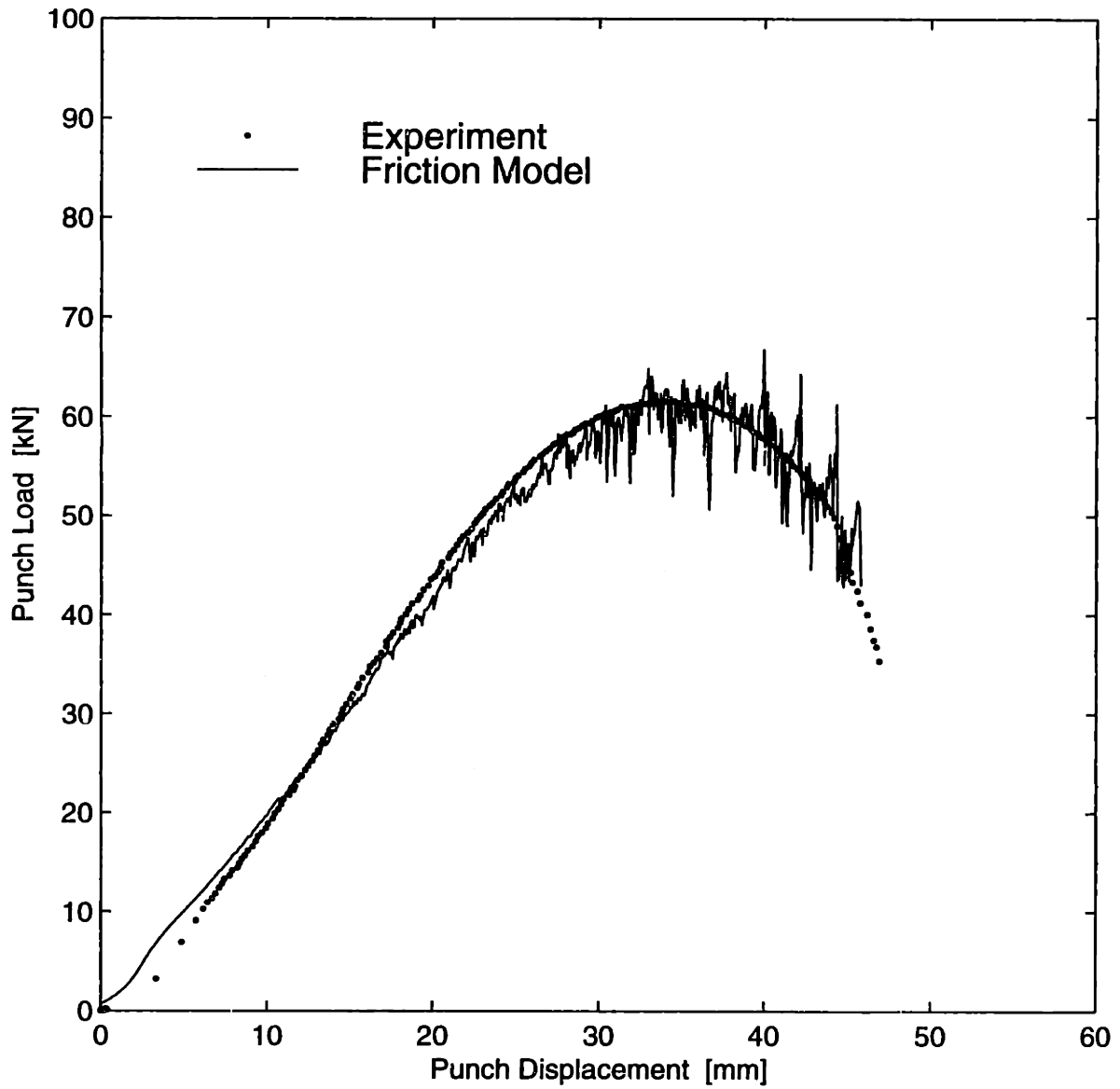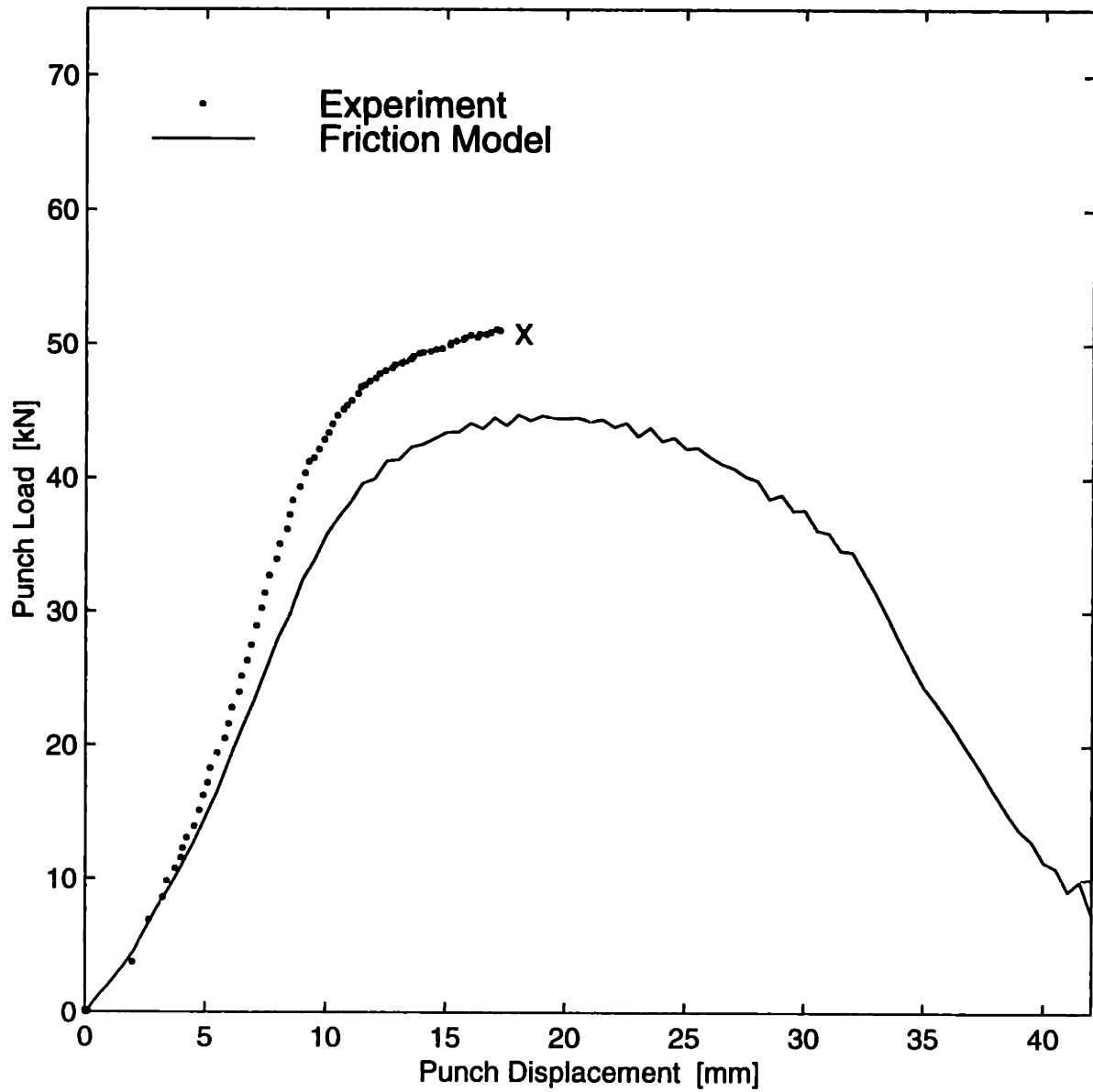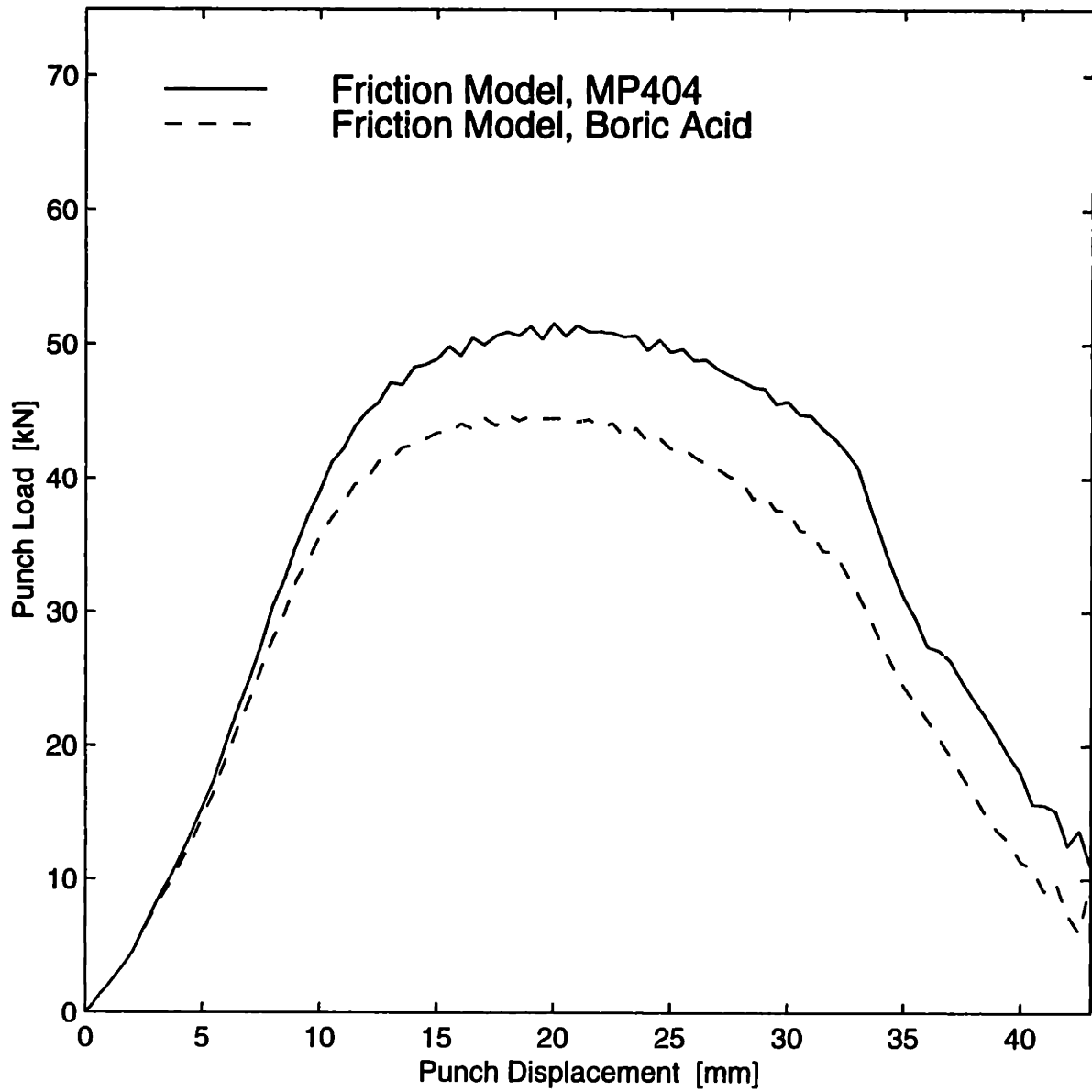
Figure D-36: Comparison of the numerical prediction against the measured punch load versus punch displacement for axisymmetric deep drawing of Al6111-T4 with MP404 lubricant.
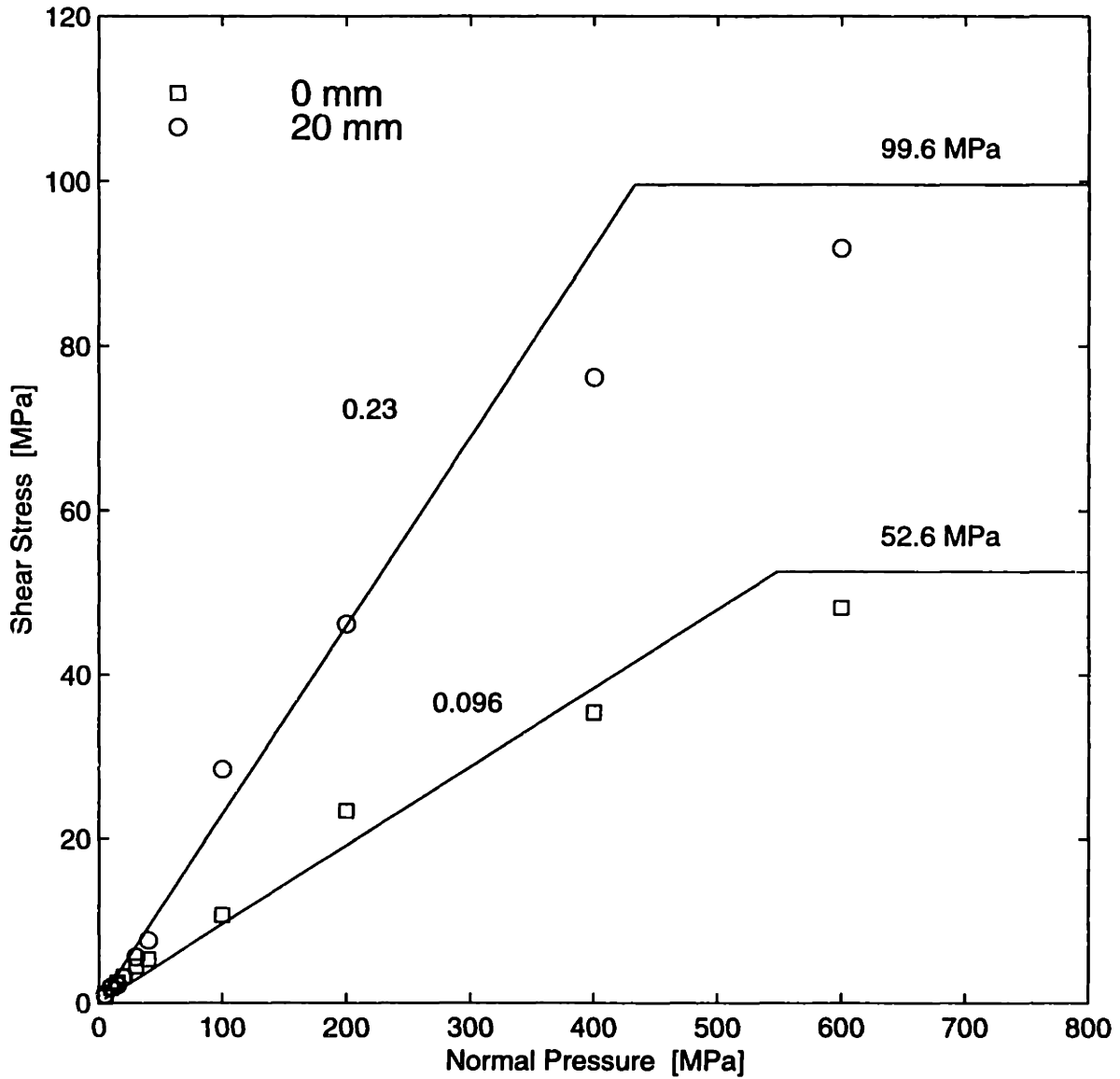
Figure D-37: Model parameters for the shear cap friction model with experimental data for the shear stress vs. normal pressure for the MP404 lubricated Al6111-T4 and tool steel interface at 0 mm and 20 mm of sliding.
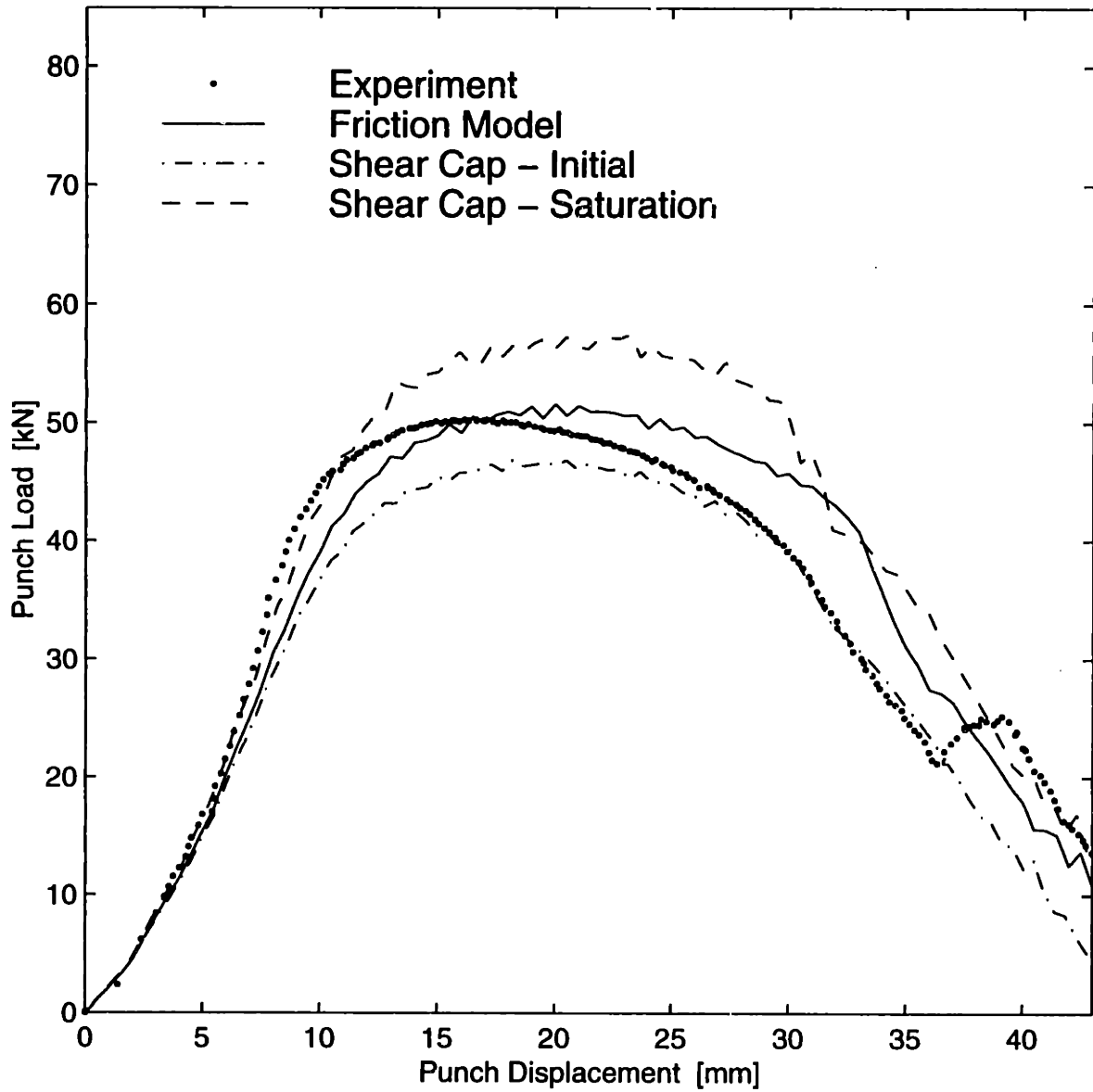
Figure D-38: Comparison of the numerical predictions of the new friction model and shear cap models against the measured punch load versus punch displacement for axisymmetric deep drawing of Al6111-T4 with MP404 lubricant.
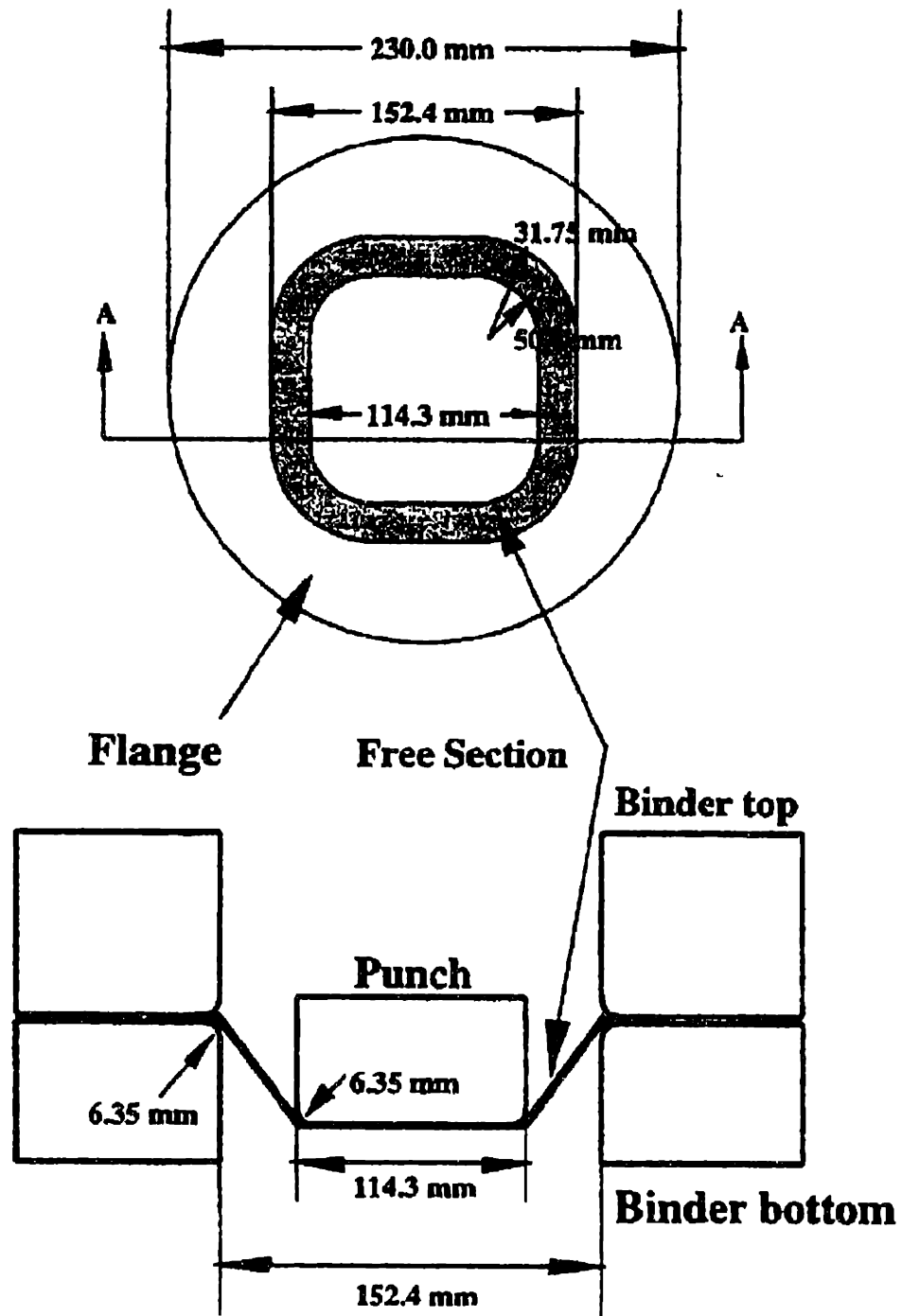
Figure D-39: Geometry of the square pan-drawing apparatus with dimensions in mm (adapted from [18]).

Figure D-40: Square pan of Al6111-T4 using MP404 lubricant (drawn to failure).
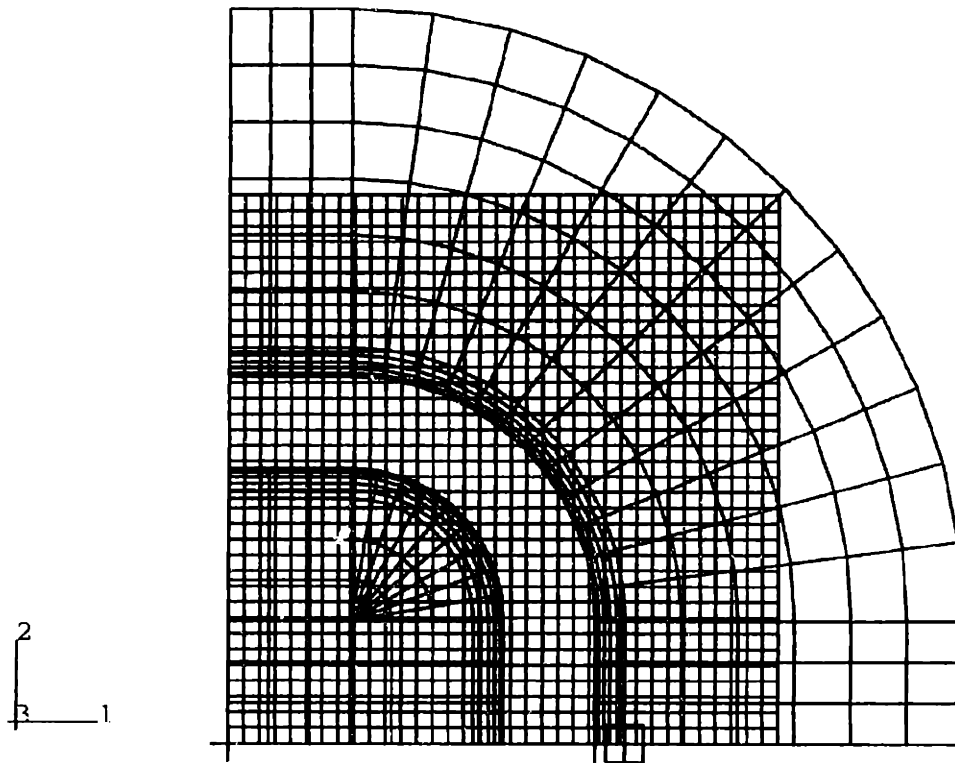
Figure D-41: Undeformed mesh for the simulation of the square pan-drawing of an Al6111-T4 blank with MP404 lubricant. The square is one quarter of the blank, the punch is in the lower left-hand corner, and the binder and die are in the upper right-hand corner.
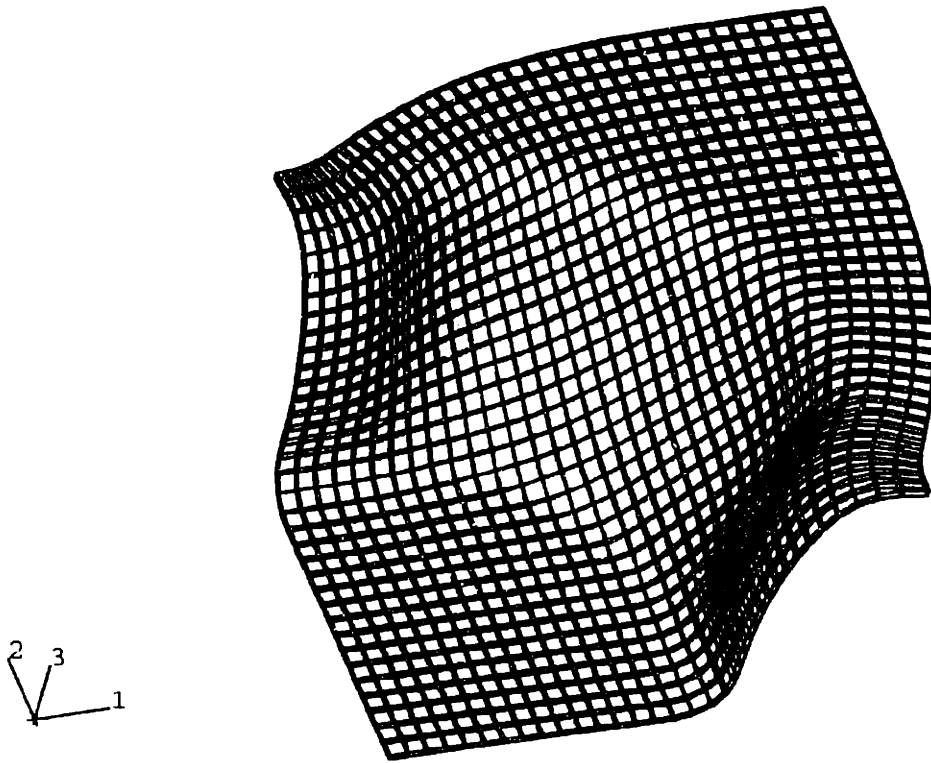
Figure D-42: Deformed mesh for the simulation of square pan-drawing of an Al6111-T4 blank with MP404 lubricant. Note that 1/4 of the pan is modeled.

Figure D-43: Comparison of the numerical prediction against the measured punch load versus punch displacement for square pan-drawing of Al6111-T4 with MP404 lubricant.

Figure D-44: Failed axisymmetric cup of Al6111-T4 using boric acid as lubricant.

Figure D-45: Comparison of the numerical prediction against the measured punch load versus punch displacement for axisymmetric deep drawing of Al6111-T4 with boric acid as lubricant. The failure load of the specimen is indicated by the X.

Figure D-46: Comparison of the numerical predictions of punch load versus punch displacement for axisymmetric deep drawing of Al6111-T4 with MP404 and boric acid as lubricants.
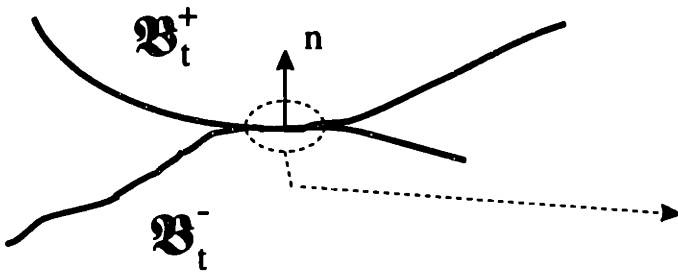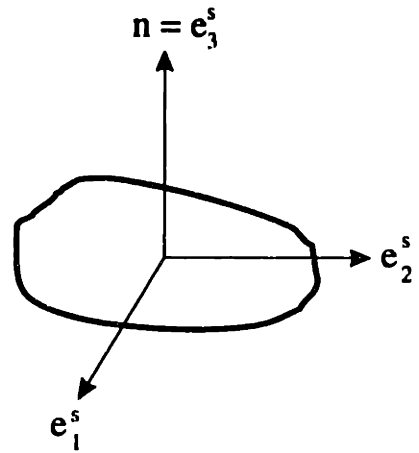
Figure D-47: Schematic of the macroscopic contact and local contact zone between the tool and workpiece.
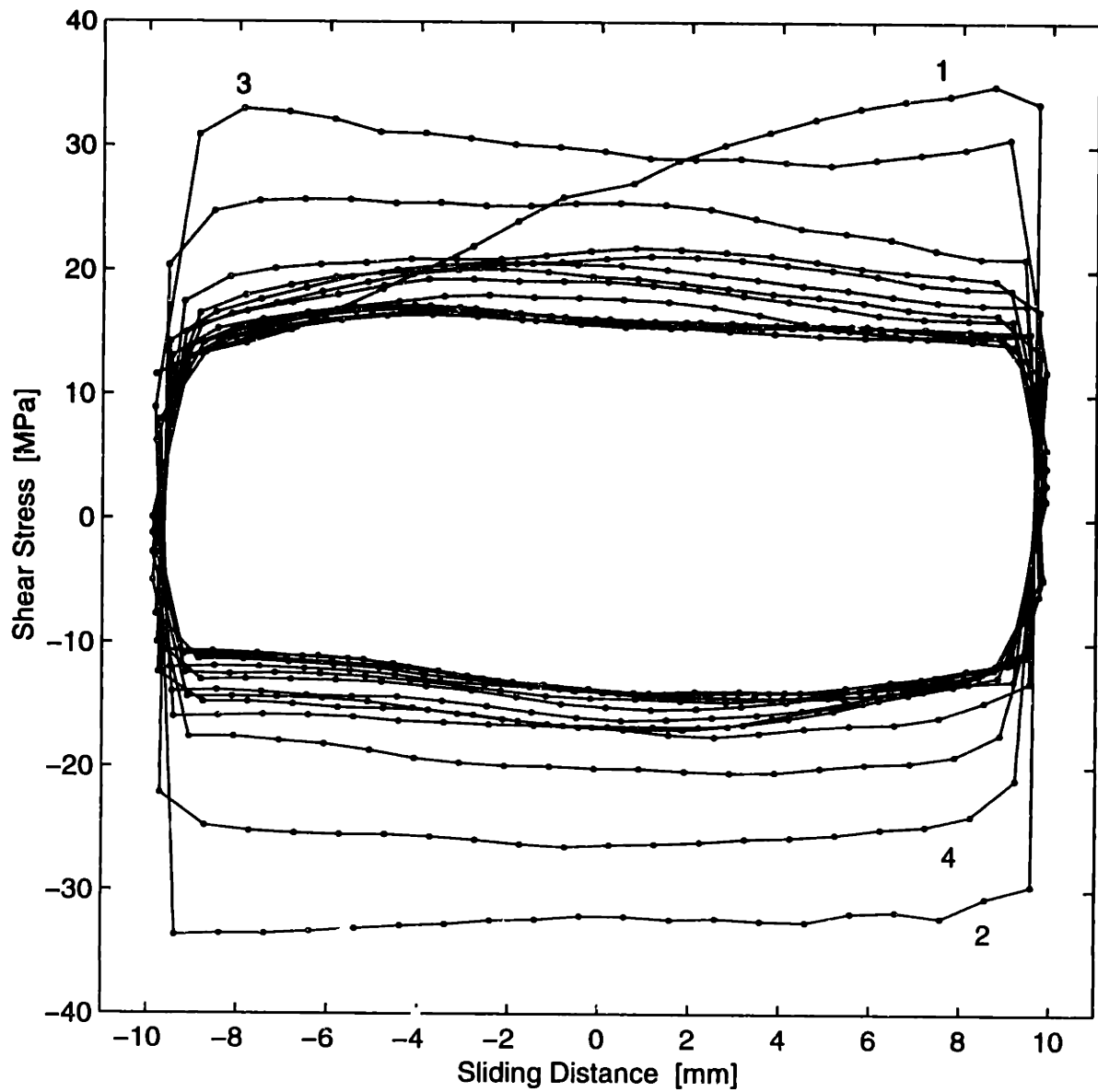
Figure D-48: Shear stress vs. sliding distance for the MP404 lubricated Al6111-T4 / tool steel interface under cyclic sliding at p = 100 MPa and $\bar{v}^s = 1$ mm/s.
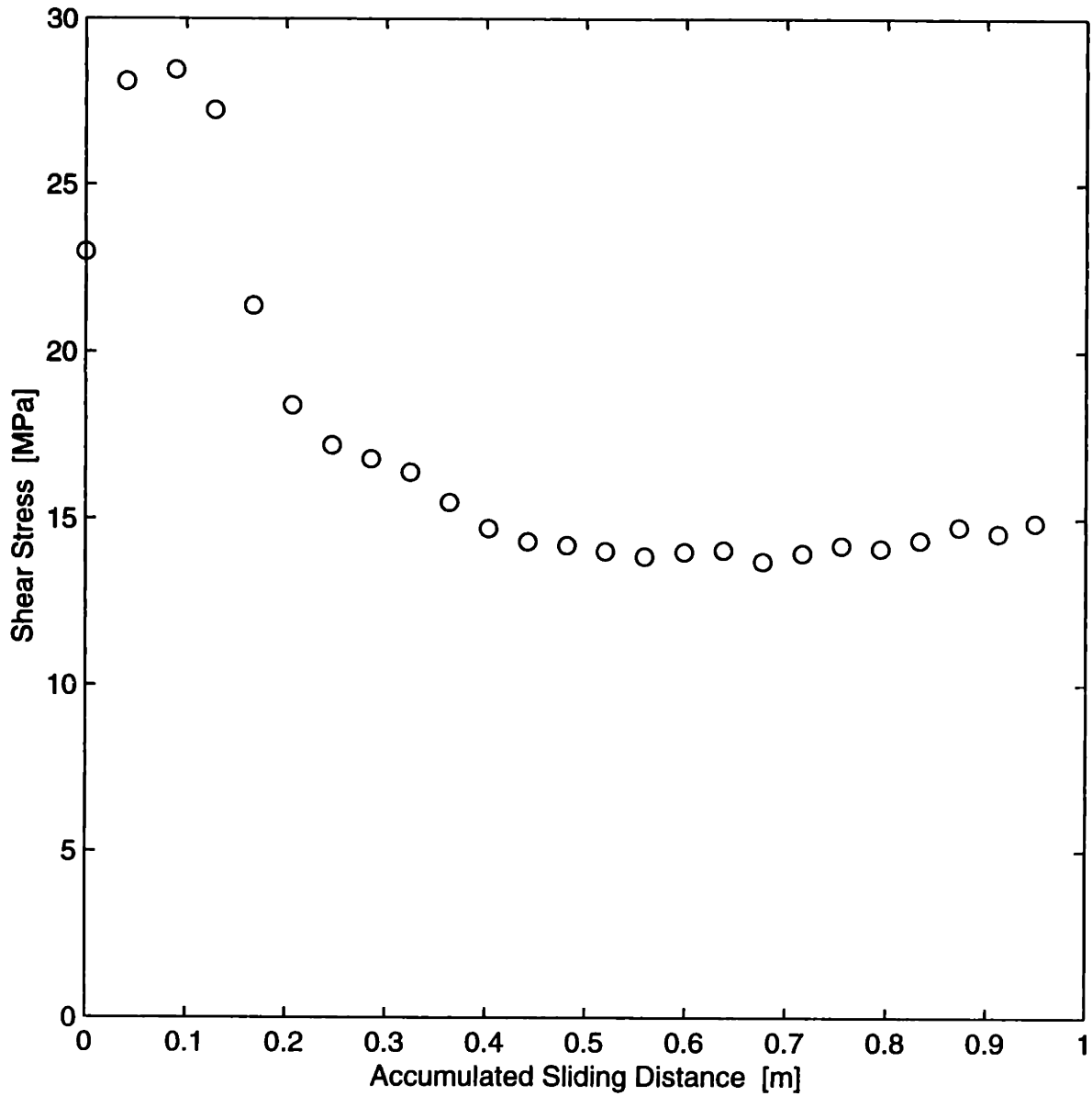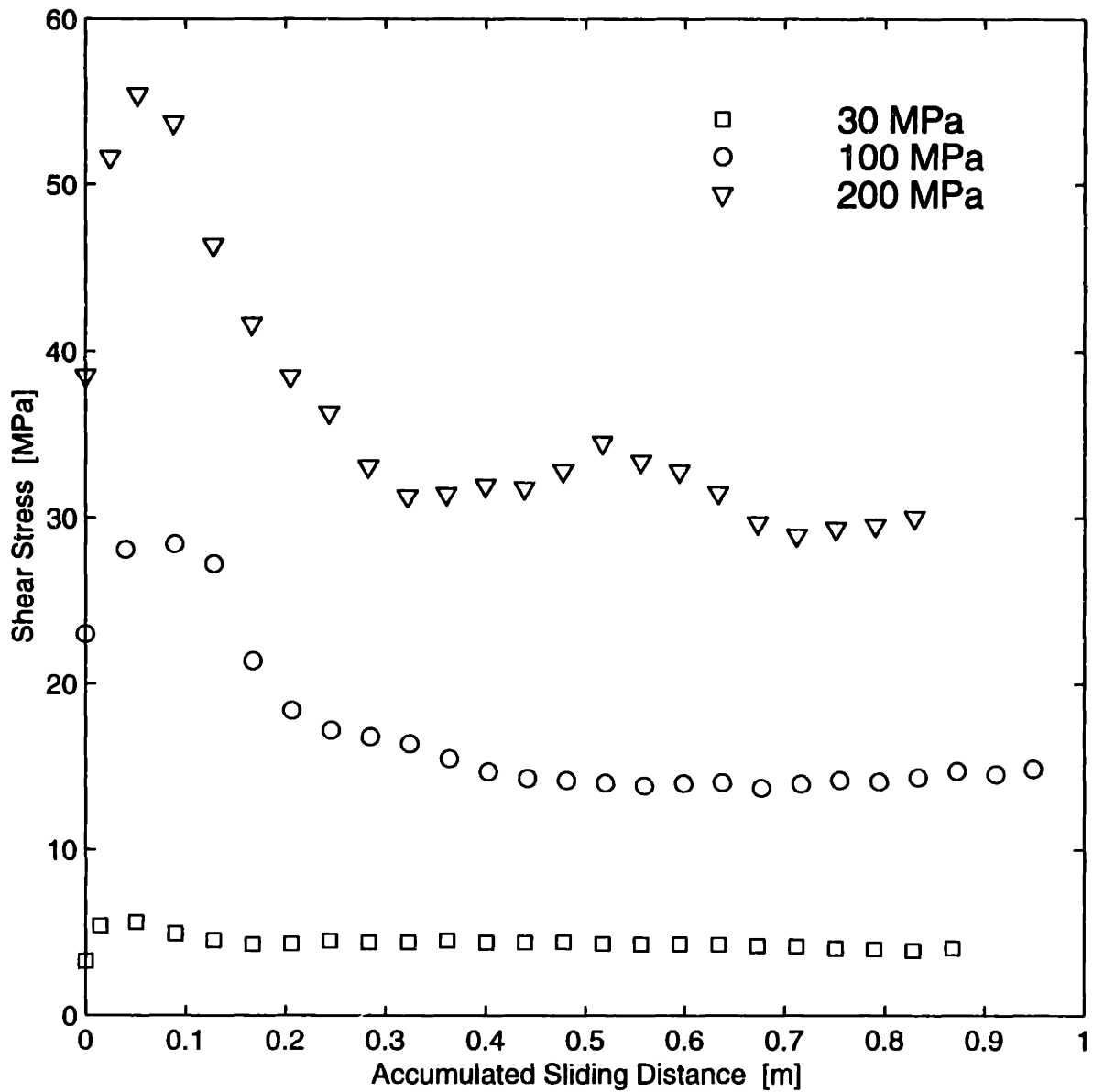
Figure D-49: Absolute value of shear stress vs. accumulated sliding distance for the MP404 lubricated Al6111-T4 / tool steel interface under cyclic sliding at p = 100 MPa and $\overline{v}^s$ = 1 mm/s.

Figure D-50: Absolute value of shear stress vs. accumulated sliding distance at various normal pressures for the MP404 lubricated Al6111-T4 / tool steel interface under cyclic sliding with $\bar{v}^s = 1$ mm/s.
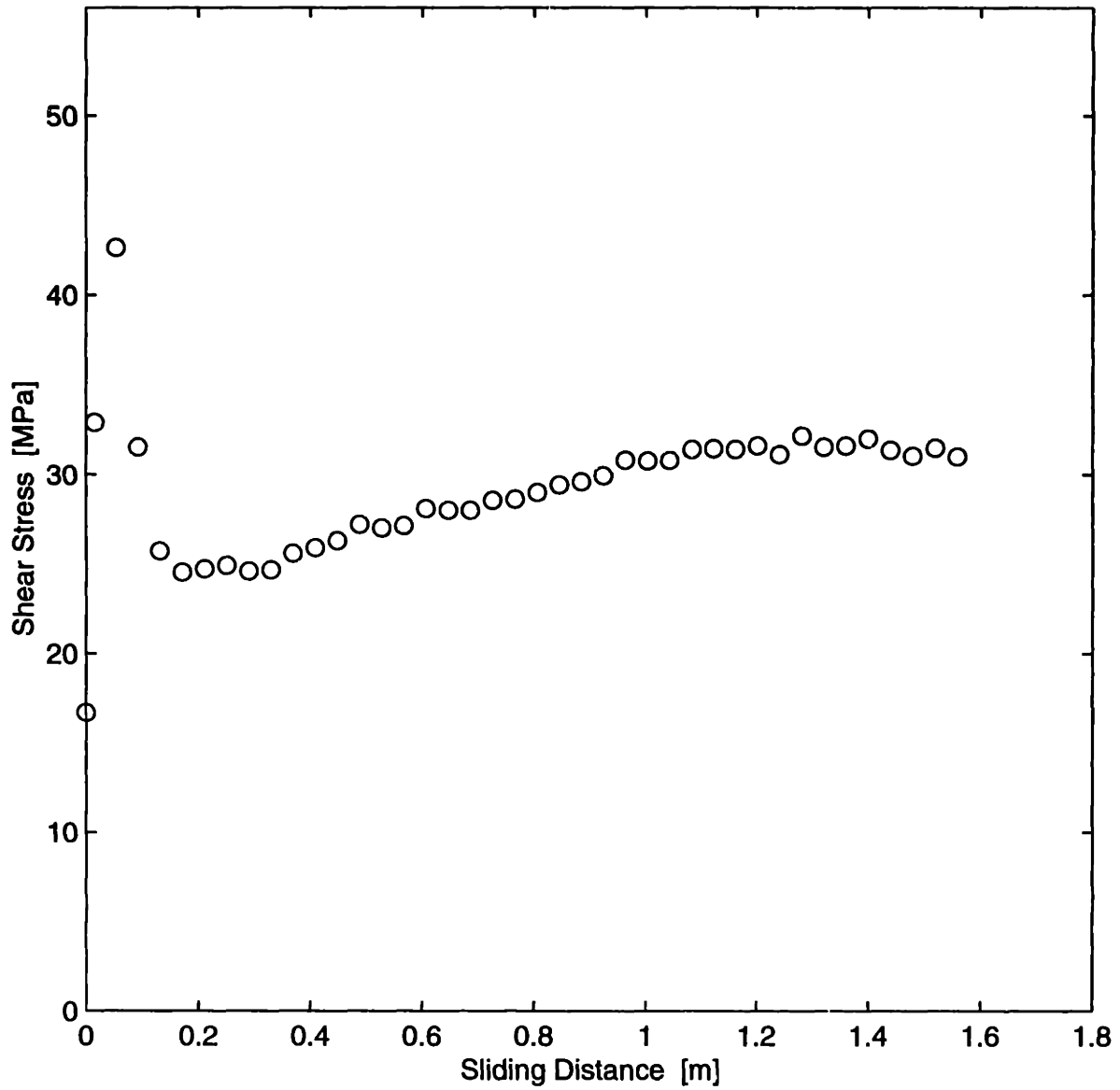
Figure D-51: Absolute value of shear stress vs. accumulated sliding distance for the MP404 lubricated Al6061-T6 / tool steel interface under cyclic sliding at p = 200 MPa and $\bar{v}^s = 1$ mm/s.
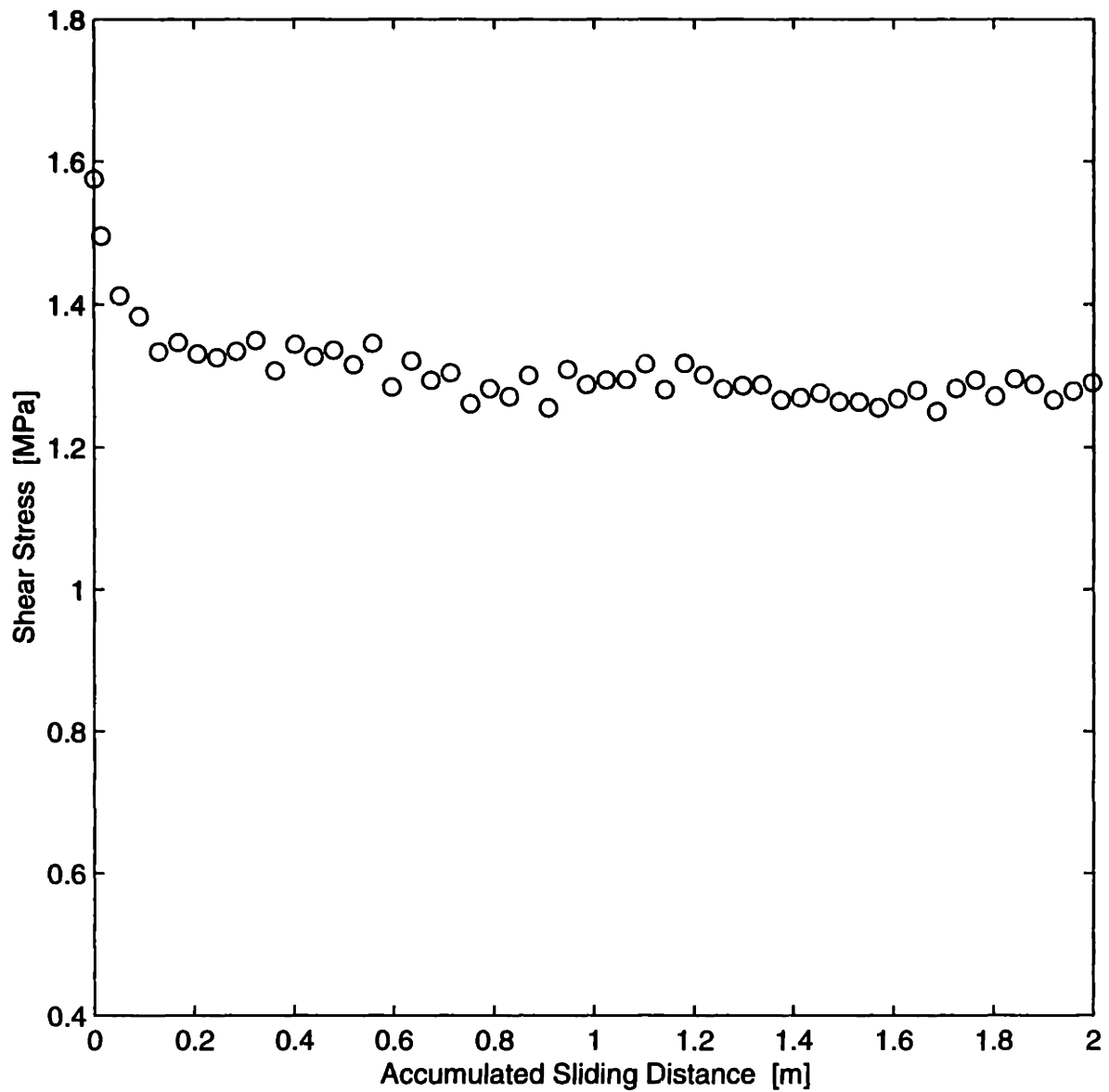
Figure D-52: Absolute value of shear stress vs. accumulated sliding distance for the boric acid lubricated Al6111-T4 / tool steel interface under cyclic sliding at p = 20 MPa and $\bar{v}^s = 1$ mm/s.
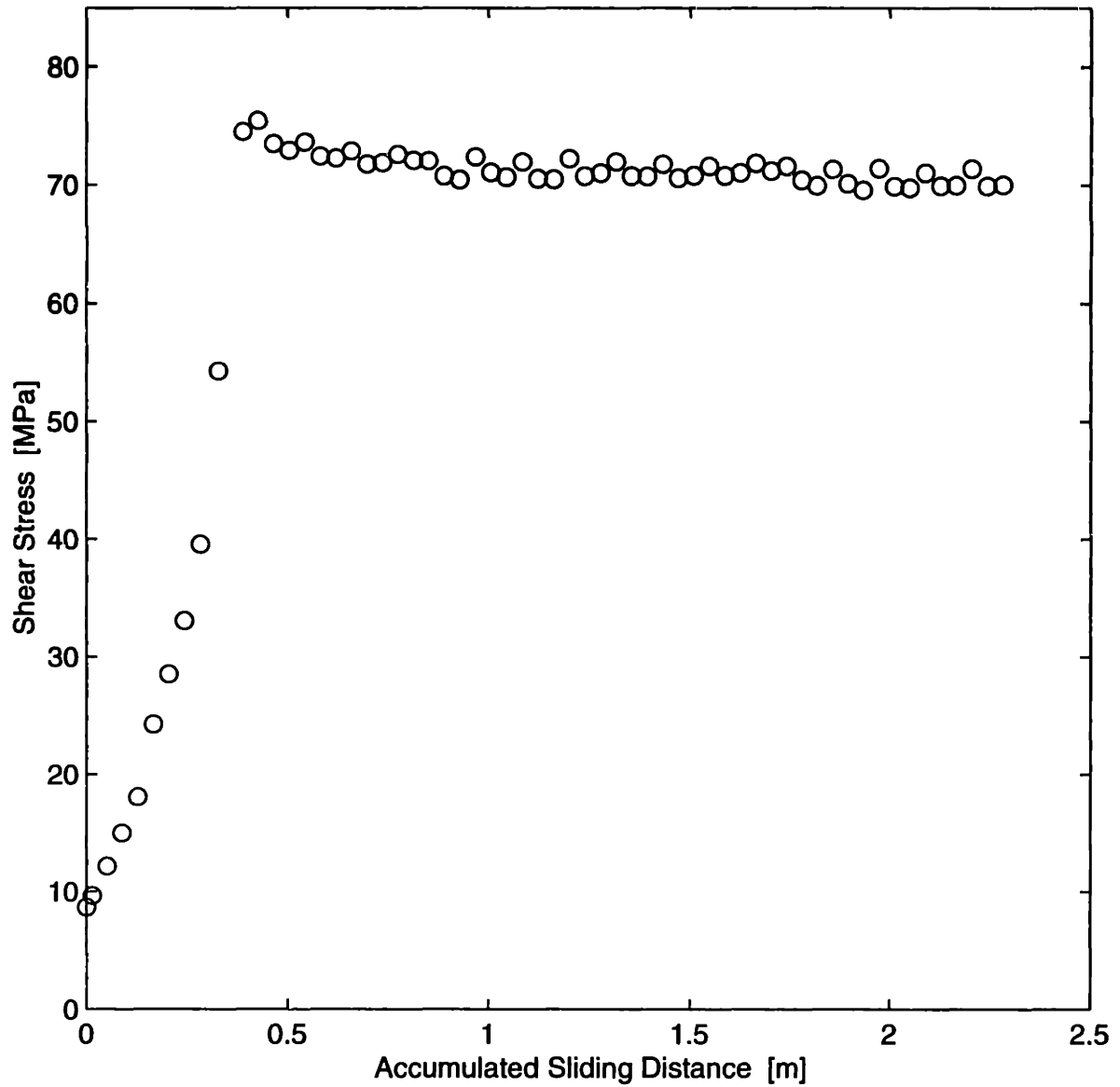
Figure D-53: Absolute value of shear stress vs. accumulated sliding distance for the boric acid lubricated Al6111-T4 / tool steel interface under cyclic sliding at p = 200 MPa and $\bar{v}^s = 1$ mm/s.